EMPIRICAL DETERMINATION OF PERFORMANCE CHARACTERISTICS FOR BUSEK 1CM MICRO RADIO-FREQUENCY ION PROPULSION SYSTEM

THESIS

Connor L. Muilenburg, Second Lieutenant, USAF

AFIT-ENY-MS-16-M-231

DEPARTMENT OF THE AIR FORCE
AIR UNIVERSITY

AIR FORCE INSTITUTE OF TECHNOLOGY

Wright-Patterson Air Force Base, Ohio

AFIT-ENY-MS-16-M-231

EMPIRICAL DETERMINATION OF PERFORMANCE CHARACTERISTICS FOR BUSEK 1CM MICRO RADIO-FREQUENCY ION PROPULSION SYSTEM

THESIS

Presented to the Faculty

Department of Aeronautics and Astronautics

Graduate School of Engineering and Management

Air Force Institute of Technology

Air University

Air Education and Training Command

In Partial Fulfillment of the Requirements for the

Degree of Master of Science in Astronautical Engineering

Connor L. Muilenburg, BS

Second Lieutenant, USAF

March 2016

AFIT-ENY-MS-16-M-231

EMPIRICAL DETERMINATION OF PERFORMANCE CHARACTERISTICS FOR BUSEK 1CM MICRO RADIO-FREQUENCY ION PROPULSION SYSTEM

Connor L. Muilenburg, BS

Second Lieutenant, USAF

Committee Membership:

Dr. C. R. Hartsfield, Ph.D.
Chair

Maj D. Liu, Ph.D.
Member

Dr. R. D. Branam, Ph.D.
Member

Abstract

Performance characterization for the Busek BIT-1 cm micro radio-frequency ion engine was accomplished across its full regime of operating conditions. The thrust was estimated at the nominal operating condition using a known relationship for ion engines between beam current, screen voltage, and the mass of the propellant used. Specific impulse was found at the nominal operating condition by its relation to the thrust and mass flow rate. The divergence angle of the plume of the ion engine was calculated using readings from a Faraday probe. The probe collected current density data at various angles in front of the ion engine, and with integration, the divergence angle was found. The thrust and specific impulse of the ion engine varied linearly with the total power input. This trait is very important for throttleability purposes, a useful capability for a thruster. The divergence angle of the 1 cm ion engine was calculated as 19.3 degrees, a parameter that is ideally minimized to reduce divergence losses. Preliminary testing of this micro ion engine indicates thrusters of this size may have potential in future CubeSat missions.

Acknowledgments

I would like to express my sincere appreciation to my faculty advisors, Major David Liu and Dr. Carl Hartsfield, for their guidance and support throughout the course of this thesis effort. Additionally, I would like to thank Dr. Mike Tsay and John Frongillo, along with their associates at Busek, Co. Inc. for their help with troubleshooting the numerous issues that arose in this research, along with the final setup and testing that occurred at Busek. I would like to thank Mr. Andrew Hine for his collaboration and setup advice while attempting thruster integration at the Air Force Institute of Technology. Finally, I would like to thank Mr. Jamie Smith, Mr. Josh Dewitt, and Mr. Keith Long for their laboratory assistance and expertise.

Connor L. Muilenburg

Table of Contents

Page

List of Figures

Page

List of Tables

Page

EMPIRICAL DETERMINATION OF PERFORMANCE CHARACTERISTICS FOR BUSEK 1CM MICRO RADIO-FREQUENCY ION PROPULSION SYSTEM

I. Introduction

1.1 Background

Electric propulsion affords the opportunity for many space missions formerly impossible within the realm of chemical thrusters. Ion engines, in particular, provide capabilities on the low thrust, high specific impulse end of the electric propulsion spectrum. Starting in 1964, when a pair of NASA Glenn ion engines became the first successful test of an ion engine in space, research on the subject has abounded [1, 2]. Experimental tests of the engines continued from the 1960s through the 1980s [3]. In terms of commercial use, the first ion engine on a commercial satellite in the United States was in 1997, when the Hughes Xenon Ion Propulsion System launched [4]. In the following year, Deep Space 1 launched; it became the first deep space interplanetary mission to successfully propel itself with an ion engine [5]. Electric propulsion systems, namely Hall and ion thrusters, have increased in popularity greatly in the last 10 years. This stems from extensive flight heritage, confirming electric propulsion is able to provide great mass savings and lifetime enhancements over the traditional chemical propulsion systems due to increased specific impulse.

Ion engines with flight heritage typically operate on the range of 2500 to 3600 seconds of specific impulse and consume power from 0.4 to 4.3 kW. Their efficiency is one of the highest of the electric propulsion devices, spanning from 40 to 80 percent [3]. These features, combined with micro-Newton thrust levels, make ion engines ideal for non-impulsive maneuvers such as station keeping and orbital insertion. Ion engines are

also used in the context of deep space, as those missions require high specific impulse to maintain a plausible vehicle mass and reach the desired location within a reasonable time period. Though the low thrust of electric propulsion systems, specifically ion engines, limits some applications, their relatively recent resurgence and continued proliferation is indicative of huge future potential.

1.2 Motivation

The performance of Hall thrusters and ion engines is correlated with the size of the system. For a given input power level, the thrust and specific impulse are inversely related. Therefore, if a mission requires relatively high thrust and specific impulse, the only way to achieve such results with the given technology is to increase the powerplant mass. On the other end of the spectrum, Hall thrusters and ion engines can only get so small before they are inoperable due physical phenomena. For Hall thrusters, the Larmor radius places a limitation on design. The thruster channels are at least as big as the Larmor radius, which is depending upon the magnetic field, and therefore magnet current, preventing the thruster from decreasing in size beyond a certain point. For ion engines, the size constraint of the power processing unit along with the space charge effect—particles of like charge repelling—limit the sizing options [3]. At a certain point, the engine becomes too inefficient for plausible operation. The thruster studied in this research is on the small end of the spectrum, with a diameter of only one centimeter. Though it is theoretically possible to make a smaller thruster, research completed by Busek Co., Inc. indicates scaling smaller will exponentially increase the coil resistance, and will thereby increase the ohmic heating loss [6].

Micro-thrusters are necessary for precise actuation on various CubeSat missions. Busek Co., Inc. was selected by NASA/JPL to develop the 1cm-class micro RF ion thruster system researched for this thesis. Specifically, this thruster was designed for use on the Laser Interferometer Space Antenna (LISA) mission, which requires precise pointing accuracy to maintain a constellation with the mission of studying cosmic gravitational waves [6]. Figure 1, from the same source, details various missions that require high precision control and/or metrology, thereby necessitating micro-thruster actuation.

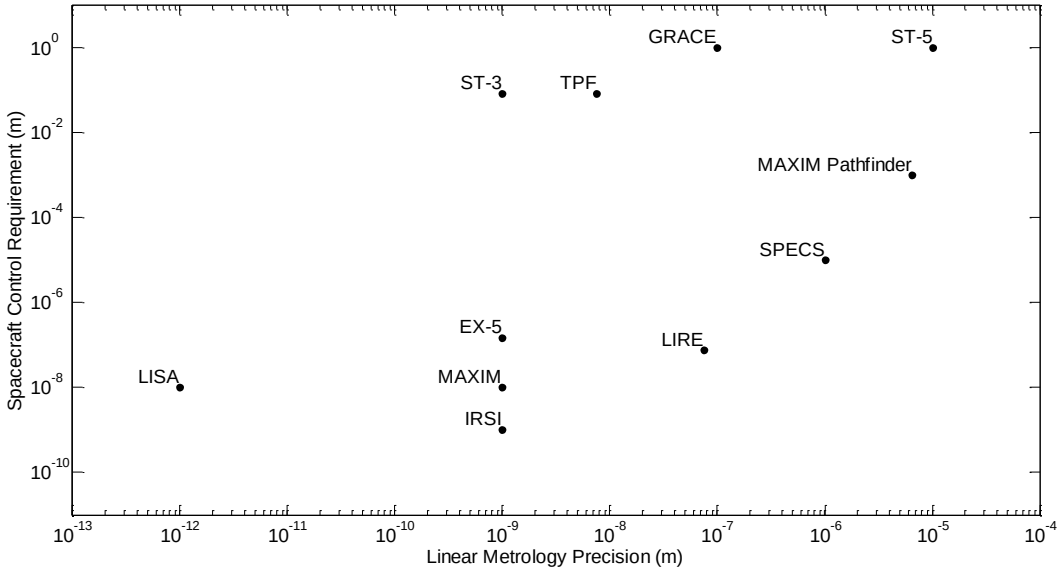

Figure 1. Spacecraft position and metrology requirements for various missions [6].

Radio-frequency (RF) ion thrusters in particular are a desirable design due to their simplicity. They require neither an internal cathode nor permanent magnetic structures for plasma generation. Instead, they use a helical coil powered at a low mega-hertz frequency to produce the plasma necessary for thruster operation; the plasma is then

confined by the electromagnetic field produced by the energized helical coil [6]. Since internal cathodes and magnetic structures are unnecessary in this type of thruster, it is easier to scale down. Micro RF ion thrusters have potential within the DOD mission set due to their precise, low thrust capabilities, high specific impulse, and long lifetimes, allowing for a great range of applications.

1.3 Scope

Though Busek Co. Inc. has completed some preliminary testing on the Busek 1cm Micro RF ion engine, further analysis and verification of performance is desired. The thrust measurements by Busek were accomplished using estimations which are generally 95% accurate according to their previous experience with gridded ion thrusters [6]. Research completed in this thesis will attempt to determine the thrust using a torsional thrust stand, which is capable of fine precision. The torsional thrust stand will theoretically allow for more accurate measurements than the current data. From the thrust information and mass flow rate, the specific impulse is determined. In order to further characterize the thruster's performance, a Faraday probe is used to analyze the divergence angle of the plume. This measurement will ideally occur at several axial distances from the thruster face and sweep across the plume to detect the current density of the ions striking the collector plate. All tests will occur at a nominal and a maximum setting. The variables changed in testing are the propellant mass flow rate to the thruster, the radio-frequency power setting, and the screen voltage.

1.4 Objectives

The United States Air Force relies on space dominance to maintain its global position of power. An important aspect of this dominance is the ability of microsatellites to fly in formation in the future. In order to do so, small and accurate attitude control and orbital maintenance inputs are necessary to maintain spacing between satellites. Ion thrusters are an efficient method of propulsion and are scalable in order to meet the needs of this objective. At small scales, though, ion thruster can exhibit diminished performance; therefore, performance analysis is necessary to quantify the abilities of ion thrusters on the small end of the spectrum to determine their potential for use with CubeSats. The goal of this research is to quantify the performance of the Busek BIT-11cm Micro Radio-Frequency Ion Propulsion System in support of the Air Force CubeSat mission. The following objectives are necessary to accomplish the research goal:

1. Measure the thrust at the nominal operating condition.
2. Determine the specific impulse at the nominal operating condition.
3. Quantify the thrust envelope for varying thruster propellant mass flow rate, radio-frequency power, and screen voltage.
4. Determine the specific impulse throughout the flight envelope.
5. Determine the divergence angle of the plume.

II. Literature Review

2.1 Chapter Overview

The purpose of this chapter is to describe the history of the ion engine, discuss how ion engines work, investigate the electrostatic theory involved in their operation, and delve into the development of radio-frequency ion engines. Additionally, the concept of the neutralizer cathode, which is vital to the operation of an ion engine, is explained. Finally, and most importantly, this chapter will explore the effects of sizing on the performance of the ion engine, as it is one of the main focuses of this research.

2.2 History of the Ion Engine

In the 1950s, research at NASA Glenn by an engineer named Dr. Harold Kaufman began the development of ion propulsion. By 1959, he built the first ion engine. As previously mentioned, the year 1964 brought the first successful space test of an ion engine, SERT 1, which had a pair of thrusters created at NASA Glenn. During testing, one engine did not function; however, the other operated for a total of 31 minutes. With the follow-up test, SERT 2, NASA Glenn was able to deliver a thruster able to operate for nearly three months and another capable of running successfully for more than five [1]. These early systems used either mercury or cesium as propellants. In current times, ion engines have migrated nearly exclusively to xenon. At standard temperature and pressure, mercury and cesium are non-gaseous, meaning some source of heat is necessary on orbit to convert the propellant in the desired state. Additionally, testing indicated both of these propellants had the chance of cooling after exiting the nozzle, condensing on the spacecraft, which is potentially life limiting [1].

Xenon is desirable as a propellant for numerous reasons. Primarily, it is not hazardous to handle, making the processing and use of the propellant very convenient. The relatively high atomic mass of xenon compared to the other noble gases means it will produce more thrust for a given input power. Xenon is storable at high pressures, meaning less spacecraft volume is necessary for fuel. Finally, if spacecraft components are at temperatures greater than cryogenic, xenon does not condense [3]. The first operational xenon-propelled ion engine was launched in 1979, over a decade after the original SERT 1 tests. From this point on, research mainly shifted towards the usage of xenon, making it the standard of ion thrusters today.

2.3 Electrostatic Theory

In order to understand how ion engines operate, one must first delve into basic electrostatic theory and plasma physics. These fields give some insight into the interactions occurring within electric propulsion systems. First, the concept of plasma is discussed. A plasma is formed in a thruster when the propellant gas is ionized, creating ions and electrons. Together, the positive ions and electrons satisfy quasi-neutrality; as a whole, the plasma is essentially neutrally charged. The analysis of ion engines is based on making general assumptions about plasma behavior in the region of interest. Near the boundaries of a thruster, quasi-neutrality is not satisfied. Additionally, it is not satisfied when the spatial scale length of the plasma is much larger than the Debye length. The Debye length is the characteristic length over which charges are electrostatically shielded [3], and it is discussed later.

Plasmas in an electric propulsion system have associated electric and magnetic fields that obey Maxwell's equations. The equations are

$$\nabla \cdot \mathbf{E} = \frac{\rho}{\epsilon_o} \quad (1)$$

$$\nabla \times \mathbf{E} = -\frac{\partial \mathbf{B}}{\partial t} \quad (2)$$

$$\nabla \cdot \mathbf{B} = 0 \quad (3)$$

$$\nabla \times \mathbf{B} = \mu_o \left(\mathbf{J} + \epsilon_o \frac{\partial \mathbf{E}}{\partial t} \right) \quad (4)$$

where E is the electric field vector, ρ is the charge density in the plasma, ϵ_o is the permittivity of free space, B is the magnetic field vector, μ_o is the permeability of free space, and J is the current density in the plasma [3]. The charge density is

$$\rho = \sum_{\mathbf{s}} q_s n_s = e(Zn_i - n_e) \quad (5)$$

where q_s is the charge state of species s, Z is the charge state, n_i is the ion number density, and n_e is the electron number density [3]. The current density is

$$\mathrm{J} = \sum_{\mathbf{s}} q_s n_s v_s = e(Zn_i v_i - n_e v_e) \quad (6)$$

where v_s is the velocity of the charge species, v_i is the ion velocity, and v_e is the electron velocity [3]. For static magnetic fields, where the partial derivative of the magnetic field with respect to time is zero, the electric field is the gradient of the electric potential.

$$\mathbf{E} = -\nabla\phi \tag{7}$$

The above equations describe the behavior of electric and magnetic fields in a plasma and are vital to the understanding of ion engine performance. The force on a charged particle with velocity v in a magnetic field is given by the Lorentz force equation [3].

$$\mathbf{F} = \mathrm{m}\frac{d\mathbf{v}}{d\mathrm{t}} = q(\mathbf{E} + \mathbf{v} \times \mathbf{B}) \tag{8}$$

As ion engines use only an electric field, rather than an electric and magnetic field like Hall thrusters, Equation 8 can be simplified with a zero vector magnetic field.

$$\mathbf{F} = q\mathbf{E} \tag{9}$$

Additionally, one needs to know the electric field caused by the interaction of a charge density with a specific point, which is given by Coulomb's law.

$$\mathbf{E}(\mathbf{r}) = \frac{1}{4\pi\epsilon_\mathrm{o}} \int d\boldsymbol{r}'\rho(\boldsymbol{r}')\frac{(\boldsymbol{r} - \boldsymbol{r}')}{|\boldsymbol{r} - \boldsymbol{r}'|^3} \tag{10}$$

Though it is possible to use Equation 9 to find the force on any given particle, it is implausible to track every particle in an ion engine, as they have frequent collisions. Therefore, it is useful to describe the particle velocities as a distribution. On average, and barring any outside forces, particles move with a speed dependent on only the macroscopic temperature and species mass. Because of this, the charged particles in an ion engine are described with various velocity distribution functions, and the random motions calculated by the moments of the distributions [3].

Most of the charged particles in an ion engine follow a Maxwellian velocity distribution, the most probable velocity distribution for particles in thermal equilibrium [3]. One dimensionally, the Maxwellian velocity distribution is

$$f(v) = \left(\frac{m}{2\pi kT}\right)^{\frac{1}{2}} \exp\left(-\frac{mv^2}{2kT}\right) \quad (11)$$

where m is the particle mass, k is Boltzmann's constant, and the width of the distribution is determined by T, the temperature [3]. The average kinetic energy of a particle in the Maxwellian velocity distribution can be represented by Equation 12.

$$E_{ave} = \frac{\int_{-\infty}^{\infty} \frac{1}{2} mv^2 f(v) dv}{\int_{-\infty}^{\infty} f(v) dv} \quad (12)$$

By combining Equations 11 and 12 and integrating, the average energy per particle can be determined [3].

$$E_{ave} = \frac{1}{2} kT \quad (13)$$

Equation 10 can be written three dimensionally to incorporate velocity terms in all three axes. If Equation 10 is combined with Equation 12 and integrated, as before, the average energy in three dimensions is found [3].

$$E_{ave} = \frac{3}{2} kT \quad (14)$$

The average speed of a particle in the Maxwellian velocity distribution is

$$\bar{v} = \int_0^{\infty} v \left(\frac{m}{2\pi kT}\right)^{\frac{3}{2}} \exp\left(-\frac{v^2}{v_{th}^2}\right) 4\pi v^2 dv \quad (15)$$

where v is the particle speed and v_{th} is defined in Equation 16 [3].

$$v_{th} = \left(\frac{2kT}{m}\right)^{\frac{1}{2}}. \quad (16)$$

If the equation for the average speed of a particle in the Maxwellian velocity distribution is integrated in the same fashion as before, the average speed of a particle is found.

$$\bar{v} = \left(\frac{8kT}{\pi m}\right)^{\frac{1}{2}} \quad (17)$$

The flux of particles in one dimension for a Maxwellian distribution are described below.

$$\Gamma_Z = \int n v_Z f(\mathbf{v}) d^3\mathbf{v} \quad (18)$$

Assuming the incident velocity has a cosine distribution ($v_Z = v\cos\theta$), the one-sided random electron flux is shown in Equation 19.

$$\Gamma_Z = \frac{1}{4} n\bar{v} = \frac{1}{4} n \left(\frac{8kT}{\pi m}\right)^{\frac{1}{2}} \quad (19)$$

Electrons in the plasma make many inter-particle collisions, so they can be described by a Maxwellian temperature T_e and are described by the above equations [3]. Because the electrons are on the order of 10 times the temperature of the ions, the previously listed equations apply only to electron motion. On the other hand, the ion motion and velocity is determined by the plasma electric field interactions, so a different set of governing

equations are necessary. The equation to describe diffusion-driven particle motion in ion thrusters is

$$mn\frac{d\mathbf{v}}{dt} = qn(\mathbf{E} + \mathbf{v} \times \mathbf{B}) - \nabla \cdot \mathbf{p} - mnv(\mathbf{v} - \mathbf{v_o}) \quad (20)$$

where v is the collision frequency between the two species [3]. If the magnetic field term is neglected, Equation 20 simplifies to the following:

$$mn\frac{d\mathbf{v}}{dt} = qn\mathbf{E} - \nabla \cdot \mathbf{p} - mnv(\mathbf{v} - \mathbf{v_o}) \quad (21)$$

Solving for the velocity of the particle yields Equation 22,

$$\mathbf{v} = \frac{q}{mv}\mathbf{E} - \left(\frac{kt}{mv}\right)\left(\frac{\nabla \mathrm{n}}{\mathrm{n}}\right) \quad (22)$$

where the coefficient of the electric field term is called the mobility and the coefficient of the diffusion gradient term is known as the diffusion coefficient [3].

The final subject discussed in this section is the concept of sheaths, which form at boundaries of the plasma. In response to applied fields or a particle imbalance, either describing a boundary condition, a plasma may not be quasi-neutral at the boundaries. The region of potential and density change is known as the sheath, and it is a natural consequence of the differing mobilities of ions and electrons in ion engines [3]. For example, if a negatively biased electrode is placed next to a plasma, the edge of the plasma is densely populated with positive ions due to their attraction to the negative charge. The next layer into the plasma will have a relatively dense electron grouping due to their attraction to the high number of ions.

Through a long series of manipulations, starting from Gauss's law, one can obtain the following equation

$$\phi = \frac{e}{4\pi\epsilon_o r}\exp\left(-\frac{r}{\lambda_D}\right) \quad (23)$$

where ϕ is the electric flux, r is the radius of an arbitrary sphere around a given test charge, and $\lambda_D = \sqrt{\frac{\epsilon_o kT_e}{n_o e^2}}$. λ_D is the Debye length, which is defined as the characteristic distance over which the potential changes [3]. Equation 23 indicates there is a charge shielding occurring in the plasma. Therefore, the potential at a sphere of radius r from the charged particle decays by 1/r as well as exponentially due to the fact the test charge is not neutral [3].It is a common assumption within electric propulsion to assume the sheath around an object is the thickness of a few Debye lengths in order for the potential to fall to a negligible value [3].

One of the most important uses of sheath physics in an ion thruster is the Child-Langmuir law. Derived independently in the early 1900s by both Child and Langmuir, their law states

$$J_i = \frac{4\epsilon_o}{9}\left(\frac{2e}{M}\right)^{\frac{1}{2}}\left(\frac{V^{\frac{3}{2}}}{d^2}\right) \quad (24)$$

where J_i is the current per unit area, e is the elementary charge, M is the mass of the particle, V is the voltage, and d is the thickness of the sheath [3]. The Child-Langmuir law states the current per unit area capable of passing through a sheath is related to the voltage and the thickness of the sheath. In ion engines, this equation has a very important

purpose. The accelerator structure is designed using the Child-Langmuir equation to find the required voltage across a gap between accelerator electrodes or vice versa.

Though the above equations do not provide a complete understanding of plasma physics, they give a basic understanding. With this brief overview, one has enough information to further delve into the workings of ion engines, discussed in the following section.

2.4 Operation of Ion Engines

Before it is possible to discuss the operation of ion engines, fundamental thruster principle knowledge is necessary. Electric thrusters, in the basic sense, work the same way as chemical thruster. Mass is accelerated out of the system to create thrust in the opposite direction. For electric propulsion, the primary form of thrust creation occurs through the acceleration of charged particles, unlike chemical systems, where combustion reactions provide the energy for propellant to escape through a nozzle. The ideal rocket equations for chemical and electric systems is the same

$$\Delta V = -(\mathrm{I_{sp}} * \mathrm{g_0}) \ln\left(\frac{m_d}{m_d + m_p}\right) \quad (25)$$

where ΔV is the change in velocity of the spacecraft, Isp is the specific impulse of the system, $\mathrm{g_0}$ is the gravitational acceleration, $\mathrm{m_d}$ is the deadweight mass of the spacecraft, and $\mathrm{m_p}$ is the propellant mass [3].

The thrust produced by an ion engine is the sum of the forces on the screen grid and the acceleration grid,

$$F_{screen} = \frac{1}{2}\epsilon_o E_{screen}^2 \quad (26)$$

$$F_{accel} = -\frac{1}{2}\epsilon_o E_{accel}^2 \quad (27)$$

$$T = F_{screen} + F_{accel} = \frac{1}{2}\epsilon_o (E_{screen}^2 - E_{accel}^2) \quad (28)$$

where all terms are in SI units. Knowing the net force on the grids, or the thrust, is equal and opposite to the electric field forces on the ions between the two grids, Equation 29 is obtained.

$$T = -F_{ion} = -\frac{1}{2}\epsilon_o (E_{accel}^2 - E_{screen}^2) \quad (29)$$

Equations 28 and 29 shows the thrust in an ion engine is transferred by the electrostatic force between the ions and two grids [3]. As stated by Newton's Second Law, the force is the time rate of change of momentum. In this case, the exit velocity does not change, so there is only one term left in the equation after the derivative is calculated.

$$T = \frac{d}{dt}(m_p v_{ex}) = \dot{m}_p v_{ex} \quad (30)$$

where $\dot{m}_p$ is the propellant mass flow rate, equal to the propellant particle flow rate Q times the particle mass M [3]. Using Equations 29 and 30, it is clear that the thrust produced is related to both the electric field of the screen and accelerator grids and the mass flow rate times the exit velocity, providing two separate ways to calculate the thrust. The jet power, or the kinetic thrust power of the beam, is defined below.

$$P_{jet} = \frac{1}{2}\dot{m}_p v_{ex}^2 = \frac{T^2}{2\dot{m}_p} \quad (31)$$

In ion engine, ions are accelerated to high velocities using an electric field. Unionized particles also escape from the system, but their comparatively low velocity means their impact to thrust is negligible. Therefore, the thrust of an ion engine is approximately equal to the mass flow rate of the ions times their exit velocity [3]. The ion exit velocity is

$$v_i = \sqrt{\frac{2qV_b}{M}} \quad (32)$$

where q is the charge, V_b is the voltage through which the ion was accelerated, and M is the ion mass [3].

By defining the relationship between ion mass flow rate with beam voltage, mass, and charge, one arrives at the final equation for thrust commonly used in ion thrusters, Equation 34.

$$\dot{m}_i = \frac{I_b M}{q} \quad (33)$$

$$T = \sqrt{\frac{2M}{e}} I_b \sqrt{V_b} \quad (34)$$

Next, the specific impulse of the thruster is defined,

$$I_{sp} = \frac{T}{\dot{m}_p g_0} = \frac{v_{ex}}{g_0} = \left(\frac{v_i}{g_0}\right)\left(\frac{\dot{m}_i}{\dot{m}_p}\right) = \frac{\gamma \eta_m}{g_0}\sqrt{\frac{2eV_b}{M}} \quad (35)$$

where γ is the total thrust correction. Finally, the efficiency of ion thrusters must be defined. Assuming singly charged ions, the mass utilization efficiency, which is the ratio of ejected ionized propellant to the total ejected propellant, is below.

$$\eta_m = \frac{\dot{m}_i}{\dot{m}_p} = \left(\frac{I_b}{e}\right)\left(\frac{M}{\dot{m}_p}\right) \quad (36)$$

Similarly, the electrical efficiency of the thruster is the power of the beam divided by the total power input into the system [3].

$$\eta_e = \frac{P_b}{P_T} = \frac{I_b V_b}{I_b V_b + P_o} \quad (37)$$

where P_o is all other power input into the thruster, such as the power required for ionization and the power required for neutralization. The total efficiency of an ion engine is

$$\eta_T = \frac{T^2}{2\dot{m}_p P_{in}} \quad (38)$$

where P_{in} is the total power into the thruster [3]. With the basic equations for ion thrusters laid out, it is now possible to discuss how the grids actually work. In general, ion engines have two grids, an accelerator and a screen. The pair of grids is commonly referred to as the ion optics [3]. The design of the ion optics is vital to the performance, lifetime, and size requirements of an ion engine, which all impact the mission. Though

countless factors go into the design of a grid, one important factor is transparency. Transparency is when the ions escape through the grid, as opposed to the impingement of particles with the grids. If an ion impacts the grid, not only is the lifetime of the grid reduced, but the potential thrust from the responsible ion is lost, and therefore high ion transparency is desired. Additionally, neutral particles produce negligible thrust due to their low velocities, as the electric potential from the grids cannot interact with neutrals. Low neutral transparency is better to have the chance to ionize the particle and create thrust with them as opposed to ejecting the neutrals. Grid design also influences the divergence angle of the plume. In order to maximize thrust, the divergence angle is ideally zero, which occurs when one hundred percent of the thrust is usable. Any plume with a divergence will have a loss proportional to the cosine of the divergence angle, reducing thrust. With a large enough divergence, it is possible for ions to impact other parts of the spacecraft, which can cause damage. An image of an ion thruster is below.

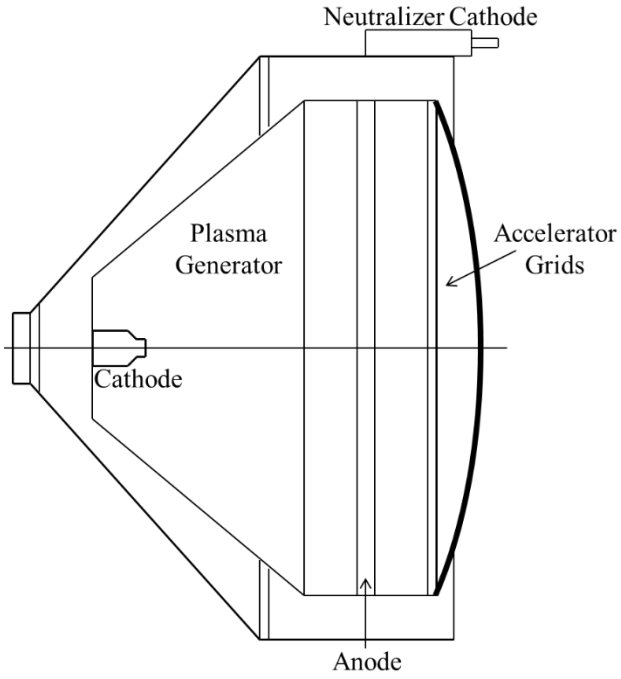

Figure 2. Ion Engine depicting grids, cathode, anode, and neutralizer cathode [3].

The ion current produced by each grid aperture is limited by space charge [3]. Because of this, multiple apertures are necessary to obtain higher beam currents, which correspond to higher thrust, according to Equation 34. In actual operation, due to varying ion current densities and non-uniformities, the current density is not maximized, and instead, more apertures are required to generate the desired performance, which drives up the size. A simplified picture of this process is below.

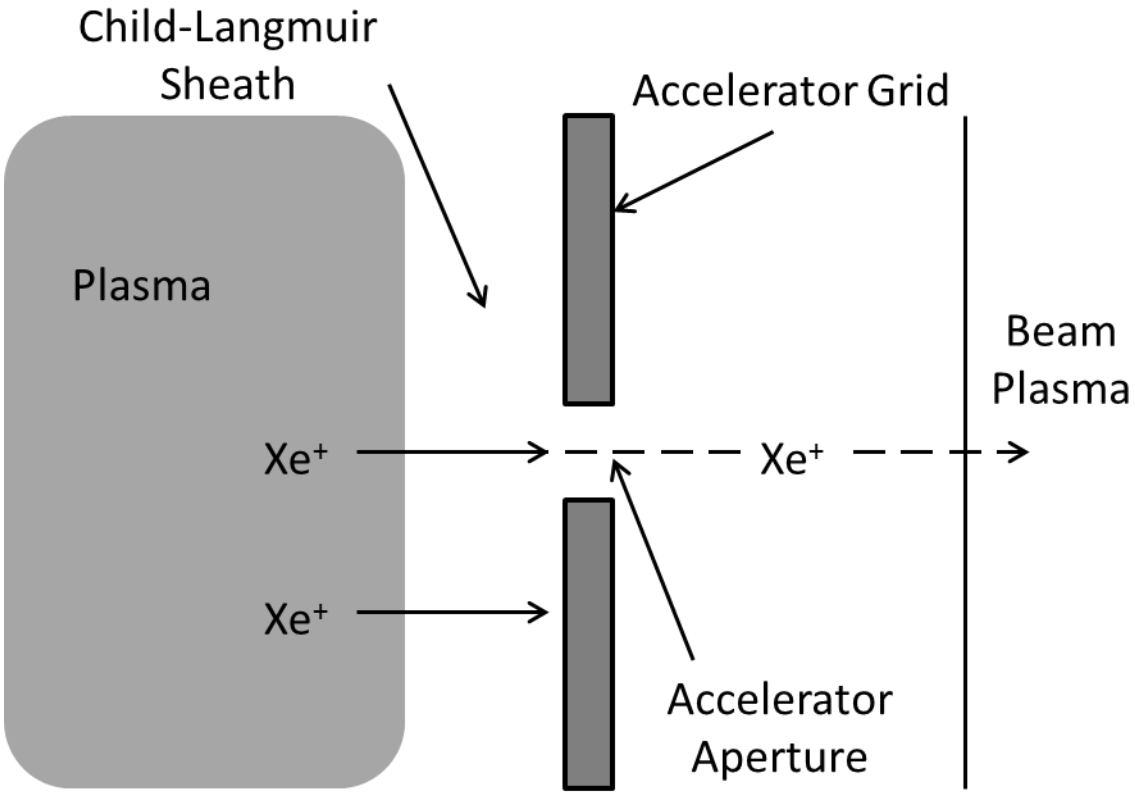

Figure 3. 1-D view of an accelerator grid aperture interacting with a plasma [3].

In the above image, a xenon ion impacts the accelerator grid instead of passing through the aperture. The screen grid, located in between the plasma and accelerator grid, prevents ions from striking the accelerator grid, inhibiting rapid erosion of the accelerator grid. Ions striking the screen do so with little velocity due to the charge of the screen. Ideal designs both focus the beam and protect the accelerator grid from erosion. A term known as perveance relates the amount of current an accelerator can extract and focus for a given applied voltage.

$$P = \frac{I_b}{V^{\frac{3}{2}}} \qquad (39)$$

To maximize the perveance of an accelerator, it is best to make the apertures in the screen larger than those in the accelerator. Doing so causes the flow to avoid contact with the accelerator grid and with the walls of the thruster [3]. If a thruster is in an under-perveance or over-perveance condition, it is possible for flow to impact the accelerator grid, which causes excessive degradation. Overall, the thruster optics serve three purposes. They extract ions from the discharge chamber, accelerate the ions to generate thrust, and prevent electron backstreaming [3], thereby making them a vital piece of the operation of an ion thruster.

2.5 Radio-Frequency Ion Engine

Within electrostatic propulsion, researchers have theorized the usage of numerous different propellants. For these propellants, many forms of plasma generation were successfully created. One of the propellants, xenon, has taken over as the most popular and commonly used. Only three different sources of plasma generation have survived with the use of xenon: electron bombardment discharge, cesium-tungsten surface contact ionization, and a radio-frequency discharge [7]. In order to compare the performance of a radio-frequency plasma generation source with the two other options, each is briefly described.

The electron bombardment discharge is most commonly used in the United States. It fundamentally involves a cylindrical discharge chamber, within which the ionization will occur. Along the centerline of the chamber, there is a cathode, discussed later in this chapter, emitting electrons to bombard the neutral xenon gas. The bombardment process leads to ionization, as an electron with sufficient energy strikes a neutral, causing the

ejection of an electron from the neutral, leaving the initial bombardment electron, an emitted electron, and a positively charged xenon ion. This process is governed by a permeating radial and azimuthal magnetic field, constraining the electrons to gyrate within the chamber [7]. The magnetic fields essentially direct the electrons into the path of the injected neutral xenon propellant and allow enough interaction between the two for large scale ionization, creating a quasi-neutral plasma. Additionally, the magnetic field forces the now ionized xenon particles towards the extractor and accelerator grids. An example of the implementation of the electron bombardment discharge source of plasma generation is shown in Figure 4.

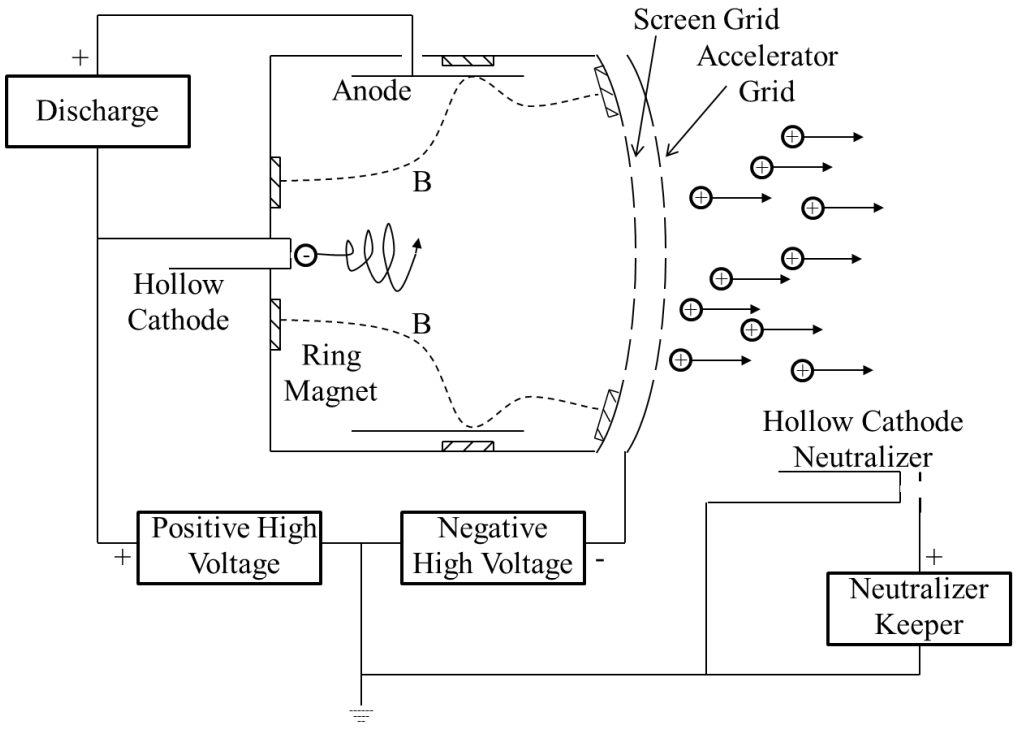

Figure 4. Ring-cusp ion thruster schematic of operation [7].

The next ionization source, surface contact ionization, utilizes the potential difference between a metallic solid and an alkali vapor to create ions. If there is a sufficiently large difference between the work function of the metal and the ionization potential of the vapor, then it is possible, with sufficient heat, to ionize the alkali vapor upon contact with the surface of the metal solid, hence the name surface contact ionization. Cesium and tungsten provide the greatest differential in potential, so it is the most commonly used combination. The most popular application of this ionization source is to force hot cesium vapor through a porous tungsten wafer [7]. This method is common among surface contact ionization because it increases the contact surface area. However, it causes problems with the wafer porosity and alkali condensation, limiting efficiency and lifetime. The inefficiencies within this source of ionization generally override its simplicity, so it is chosen relatively infrequently when compared to the other forms of ionization.

The final ionization method is radio-frequency (RF) generation, the type utilized in the thruster examined in this research. One of the main differences between the bombardment method and the RF generation method is the latter does not require an internal cathode. The external neutralizer cathode is still required. In RF generation, the propellant is ionized through an inductively coupled, annular, self-sustaining discharge [8, 9]. RF ion thrusters generally employ a helical coil energized at a low mega-Hertz frequency. The coil creates an oscillating electric and magnetic field; the former actually causes the ionization and keeps the plasma energized, while the latter constrains the plasma. This setup is convenient because it eliminates the need for an external magnetic field, a component that is normally necessary to contain plasma in internal cathode

designs. Because both the internal cathode and external magnetic field are eliminated, RF ion engines are a relatively simple design and more easily scaled down in size. Figure 5 shows a cross sectional image of a typical RF ion engine with two grids. The circles denoting the RF coil are wrapped around the body of the thruster, but are simply shown at the top and bottom of the image.

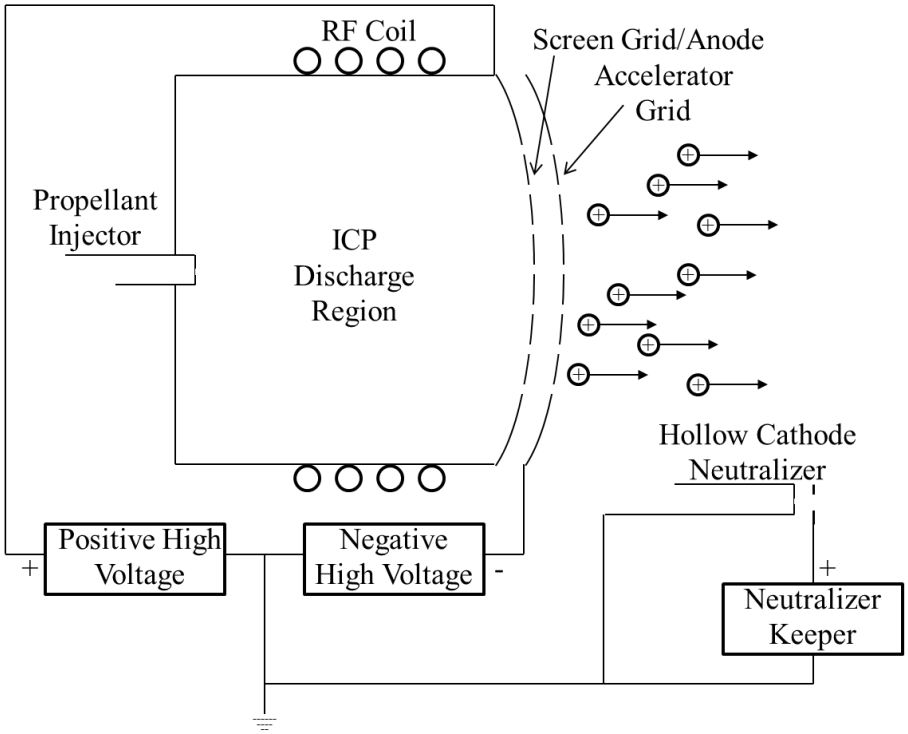

Figure 5. Cross-sectional Illustration of a Typical Two-Grid RF Ion Engine [10].

2.6 Cathode Usage with the Ion Engine

Cathodes are necessary with the use of any electric propulsion device requiring electron generation. As discussed previously, certain forms of ionization generation require a cathode to supply electrons. Additionally, in the case of ion thrusters, a neutralizer cathode is necessary. Because ion engines create thrust by ejecting positive

ions, the spacecraft becomes negatively charged. The process cannot be maintained because of the charge differential created by the removal of positive ions. To negate this process, a neutralizer cathode is implemented. A neutralizer cathode uses one of numerous forms of ionization to generate electrons, which are attracted to the charged plume of the ion engine. Neutralizer cathodes regulate the spacecraft charge and ensure no charge buildup occurs.

In the 1960s, early cathode technology involved heating tungsten filaments to produce electrons. However, tungsten has a high work function, so it was very expensive in terms of energy to produce the electrons. To create electron current densities over 1 A/cm^2, the filaments were heated to a temperature over 2600 K [3]. Achieving such temperatures requires high heater power—power not used for thrust, causing a great reduction in the efficiency of the thruster. Additionally, the lifetime of the tungsten cathodes was mediocre at best, a major problem for space applications [3]. Operation at 2600 K caused rapid evaporation of the filament material. Also, sputtering from exposure to the discharge plasma or ion bombardment reduced lifetimes even further. The combination of these two phenomena caused lifetimes on the order of hundreds of hours [3]. Such a short lifetime deemed tungsten cathodes useful for lab test, where spent cathodes are replaceable, but are simply infeasible for use in small satellite propulsion.

One of the common cathodes for use in space propulsion is the orificed hollow cathode. This system is essentially a hollow cylinder with a plate containing a centered small hole at the end of the cathode. Inside the tube is a cylindrical insert, which is a low work-function material, so a relatively small energy addition is needed to remove an electron. A heating wire is wrapped around the tube to provide the necessary energy, in

the form of heat, to remove electrons from the insert. Subsequently, as the neutral gas, normally the same as the thruster propellant, flows into the cathode, electron bombardment creates plasma. Electron bombardment occurs when an electron strikes a neutral particle with sufficient energy to ionize it, producing the original bombarding electron, an ionized particle, and a free electron from the neutral. From there, the keeper, a positively charged electrode, draws the electrons out of the cathode through the orifice in the plate [11]. Finally, for the neutralizer cathode, the positive potential of the xenon ions in the plume pulls the electrons to create neutrality in the plume. The plasma ions created in the ionization process neutralize the electron space charge, causing hollow cathodes to produce a high current at a low voltage [3].

The structural design of the hollow cathode fulfills three main purposes. First, as the propellant is injected into the cathode, a high neutral pressure region is created, which yields a high density plasma at low temperature. With high plasma and neutral densities and low electron temperatures, the plasma potential is very low. Because of the low potential, the ion bombardment energy impacting the insert is relatively low, eliminating ion sputtering and increases the life of the cathode [3]. Next, the high density plasma around the insert reduces space charge effects, potentially reducing the electron emission current density. Finally, the insert is easy to heat shield with the design, reducing the amount of input energy needed to heat the cathode, thereby reducing losses. A basic sketch of a hollow cathode is shown below in Figure 6.

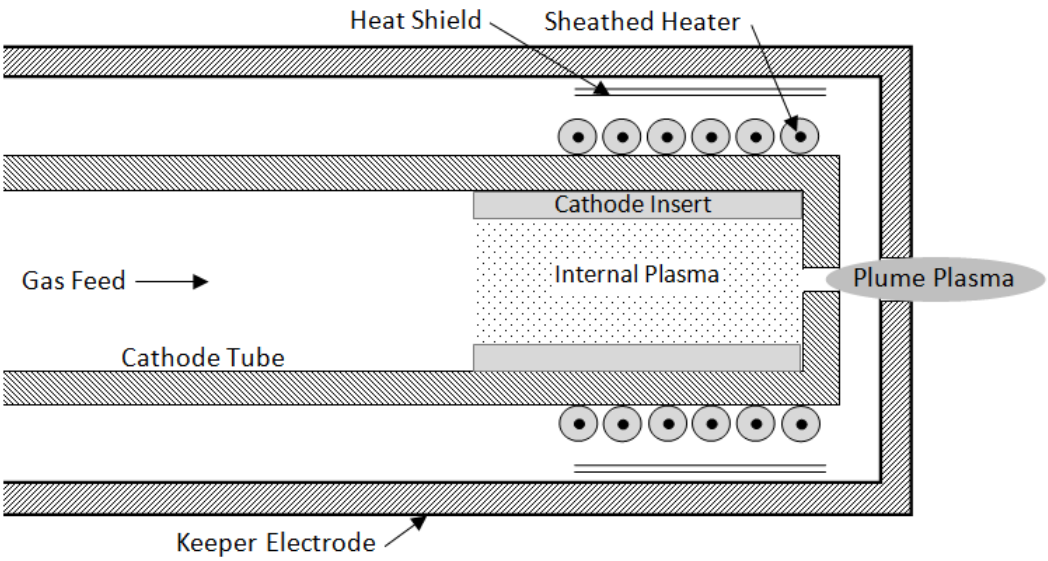

Figure 6. Hollow Cathode Diagram [3].

Orificed hollow cathodes have an electric field inside the insert region and at the keeper; this combination is known as the Schottky effect, resulting in a lower effective work function [11]. Lower work functions correspond with a smaller energy requirement to produce electrons. In effect, a chemical reaction causes the reduced work function as gases move to the surface of the insert as the temperature approaches the operating point. Because the process relies on a chemical reaction, the reactants need to be very pure to achieve the proper work function reduction. For this reason, orificed hollow cathodes are extremely sensitive to contamination from oxygen and gaseous water [11]. In order to mitigate this process, the cathode goes through conditioning, where it is slowly heated to remove all contaminants before operation. The conditioning process precedes the firing of the cathode and can take anywhere from tens to hundreds of minutes [12]. If contaminants somehow survive the conditioning and are in the cathode for operation, the cathode becomes poisoned, and it loses some or all of its capabilities. Assuming no

poisoning occurs in the lifetime of the cathode, the limiting factor becomes the supply of the insert. Once the insert is completely used, the cathode will no longer operate.

The keeper electrode has numerous functions within the cathode. It assists in the turn-on of the cathode discharge, maintains the temperature and operation of the cathode if normal operation is momentarily disrupted, and protects the cathode orifice plate and heater from life-limiting ion bombardment. Because the keeper is positively biased, it is simultaneously able to draw out electrons to start the thruster and block positive propellant ions from striking the cathode during regular firing. The combination of the above factors makes the life of the keeper electrode vital to the life of the cathode, and therefore to the life of thruster [3].

Operationally, the external heater is generally not used. Hollow cathodes are able to maintain the required temperature through three types of self-heating methods, thereby making the heater unnecessary. The first is called orifice heating, which is due to the orifice having a small opening, causing a high internal pressure. High pressure causes the discharge plasma to become very resistive, causing heat transfer into the plasma. From there, the plasma transfers the heat to the walls of the orifice by convection. The insert then gains heat from the orifice through both conduction and radiation. Another form of heating is known as ion heating. It occurs when ions in the insert region pass the sheath potential near the insert and strike the surface, transferring energy through ion bombardment. The final form of self-heating in orificed hollow cathodes is electron heating. Electron heating occurs in cathodes where the internal pressure and discharge current are high, causing very high plasma densities around the insert region. In this scenario, some electrons in the Maxwellian electron distribution have enough energy to

penetrate the sheath potential and strike the insert surface, depositing energy. The type of heating dominating any orificed hollow cathode depends on the geometry; small orifices promote orifice heating; large orifices cause a combination of electron and ion bombardment, and no orifice yields ion bombardment [3].

The final form of cathode discussed in this paper is the electride hollow cathode. It is still in the experimental phases, as it is a relatively recent development. However, the electride cathode operates in a manner very similar to the orificed hollow cathode. The term ‘electride’ refers to the insert material, which is the real difference in the new technology. Typical work functions for the orificed hollow cathode with inserts of lanthanum hexaboride and cerium hexaboride are near 2.7 eV, and barium-impregnated porous tungsten is around 2.1 eV. These materials require the traditional hollow cathode with a heater to start the electron production. Electride cathodes use an insert with a much lower work function, such as calcium aluminate (C12A7), which has a measured work function as low as 0.6 eV [13]. Because the insert work function is so low, electride cathodes do not need a heater to emit electrons. Therefore, they avoid the conditioning stage of operating as room temperature is adequate for firing. For start-up, high gas mass flow, around 20 times the nominal flow rate, is necessary, along with a high keeper voltage. In general, a kilovolt is supplied to the keeper and approximately 30 sccm of xenon is required to initiate plasma generation [13], though these numbers vary depending on the size of the cathode. After the electride cathode ignites, the mass flow rate is reduced to the desired level, and the keeper transitions into a current-limited mode. The cathode technology used in this research is a heaterless electride cathode.

2.7 Sizing of the Ion Engine

The performance of ion engines is correlated to their size. There is a limit on the small end of the spectrum for feasible ion engine operation, due to power processing limitations and space charge [3]. On the large end, the power processing unit becomes prohibitively massive, making their use infeasible. Therefore, there is a range of operation in which ion engines are best suited. This section will focus on the scaling down portion of sizing, as this research focuses on a micro thruster.

A study by Michael Patterson et al. found a relationship between engine sizing and neutral loss rate, related to the inverse of propellant utilization efficiency. As a high propellant utilization efficiency is desired, a low neutral loss rate is best. The group found a dependency of neutral loss rate on discharge chamber length. If the length of an ion thruster decreases, so does its propellant efficiency, and therefore the thruster efficiency. Also, they found obtaining useful propellant efficiencies with xenon is very difficult for discharge chambers less than five centimeters, as they require a very large beam current and power density [14].

Another factor impacting the scaling down of ion thrusters is cathode technology. If one were successfully able to make a thruster half a centimeter in diameter, for example, it still may not be plausible based on mass flow rates. If the thruster and the neutralizer cathode required equal mass flow rates for operation, the specific impulse of the thruster system is essentially halved, because half of the usable propellant goes into the neutralization of the plume [15]. Therefore, the mass flow requirement of cathodes is of vital importance for small ion thrusters. The ratio of thruster mass flow requirements

to the total mass flow is a performance loss. Analysis of this ratio is necessary before implementation on-orbit.

RF ion thrusters are more easily reduced in size than thrusters with other plasma generation sources because they require neither an internal cathode nor permanent magnetic structures to create plasma [6]. The simplicity of RF ion thrusters make physical scaling simpler, but maintaining efficiency and performance as size decreases is still a difficult feat. Research conducted by Dr. Michael Tsay indicates that one of the most challenging aspects is overcoming the diminishing coil inductance as the geometry shrinks, as well as the fact ohmic heating becomes a dominant loss factor as power magnitudes scale down [6]. Table 1 shows a compilation of general guidelines, created by Busek, for scaling down an RF ion thruster.

Table 1. Guidelines for scaling down an RF ion thruster from the developer of the ion engine studied in this research, Busek Co. Inc. [6].

Design Parameter	Preference	Issue
Grid Diameter	An ideal grid diameter is based on a target thrust, assuming high grid transparency and known beamlet current.	None, but may need to increase the grid diameter to match the actual chamber size. The grid's open fraction will then be reduced to meet the target thrust.
Discharge Chamber Diameter	Matching the ideal grid diameter.	If the chamber is too small, the coil inductance will be too low and the ohmic heating loss will be very severe.
Discharge Chamber Length	As short as possible for minimizing ion wall loss.	A short chamber limits the number of coil turns and its inductance value.
Operating Frequency	Producing a skin depth that is 1/2-2/3 of the chamber radius.	The coil's effective series resistance and ohmic heating loss increase with increasing frequency
Number of Coil Turns	As high as possible for maximizing coil inductance	A longer coil translates to a higher ion wall loss. It also increases the coil resistance and ohmic heating.
Coil Cross Section Diameter	As large as possible for minimizing coil resistance and ohmic heating loss	A larger cross-section translates to fewer coil turns, which reduces the inductance

There are many obstacles to reducing the size of an ion engine. The Busek 1cm Micro Radio-Frequency Ion Propulsion System is one of the smallest ion engines in existence, so performance characterization is vital to understand the potential of micro ion engines.

III. Methodology

3.1 Chapter Overview

The purpose of this chapter is to describe the methodology used in the completion of this research. Initially, the experimental setup used did not operate successfully, so this section will discuss a few of the issues associated with the setup, what operations were needed to overcome them, and the adjustment to the final experimental setup. Unfortunately, all experimental setups attempted at the Air Force Institute of Technology (AFIT) were unsuccessful due to an likely incompatibility with the vacuum chamber passthroughs used, so the final setup occurred on location at the manufacturer of the ion engine, Busek Co. Inc, in Natick, Massachusetts.

3.2 Vacuum Chamber Capabilities

For the majority of this research, the Space Propulsion Application Simulation System (SPASS) Laboratory, located at AFIT on Wright-Patterson Air Force Base, was used. Housed in the lab is a high-capacity vacuum chamber, within which the 1cm RF ion engine, along with the neutralizer cathode, was installed. The vacuum chamber is 1.8 m in diameter, with a length of 2.5 m, equating to a total volume of approximately 6.4 m^3. It is capable of pumping 16,000 liters per second of xenon. The chamber is reduced from atmospheric pressure to nearly 10^{-4} torr through the use of a Leybold Screwline SP 250 roughing pump. Through the use of a Lester 300 mini-convectron gauge, the pressure is measured as the 0.1 mtorr point is approached. Next, the gauge initiates the switch from the roughing pump to the four CVI TM 500 and two CVI TM 150 cryogenic pumps,

capable of dropping the pressure to 10^{-7} torr by reducing the temperature of the cryo-head assembly, acting as a cold trap and condensing gases.

3.3 Flow Controller

The vacuum chamber is equipped with four MKS model 180A mass flow control valves, through which the propellant for the thruster and neutralizer cathode flows. Three of the four valves have a range of 0 to 10 SCCM and the fourth has a range of 0 to 50 SCCM. The four valves are controlled by an MKS Type 247 flow controller, shown in Figure 7 below, which is capable of regulating all channels simultaneously with an error of less than 0.01%.

Figure 7. MKS Type 247 flow controller, able to regulate four channels at once.

In the SPASS Laboratory, xenon and krypton are the propellants, both with 99.99% purity. The setup for the flow control system can be seen in Figure 8, below.

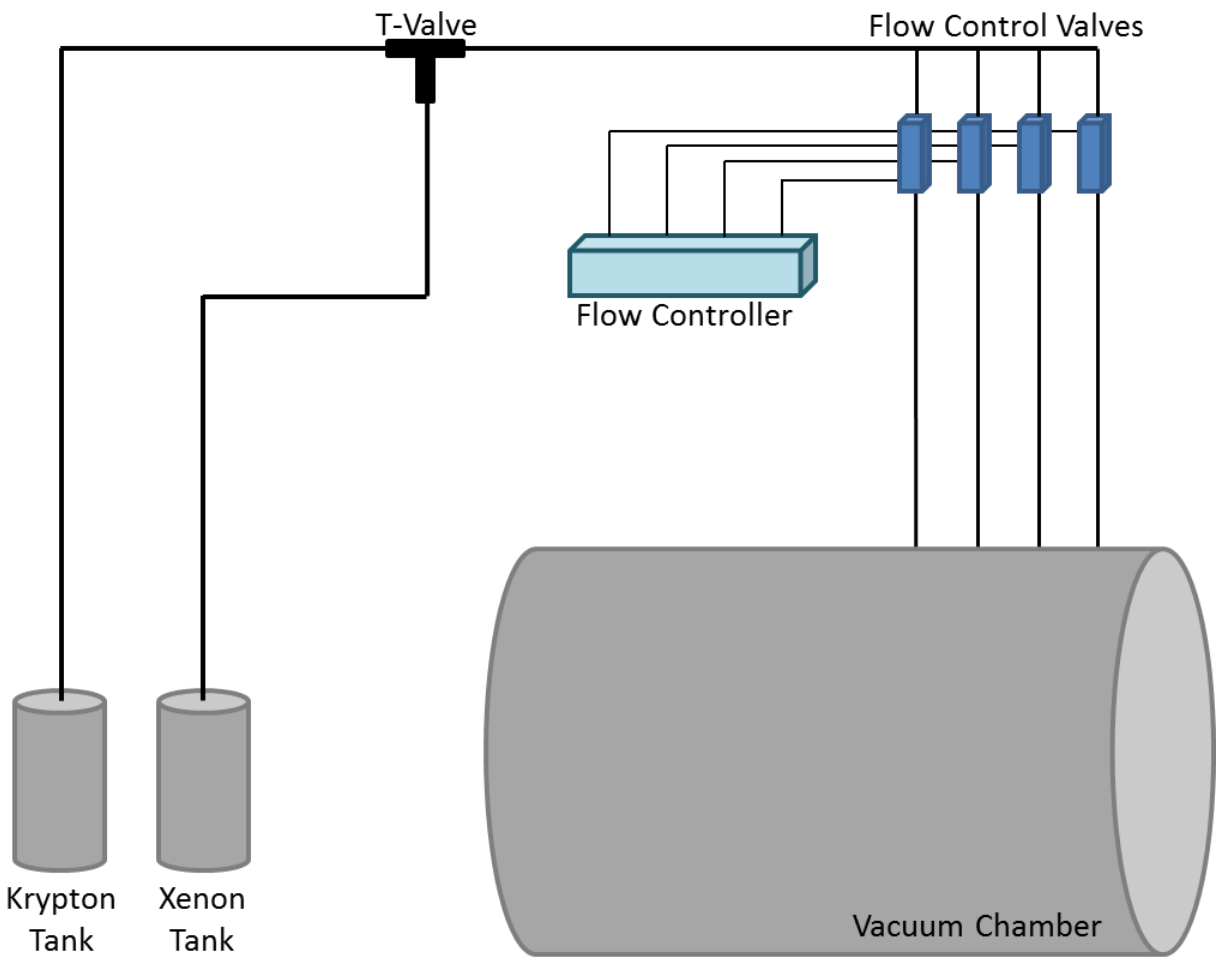

Figure 8. Schematic of the relationship between the propellant fuel tanks, flow controller, and vacuum chamber.

For this experimental setup, only two of the gas flow lines were needed: one line to supply the neutralizer cathode and one for the thruster itself. The other two lines allow for multiple simultaneous thruster tests in the chamber without the need to adjust propellant lines, which would require bringing the chamber back to atmospheric pressure, a lengthy process. With this setup, two separate anodes and cathodes can be used in the chamber in a single session, with the ability to switch between krypton and xenon gas, as required.

3.4 Thruster Support

Before the thruster was mounted inside the vacuum chamber, a support structure needed designing. The base of the support was designed to attach to the thrust stand through four bolts and nuts. The upper region of the stand was designed to support the thruster through a single threaded whole, which is how the manufacturer mounted the thruster [15]. One point of contact was deemed sufficient by the manufacturer because of the light weight of the thruster. However, to ensure conditions remained the same throughout testing, a second support was desired to prevent any unwanted rotation about the single screw. Therefore, a stand for the thruster was designed in SolidWorks, seen below in Figure 9.

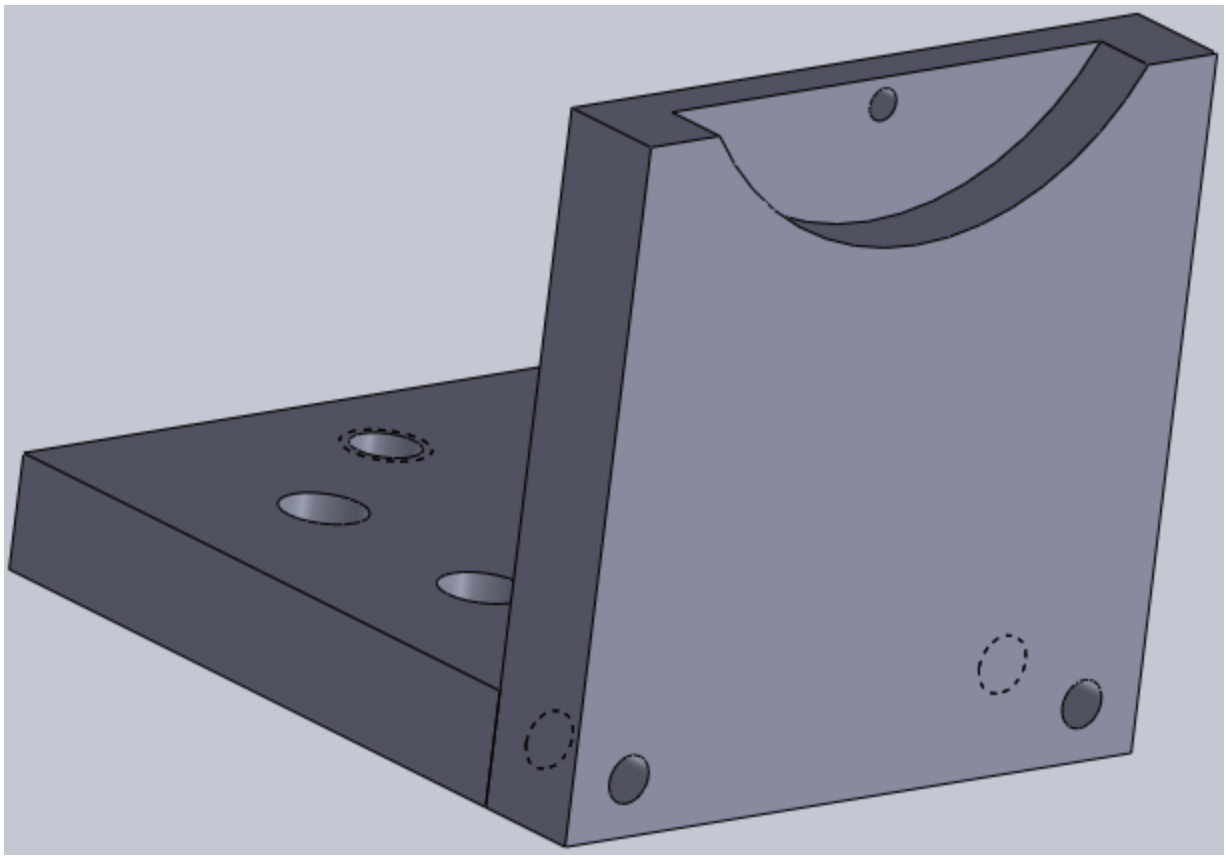

Figure 9: Support design, created to mate the thruster with the thrust stand.

After the stand was designed, it was fabricated in an in-house machine shop using PEEK (polyether ether ketone) plastic because of its desirable insulation properties. The base of the support contains five holes. Four are to mount to the thrust stand, and the fifth is to provide a potential mounting option for the neutralizer cathode, a feature that turned out unnecessary. On the vertical portion of the stand, there are two holes at the bottom to attach the two pieces together, using a threaded insert in the base of the support. Finally, at the top of the vertical piece, there is a hole inside an arc-shaped cutout. The diameter of the circle from which the arc was created corresponds to the diameter of the outer casing of the thruster, so it has support from both the screw and the arc, preventing it

from moving. An image of the completed stand is shown below in Figure 10, with a ruler for scale. Each piece of the stand is 1.5 inches square.

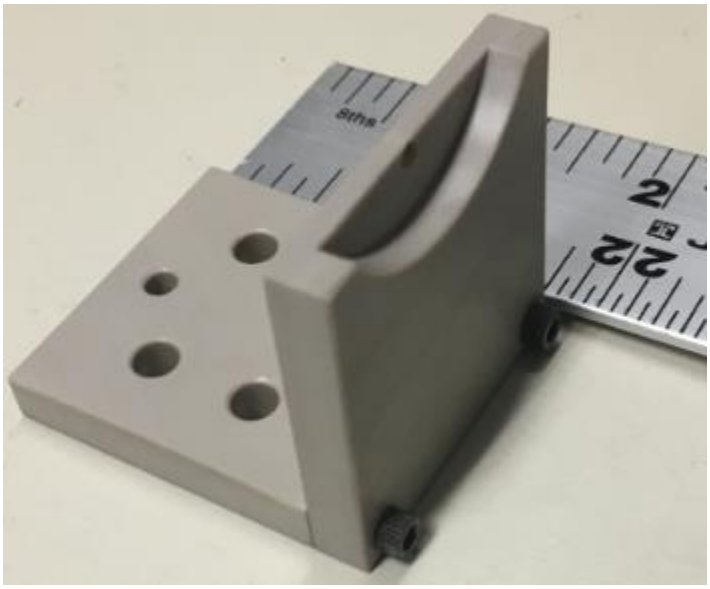

Figure 10. Thruster support, created out of PEEK plastic.

3.5 Thruster Mount

The ion engine was mounted to the stand and installed in the chamber to confirm operational abilities of the thruster, followed by a planned test to find the divergence angle of the plume. Due to space limitations in the vacuum chamber, the thruster was not mounted in a single position to measure both divergence and thrust information, so the testing involving the thrust stand was planned to occur after the divergence testing. Because of the setup of the chamber, the thruster was mounted to fire along the axial direction to gather information with a Faraday probe. The vacuum chamber houses an Aerotech three-axis translational stage and the thruster was mounted on it. On each of the

three independent axes, the translational stage is able to provide 60 cm of range, with errors less than one millimeter. Using this technology, it is possible to move the ion engine to a location centered in the chamber and at the proper height for the Faraday probe to take data. An image of the setup is shown below, in Figure 11.

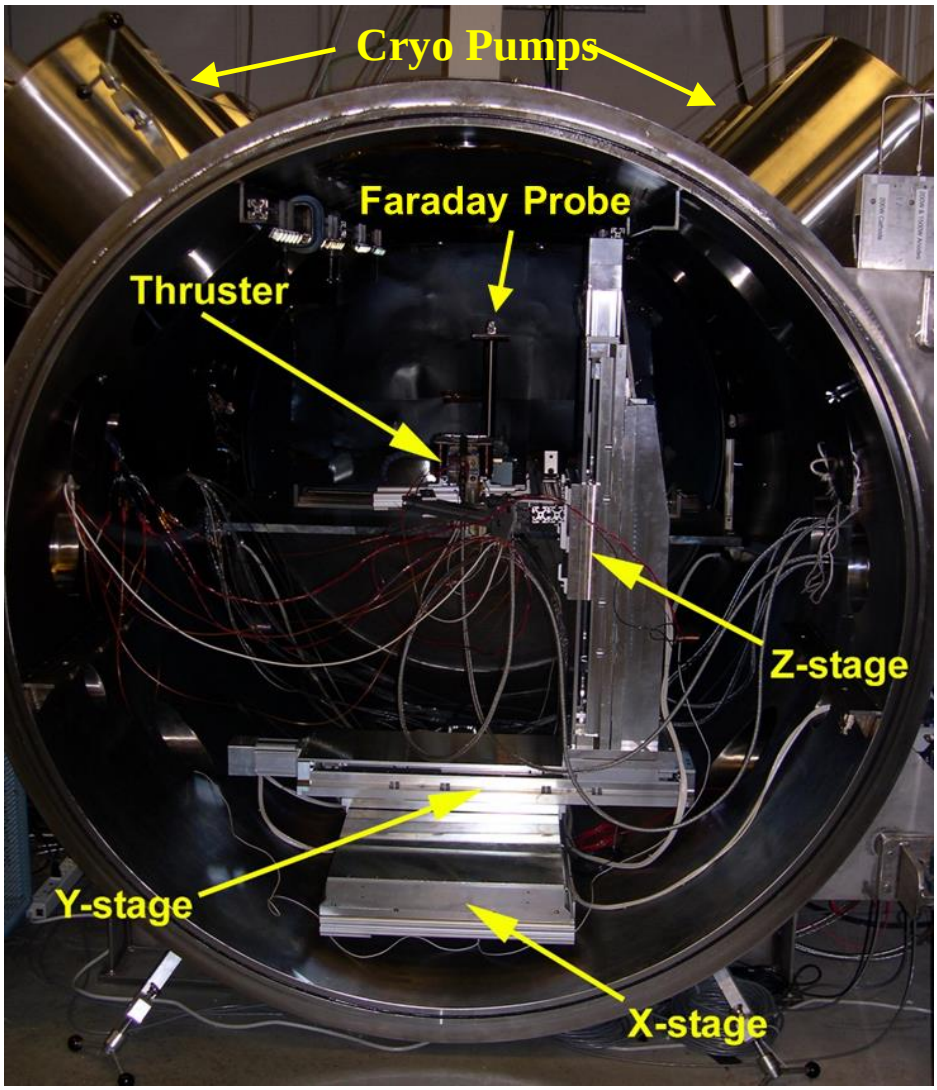

Figure 11. Vacuum chamber located in the SPASS Laboratory. The cryogenic pumps, thruster, Faraday probe, and three axes of the translational stage are labeled.

3.6 Faraday Probe

The Faraday probe is mounted to a custom made stage created by the manufacturer of the probe, Plasma Controls. This stage is capable of two axis translation and rotational motion in the third axis. Therefore, it is able to translate in an arc around the thruster while remaining the same distance away. Additionally, as the Faraday probe traverses the arc automatically, it has the capability to stop at each position and rotate to ensure the probe collects the highest current density from the beam. A basic schematic of the motion of the Faraday probe inside the vacuum chamber is shown in Figure 12.

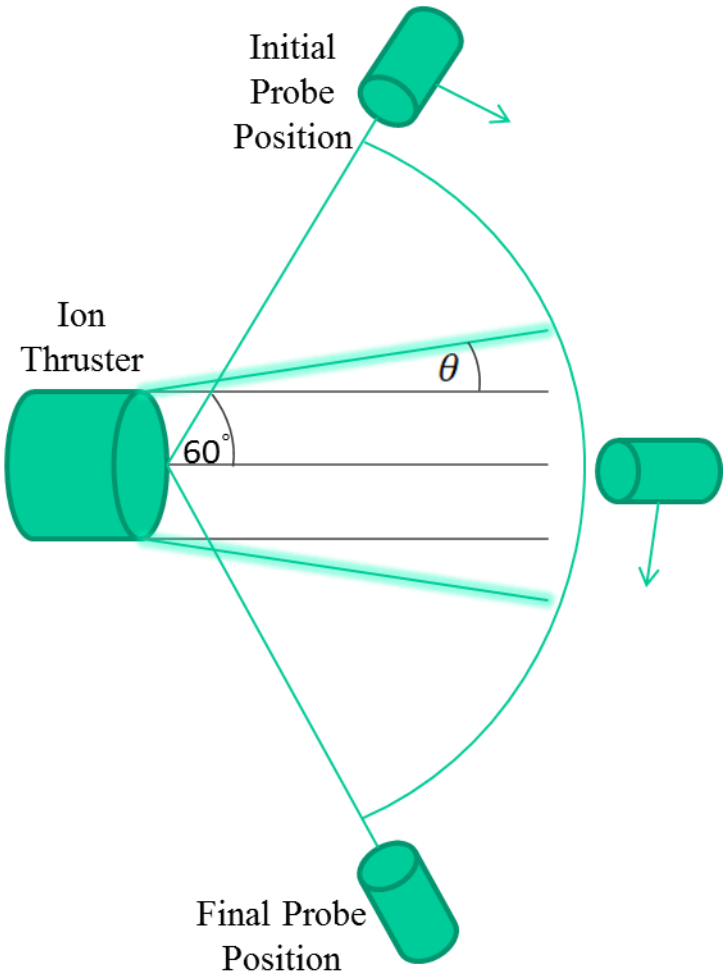

Figure 12. Schematic of the action the Faraday probe will take upon its translational stage. The probe starts outside of the thruster's beam, then moves in an arc pattern, passing through the plume, and exiting the other side. The probe collects current density information at all points along the arc.

Though the above image does not depict it, the Faraday probe rotates as it moves through the arc to ensure it finds the highest current density for each given location. Because the thruster is mounted to a three axis translational stage, the Faraday probe is able to collect data from numerous different distances from the thruster face. After each test, the thruster is moved forwards or backwards as necessary to obtain a detailed plume

profile, indicating the divergence angle at numerous locations axially. The Faraday probe electrical diagram is shown in Figure 13, below.

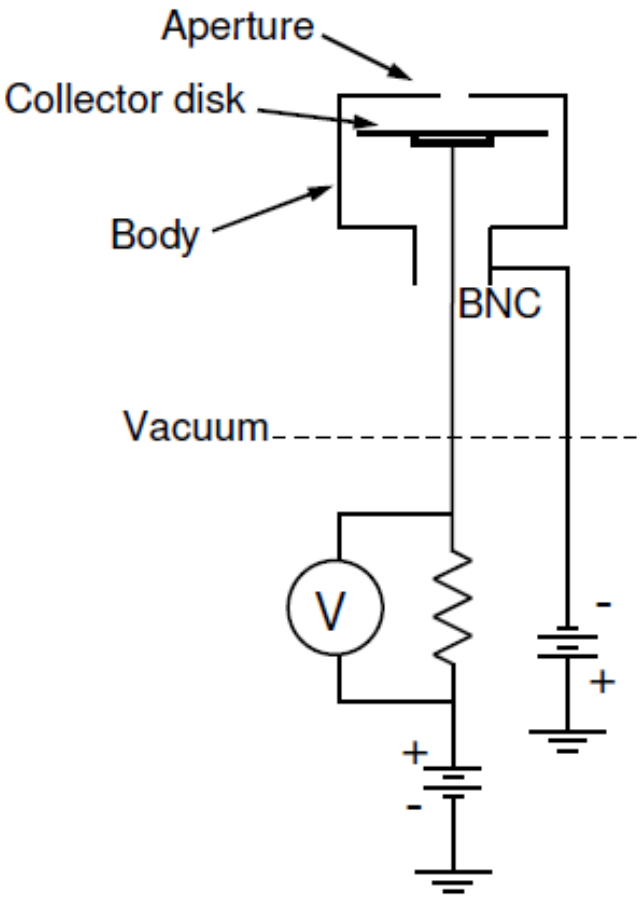

Figure 13. Faraday probe electrical diagram. The top half of the image is inside the vacuum chamber, with the biased aperture and collector disk protected by the body. A BNC cable transmits information outside the vacuum chamber, where measuring the voltage drop across a known resistance yields current density information [16].

The negatively biased body protects the positive collector disk, which senses the xenon ions that strike it. The aperture is a circle with a diameter of 0.015" is biased to a potential of -30 V in order to prevent any electrons from impacting the collector disk and skewing the data [16]. The collector disk is at a potential of 30 V to ensure only high

energy ions hit the collection plate. Through a BNC connection, the current density is calculated outside of the vacuum chamber using a voltage drop over a known resistance. The current density is equal to the number of millivolts of the drop over the product of the resistance and the aperture area [16]. An image of the actual Faraday probe is shown below, in Figure 14.

Figure 14. Faraday probe, provided by Plasma Controls [16].

3.7 Secondary Flow Controller

Before the Faraday probe can measure the current density, the thruster must first fire. As previously mentioned, this setup uses two separate gas flow lines, one for the

neutralizer cathode and one for the thruster. The neutralizer cathode requires 10 SCCM of xenon, as well as an initial high voltage, to start operation. After the cathode lights, the gas flow can reduce to the nominal 0.5 SCCM. Both 10 SCCM and 0.5 are within the range of operation of the MKS model 180A mass flow control valves, so no further modifications were necessary for the neutralizer cathode gas flow. For the thruster, however, nominal mass flow rate is 0.05 SCCM, and such a small flow is not attainable with the given mass flow control valves. In order to obtain more precision with the mass flow, a second flow controller was added in series after the first one to further reduce the propellant flow to usable levels. The mass flow controller of choice is the Omega FMA-2601A, with a maximum flow rate of 0.5 SCCM. It has an error of less than 1%. In order to achieve the desired mass flow, the first flow controller was set to 10% to bring the flow from 10 SCCM to 1, and then the second controller was set to 5% to further reduce the flow to 0.05 SCCM.

Due to the setup of the tubing near the vacuum chamber and the port through which the gas actually enters the chamber, the Omega flow controller was situated about a foot from the chamber exterior wall. With only eighth inch tubing as support, the flow controller started to bend the tubing and Swagelok connectors, causing a leak in the vacuum chamber. When it was determined that the flow controller had caused the leak, it was apparent that a support was necessary to bear the weight of the controller, which had too large of a moment arm for the tubing to hold without deformation. Using SolidWorks, an L-bracket was modified to mount to the vacuum chamber port, with two slotted screw holes to attach the flow controller at whatever variable distance was required. An image of the bracket is shown below, in Figure 15.

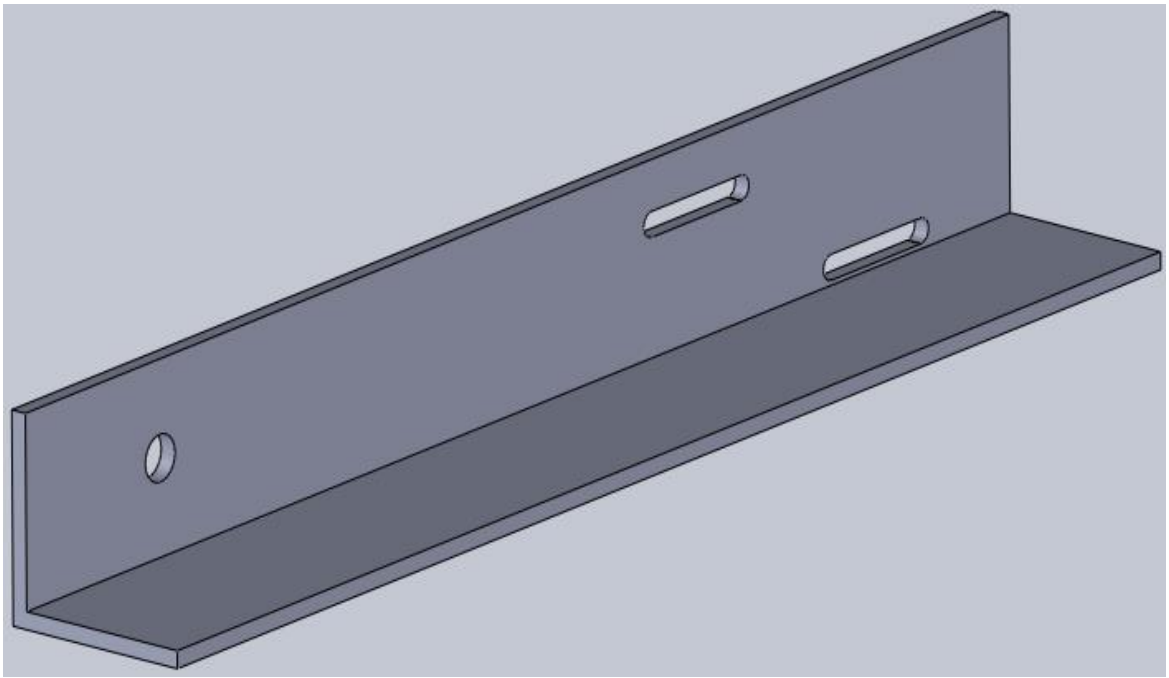

Figure 15. Design of a support for the Omega flow controller.

After replacing the bent components of tubing and Swagelok connections, the support structure was installed to prevent further damage. Due to space restrictions, the slotted screw holes were not usable, as the flow controller had to be mounted vertically instead of horizontally to avoid other tubing. Despite the inability to mount the controller to the support, the tubing provided enough stability to keep the controller on the support, while the support actually took the weight off the tubing. Using the setup shown in Figure 16, below, the vacuum chamber was able to return to its normal operational ability, indicating the leak was fixed.

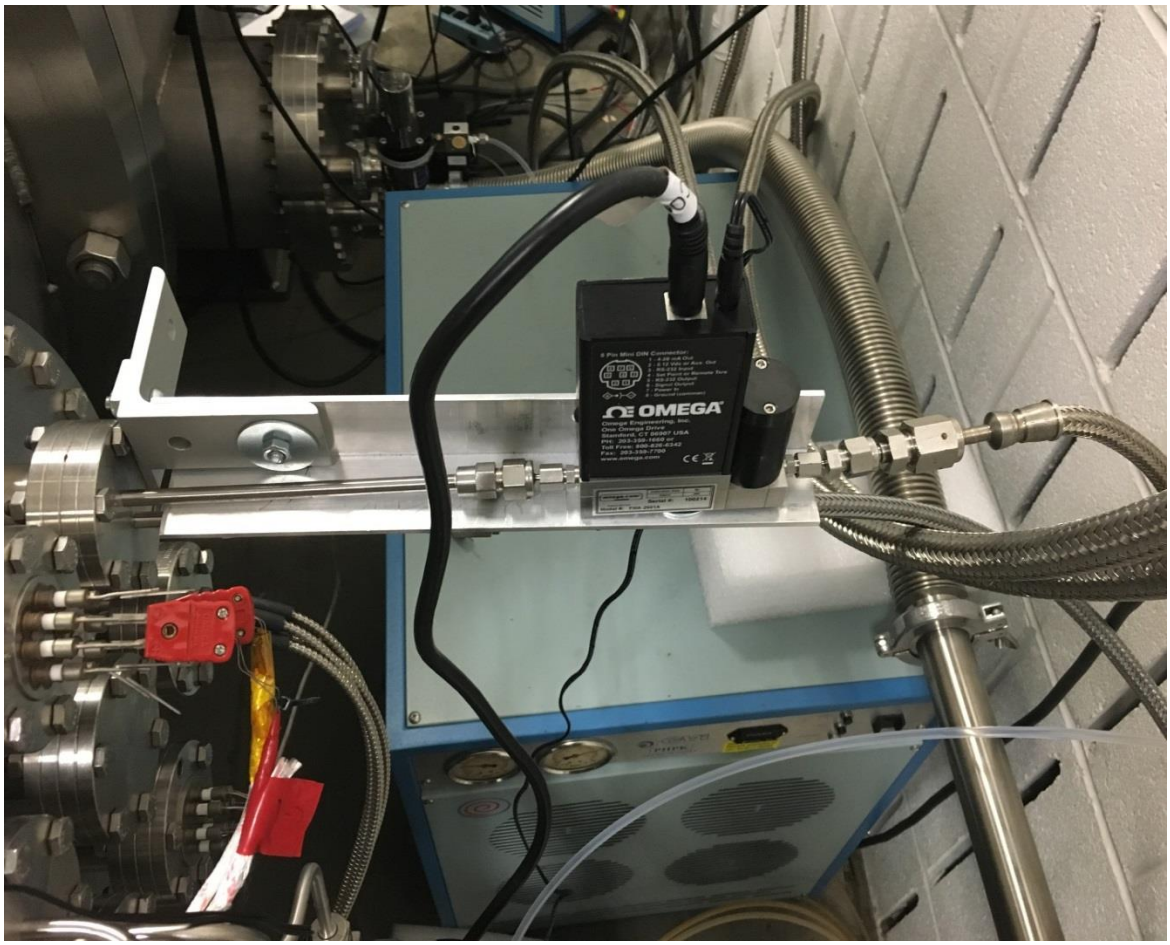

Figure 16. Omega flow controller mounted upon the support and connected to the vacuum chamber, preventing any tubing from bearing the weight of the flow controller.

3.8 Power Processing

Next in the experimental setup is the power processing required to use the 1cm ion engine. The initial setup involved a Spellman SL1200 high voltage power supply for the neutralizer cathode, an Extech Instruments 382260 80W power supply for the RF board on the power processing unit (PPU), and a Bertan Series 230 high voltage power supply to run the rest of the PPU. These three power supply units, along with the PPU and a computer with LabVIEW, are the only components required to operate the thruster

electrically. The LabVIEW is meant to control both the radio-frequency plasma generation process and the screen and accelerator voltages, and using these programs, along with the mass flow controller and cathode power supply, the whole system is controllable.

However, during setup and testing of the power supplies, the leads to the RF board and to the rest of the board were swapped, leading to a momentary voltage approximately 5.5 times the design amount going through the PPU portion that conditions the power for the screen and accelerator grids. The error was due to significant failed troubleshooting to get the PPU fully operational, consisting mostly of communication errors between the computer and the PPU, which led to the mistake of switching power supply lines. This voltage, though brief, damaged the PPU, and rendered all but the RF board inoperable. Rather than send the damaged component back to the manufacturer, which would have likely added upwards of a month to the testing timeline, a work-around was created. Using power supplies linked directly to the screen and accelerator grids, the appropriate voltages and currents were supplied, rather than going through the PPU for power conditioning.

In order to supply the voltage levels necessary to operate the screen grid, which requires potentials up to 1800 V, a Glassman High Voltage PS/EK03R200-GW9 power supply was obtained. For normal operation, the positive and negative terminals from the power supply are connected to the PPU. From there, the PPU used leads that connected to the screen grid, accelerator grid, and common ground. To bypass this step, the high voltage power supply positive output was connected directly to the screen grid, with the negative terminal linked to the common ground.

Similarly, a Stanford Research Systems PS250 power supply was used to supply the 200 V potential to the accelerator grid. In order to start the thruster, the neutralizer cathode must first ignite. As mentioned previously, 10 SCCM of xenon and a kilovolt of potential must work in concert to start the flow of electrons. Once the neutralizer is operating in steady state, with a 0.5 SCCM gas flow and a much lower potential, the thruster must draw in some electrons to start the plasma generation process. To do this, the polarity of the accelerator grid is quickly switched from its normal -200 V to 200 V, then immediately back to -200 V. This process allows seed electrons to enter the discharge region where the plasma is generated. Normally, this would be accomplished by a button in LabVIEW that toggles accelerator grid polarity. The damage to the PPU prevented the use of the program that contained the toggle button, so a manual switch was implemented.

Busek, Co. Inc. provided an electrical wiring diagram of a double pole single throw ignition switch to attach to the power supply to bypass the LabVIEW toggle button, shown below in Figure 17.

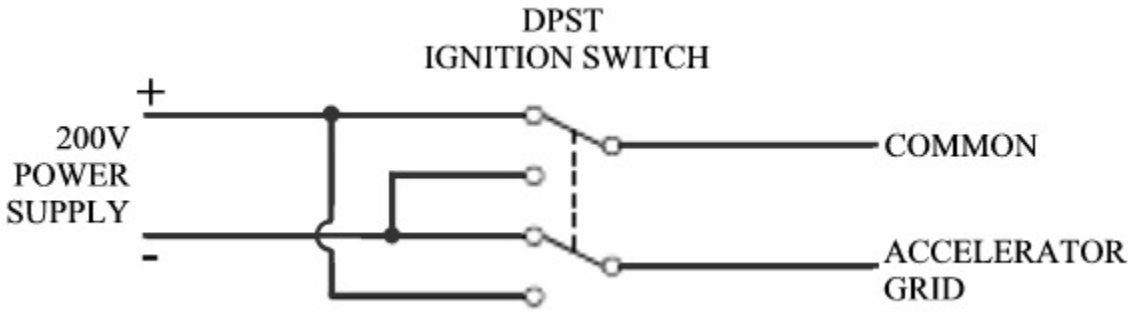

Figure 17. Ignition switch electrical diagram, required for the startup of the ion engine [15].

However, upon implementation, the desired voltages were not successfully output. To mitigate the issue, a double pole double throw switch, with six terminals instead of four, was installed. The positive and negative power supply terminals were connected to one pair of terminals on the switch, then connected again, but in the opposite order, on the opposite pair of ports. Then, the middle two ports, the outputs, were connected to the accelerator grid and common ground, respectively. Upon testing prior to attaching the toggle switch to the accelerator grid, the outputs yielded the desired positive and negative 200 V. However, once attached to the accelerator, the positive output was correct, but the negative option output no voltage. Unable to fix the problem with any other reasonable solution, the power supply formerly attached to the PPU, the Bertan Series 230 high voltage power supply, was attached to the toggle switch.

With one power supply set to 200 V and attached to one pair of terminals and the other set to -200 V and attached to the opposing terminals, the desired output was obtained by turning on both power supplies and simply flipping the toggle switch to send whichever voltage was desired. Therefore, to start the thruster, the switch was set to the negative option, then toggled to the positive for about one second, and finally reverted back to the negative for normal operation. Both power supplies used for the accelerator grid had the capability to output both positive and negative potential, but unfortunately, the bias cannot be altered while the power supplies were operational. The process of drawing in electrons to initiate plasma creation needs to be quicker than the time it would take to turn off the supply, switch the polarity, and turn it back on. Because of this issue, the toggle switch was kept as the final solution. An image of the switch, surrounded by an insulation box and attached to a work station, is seen in Figure 18, below.

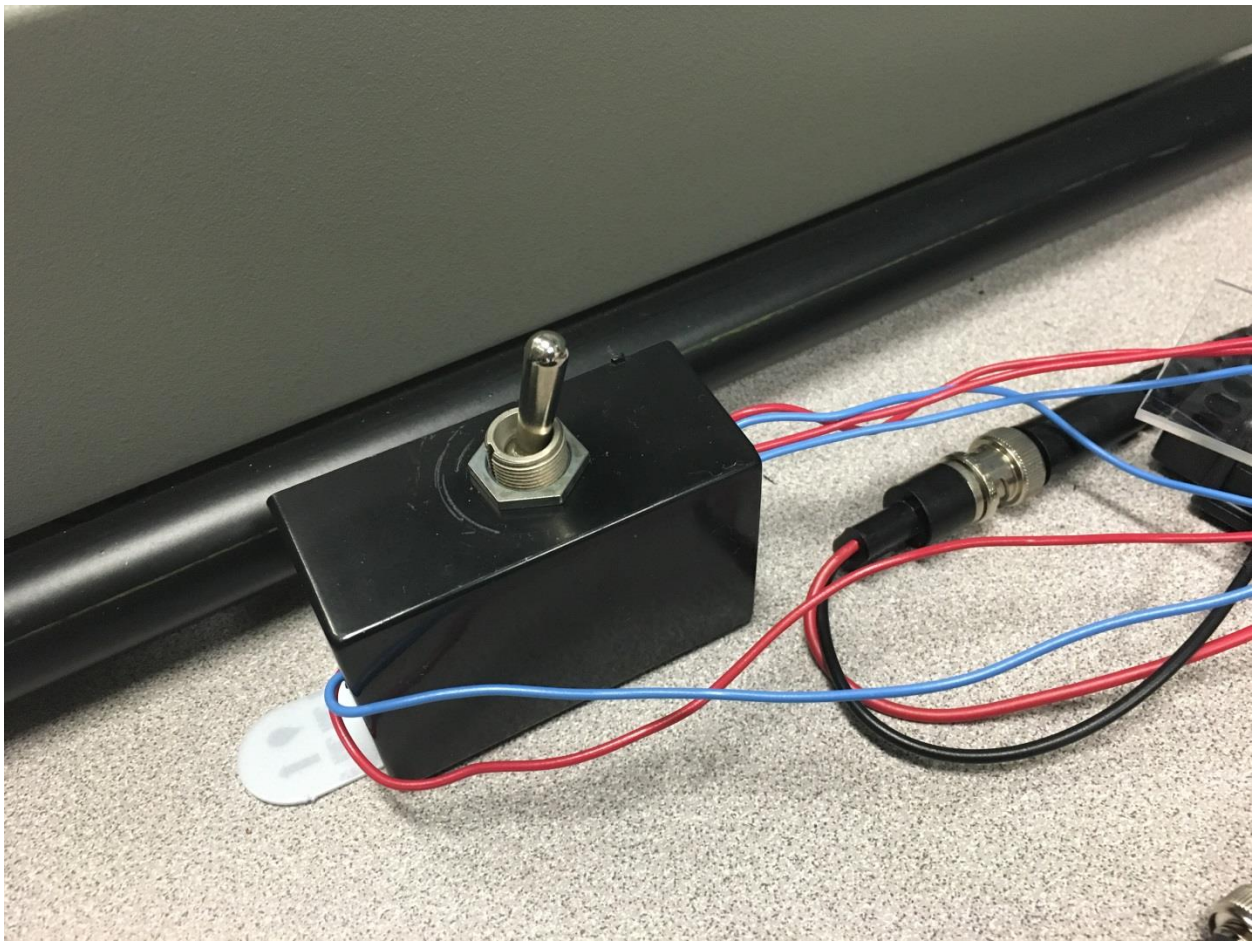

Figure 18. Double pole double throw toggle switch, used to reverse the polarity of the accelerator grid in the process of starting the ion engine.

It is noticeable in the above image that there are four wires leading to the box on the right side, which are the positive and negative leads from the two power supplies, and two wires trailing from the box on the left, which are the outputs. The setup to operate the thruster involved a power supply for the RF board, two power supplies to cover the positive and negative requirements of the accelerator grid, and two high voltage power supplies to drive the neutralizer cathode and supply voltage to the screen grid. The five power supplies, combined with the computer with LabVIEW to operate the RF board, the PPU, and the mass flow controllers for both the neutralizer cathode and the thruster, are

the entirety of the setup on the exterior of the vacuum chamber. An image of this setup is shown below, in Figure 19.

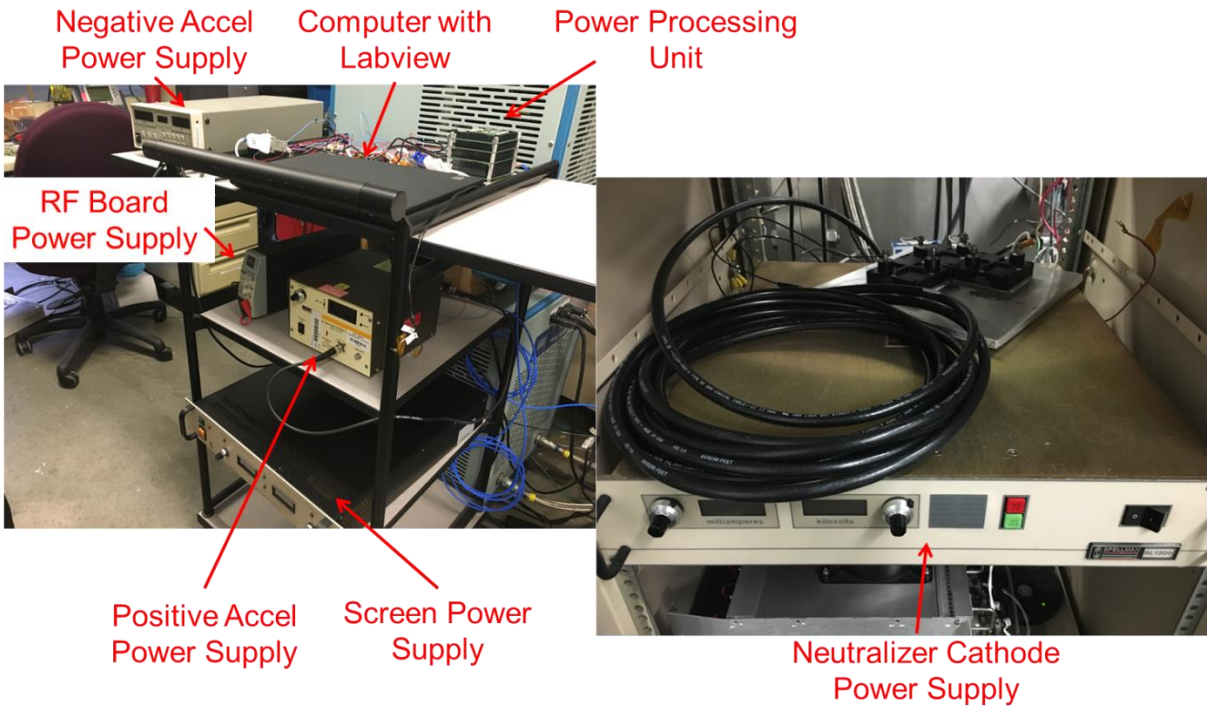

Figure 19. The experimental setup located on the exterior of the vacuum chamber. The five power supplies, in conjunction with the LabVIEW capable computer and the power processing unit, control the thruster.

3.9 Thrust Stand

For the thrust measurement portion of the experiment, a Busek, Co. Inc. torsional balance system was obtained. The thrust stand is designed to accurately measure micro-Newton forces, and the 1cm ion engine produces thrust within the micro-Newton regime. An image of the thrust stand is shown in Figure 20, below.

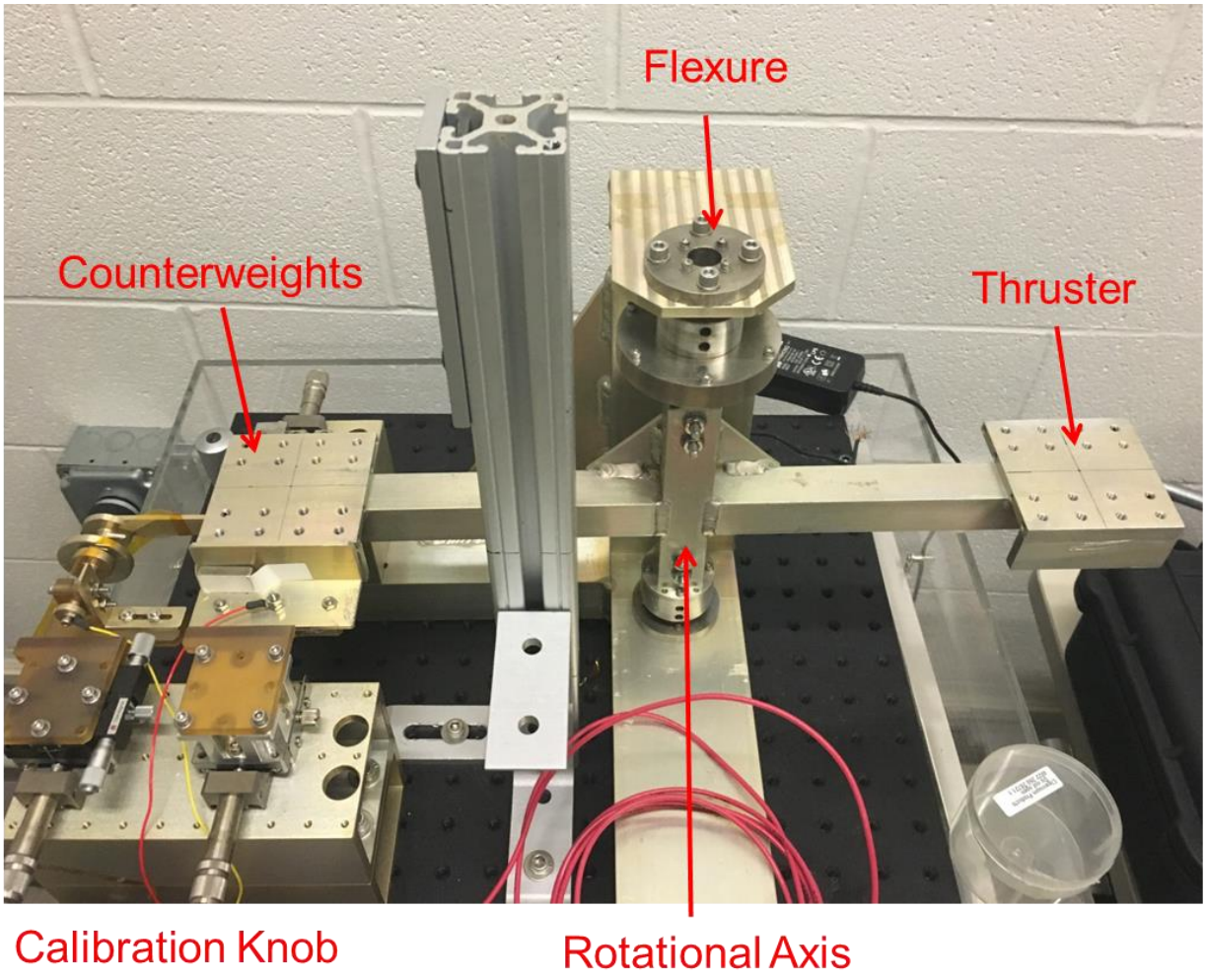

Figure 20. Torsional balance system, created by Busek, Co. Inc. This image shows the location of the thruster, the counterweights for the thruster, the rotational axis, the flexure used to find the relationship between the output voltage and the thrust, and the calibration knob used to achieve accurate results from the stand.

The thrust stand has two mounts on the end of each of its arms, one for the thruster and one for a counterweight to ensure that the system is level—a requirement for accurate operation. As is labeled in the above figure, the rotational axis is in the middle of the picture, and it is the vertical point about which the system rotates. On the top of the rotational axis is the flexure, which is the spring that allows one to solve the differential equation that relates thrust to the voltage output of the thrust stand. Finally, on the left of

the picture is the calibration knob, allowing the user to adjust operation of the stand to ensure accurate measurements based on a prescribed process from the manufacturer.

For an example case of a 1 mm separation between the detector plates, Busek, Co. Inc. provided a chart containing conversion information from voltage output by the thrust stand to actual thrust. This table was converted into a chart, and is shown below in Figure 21.

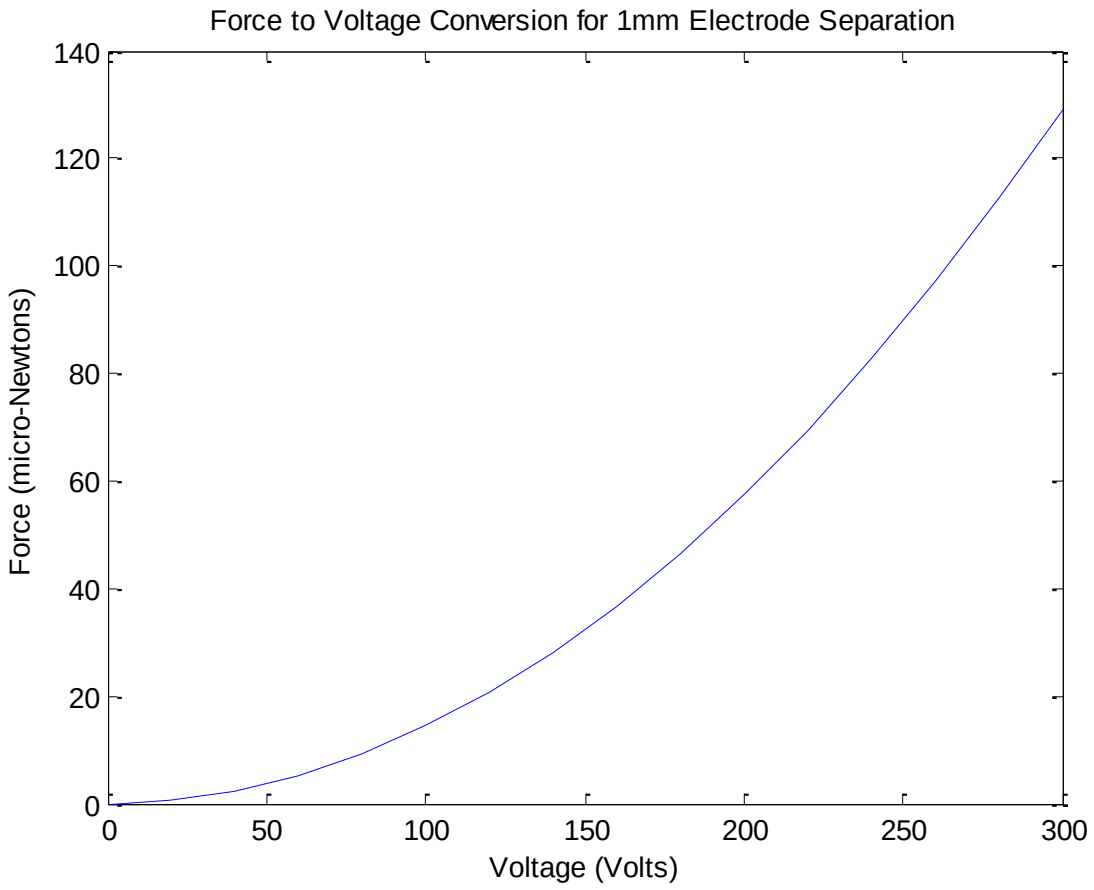

Figure 21. Manufacturer-provided data on the relationship between the voltage output by the thrust stand and the corresponding thrust from the ion engine for a case with 1 mm plate separation [17].

In the event that the torsional balance system is not run with a 1 mm plate separation, the manufacturer also provided an equation, solved from the differential

equation with the information from the flexure, relating the thrust stand output voltage to thrust produced [17]:

$$F = \frac{(1.262 * 10^{-9})(1 + 138.1 * d)V^2}{d^2} \quad (40)$$

Equation 40 relates the force to the voltage for a given distance between detector plates. F is the force, V is the voltage, and d is the distance between the plates on the thrust stand. Therefore, with a steady state firing, a relatively constant voltage should be output by the torsional balance system. With this information, it is possible to find a steady state thrust from the 1 cm ion engine.

3.10 Ion Engine and Neutralizer Cathode Setup

Since the experimental setup for all the components outside the vacuum chamber has been outlined, the next step is to show the installation of the thruster system inside the chamber. In Figure 22, below, the thruster and neutralizer cathode are mounted inside the vacuum chamber, with the various connections, such as gas flow, an SMA cable for RF plasma generation, and screen and accelerator power lines detached from their respective connectors.

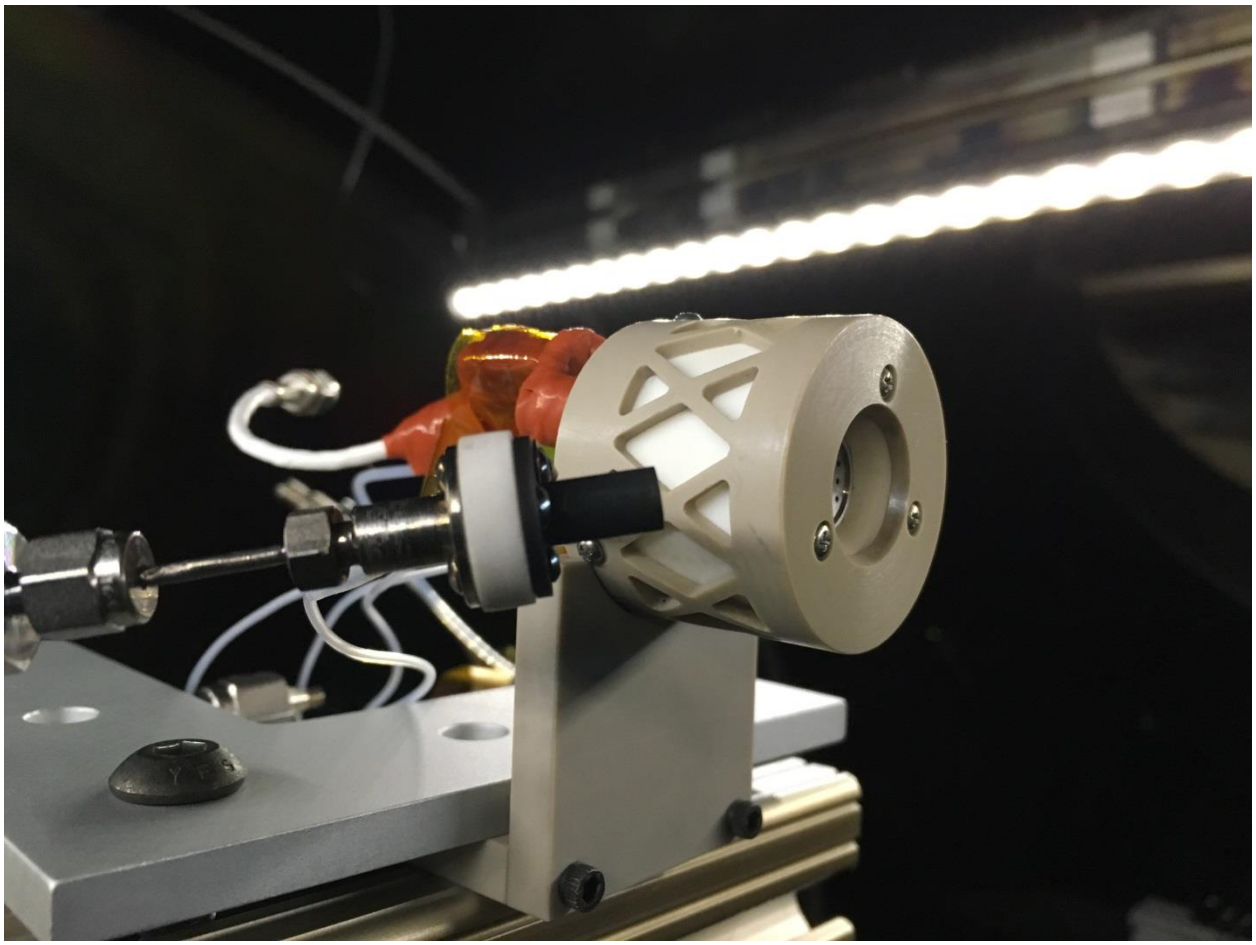

Figure 22. The ion engine and neutralizer cathode mounted inside the vacuum chamber. The connections to the exterior of the chamber from the thruster and cathode are not attached in this image.

In Figure 23, below, the face of the thruster and the neutralizer cathode are shown, along with some of the mounting structures used to secure the system. Additionally, some of the visible wiring and connections are labeled.

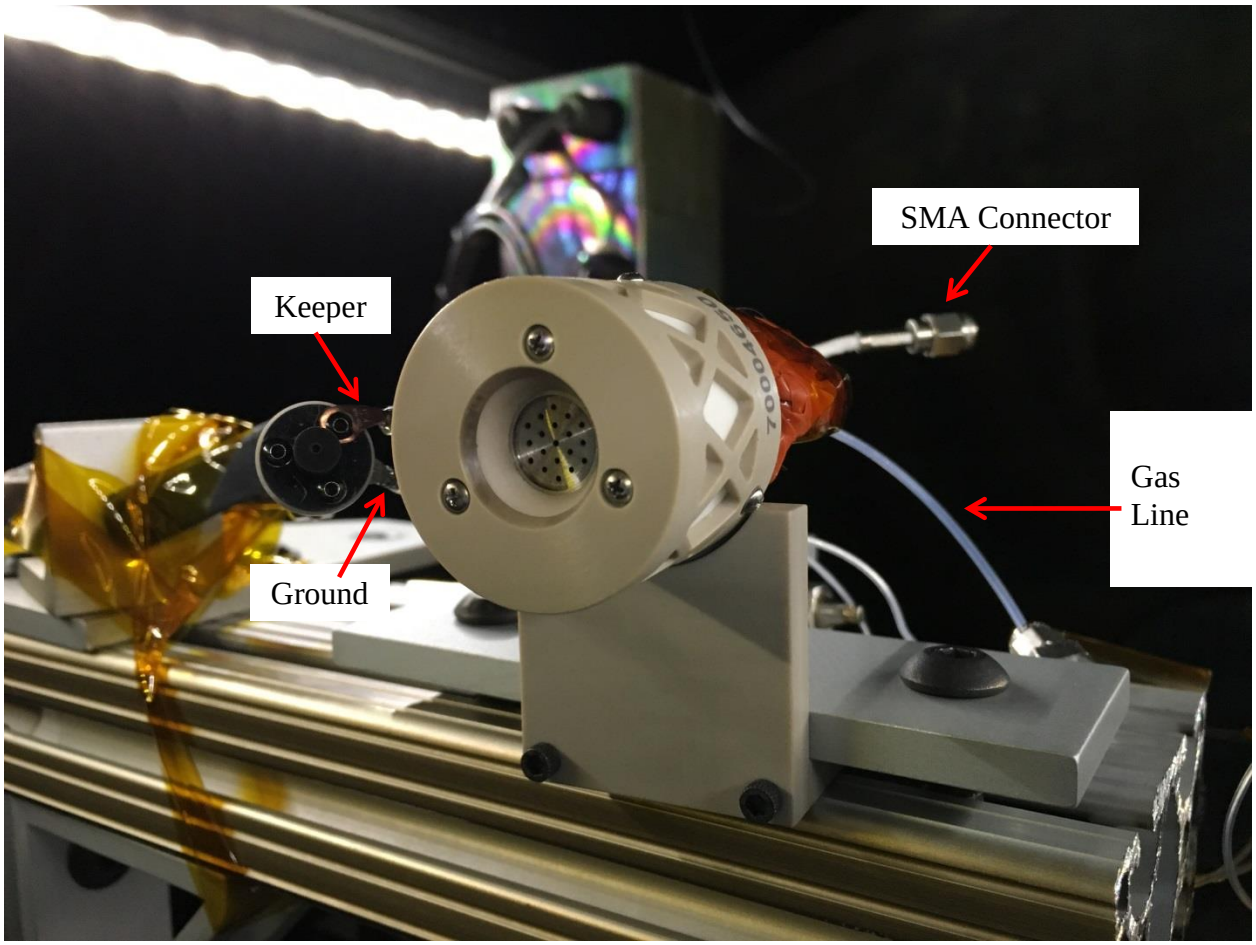

Figure 23. View of the face of the ion engine and the neutralizer cathode, along with various connections.

In the following image, Figure 24, the opposing view of the ion engine and neutralizer cathode is shown. Near the top of the picture, in the background of the image, is the stage where the Faraday probe is mounted. Note that it has the two translational stages that allow it to move in an arc. The rotational axis of the stage is not visible.

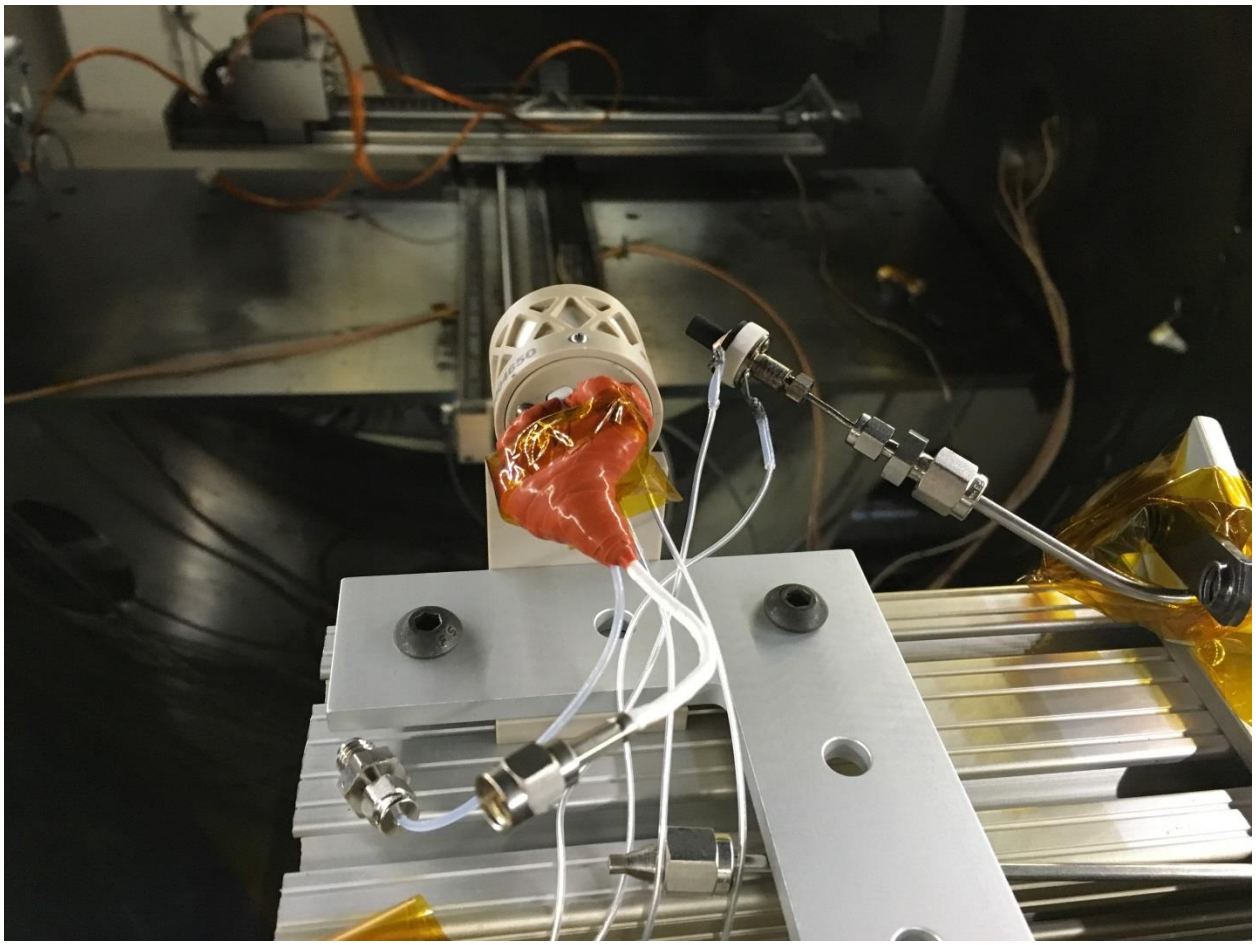

Figure 24. View of the back side of the ion engine and the neutralizer cathode mounted in the vacuum chamber. In the background of the picture is the two axis translational stage where the Faraday probe is mounted.

To conclude the setup portion inside the chamber, a final image, Figure 25, is shown below. In the figure, all the connections and wires are label to show their connections outside the chamber.

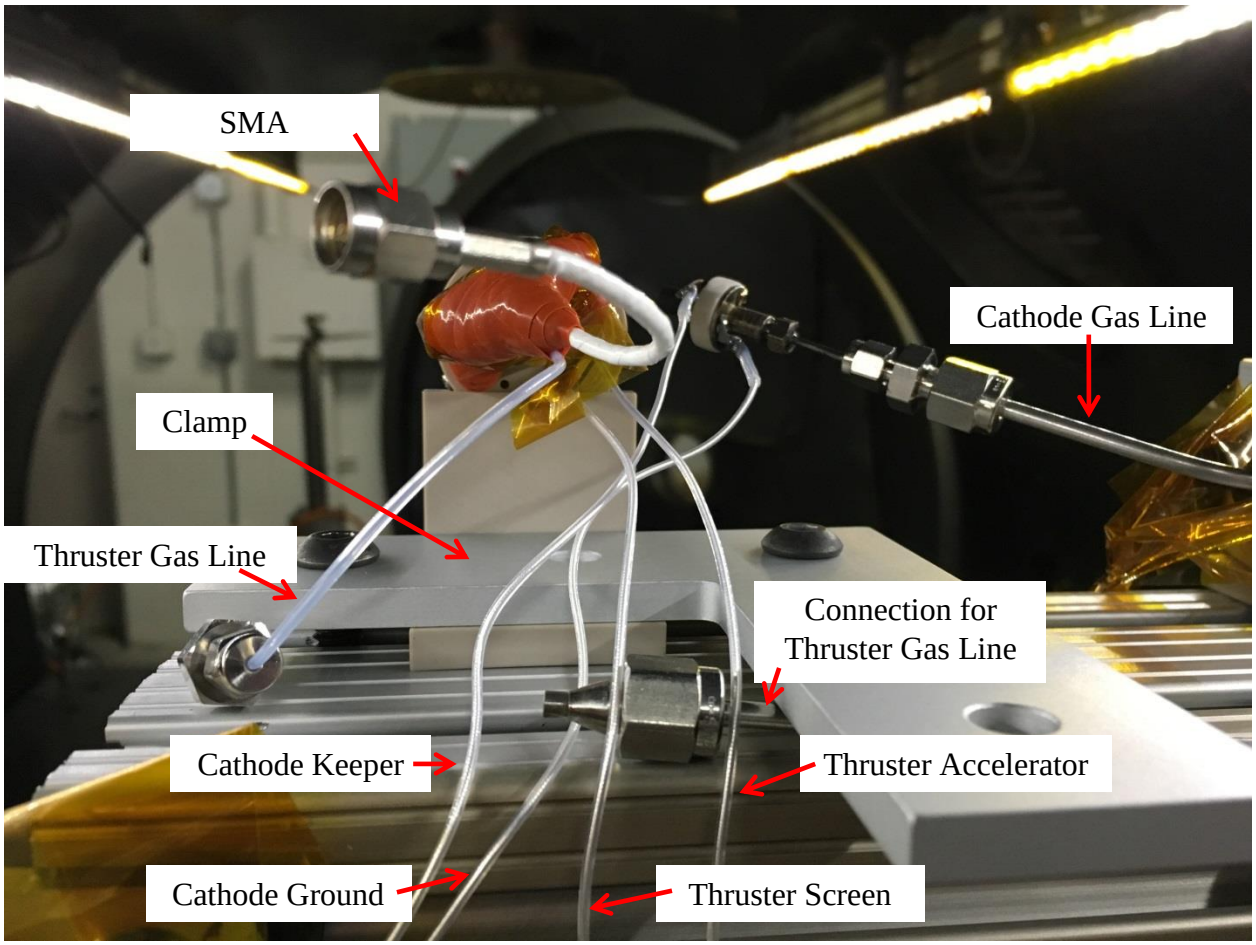

Figure 25. Back view of the ion engine and neutralizer cathode, with all connections labeled.

Finally, to show the size of the 1 cm ion engine and its neutralizer cathode, Figure 26**,** is presented below. In the image, the neutralizer cathode is on the left, the thruster on the right, and a penny is in the foreground for a size comparison.

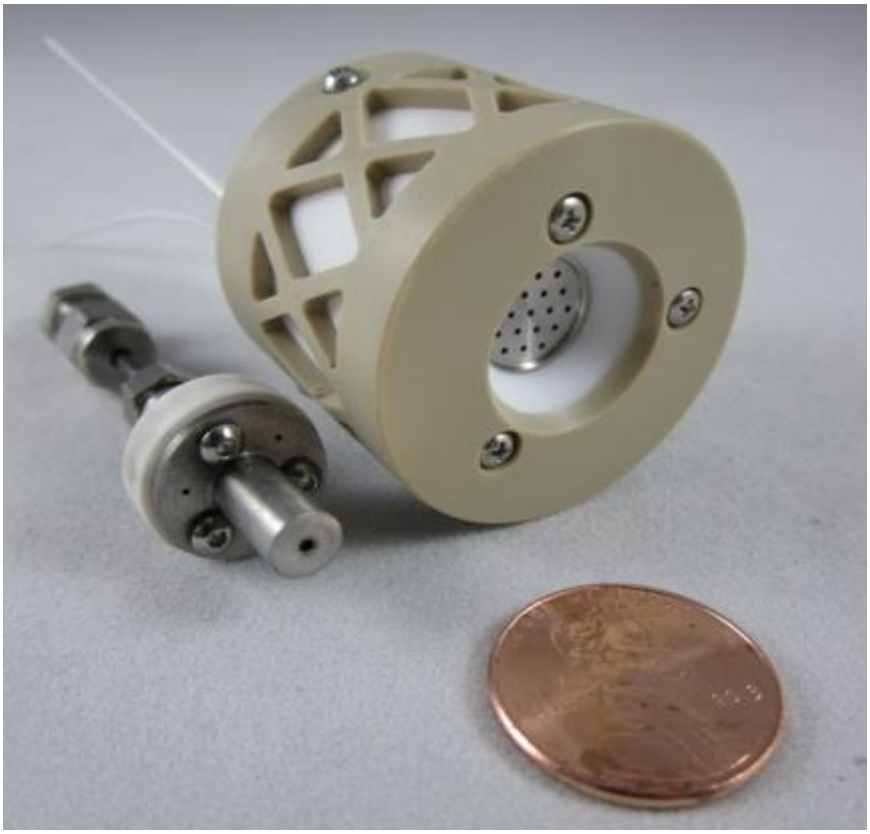

Figure 26. Image of the ion engine and neutralizer cathode prior to installation. A penny rests in the foreground for size comparison [18].

3.11 Intermediate Setup

Due to a lack of success with the original thruster setup, a secondary configuration was made to fix the problems encountered during the first wave of testing attempts. This setup was accomplished with the help of Andrew Hine, a Western Michigan University graduate student whose research involved the sister thruster to the one studied in this research, identical in size. Mr. Hine wanted to use the vacuum chamber located on the AFIT campus due to its high pumping capabilities, which allows for longer sustained firings without increasing the pressure in the chamber. With that

ability, longer firings are possible, and therefore, the diagnostics of the plume may be accomplished with more thorough and detailed results.

Prior to Mr. Hine's arrival, all attempts to fire the thruster failed due to a problem within the RF plasma generation process. The Busek RF board and associated LabVIEW program to control it had the option to run in either a manual or an automatic mode. In the automatic mode, the RF power was set, and then the program swept through a range of frequencies from 6-10 megahertz, looking for the matching frequency where the reflected power is lowest. This phenomenon normally occurs around 8.6 megahertz for this system, with a reflected power less than 10%. However, when following the start-up procedures provided by the manufacturer, the automatic mode continually swept up and down the frequencies, never settling on a matching frequency. To bypass this issue, the LabVIEW program was switched to manual mode, where one can manually change the frequencies and visually observe where the reflected power drop-off occurs. After scanning the range of frequencies numerous times, the lowest the reflected power ever reached was approximately 70%, indicating a problem somewhere in the RF plasma generation process. The thruster was unable to generate plasma with such a reflected power, and therefore, the system as a whole could not operate. The problem was likely due in part to an impedance mismatch inherent with the setup in the SPASS Laboratory vacuum chamber, so alternative methods of plasma generation through RF excitation and other potential setups were examined.

Mr. Hine had operated his thruster by bypassing the Busek equipment that was the root of the issue in the setup at AFIT. As opposed to the RF board and LabVIEW program to run the RF excitation, Mr. Hine used a series of instruments to identify the

matching frequency with the lowest reflected power and generate a signal at the proper frequency. He used an HP 8935 CDMA spectrum analyzer in conjunction with a Mini Circuits ZFBDC20-61HP-S+ bi-directional coupler and a Mini Circuits ZX47-40-S+ power detector to find the frequency with the lowest reflected power in the system. Then, using a Tektronix AFG2021 function generator linked to an ENI 603L RF amplifier, Mr. Hine input a signal with the determined frequency of 8.75 megahertz into the thruster through an SMA connection. With this setup, the need for the RF board and LabVIEW was eliminated. Therefore, Mr. Hine integrated his RF excitation instrumentation into the experimental setup in the vacuum chamber in the SPASS Laboratory, theoretically bypassing the ineffective components. All other setup wiring and tubing for the thruster and neutralizer cathode remained the same as in the original configuration, with the exception of the addition of a rotational stage. The thruster and neutralizer cathode, attached to the rotational stage, is shown below, in Figure 27.

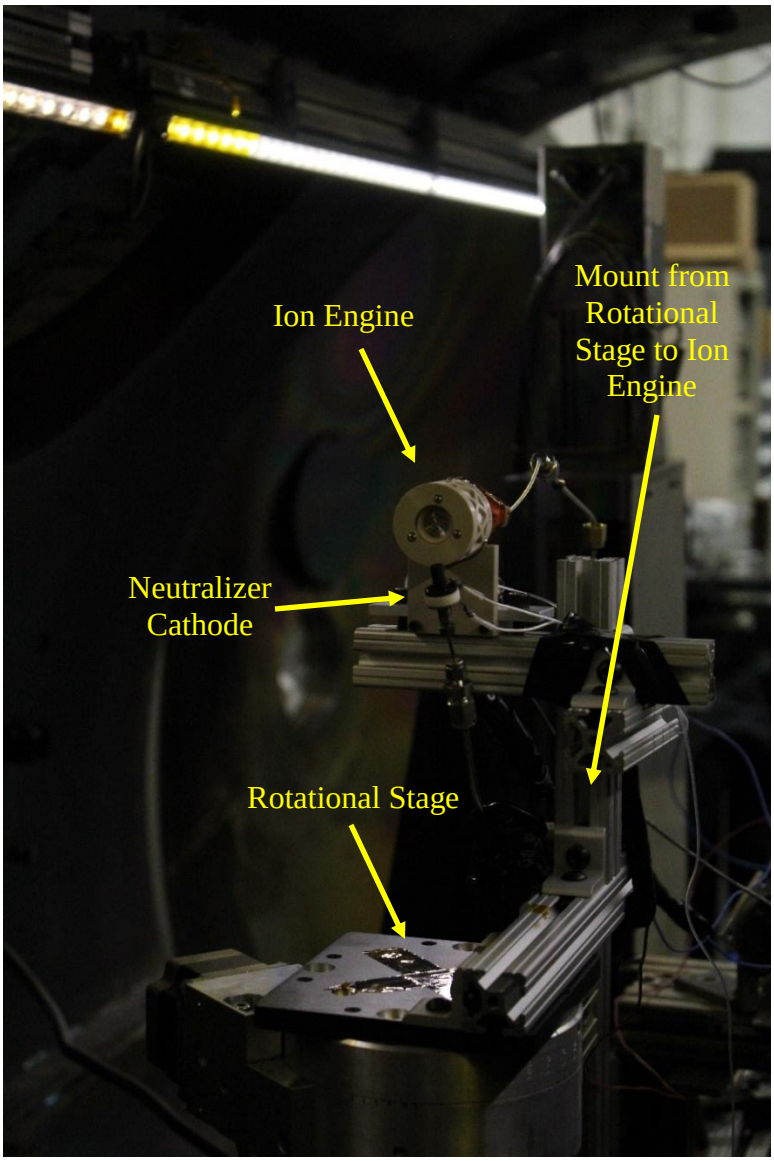

Figure 27. Ion engine and neutralizer cathode mounted to rotational stage.

For Mr. Hine's research, information from various probes for numerous thruster angles was required. To start, the setup used a Faraday probe. In place of the Plasma Controls Faraday probe used in the original setup, Mr. Hine brought an Air Force Research Labs (AFRL) designed probe from his laboratory. Instead of a single point aperture, this nested probe utilized a pair of circular collectors, but still indicates the same

beam current density information. Mr. Hine needed current density information from the Faraday probe starting from 90 degrees off the face of the thruster, so the probe is situated perpendicular to the thruster's thrust vector. This capability is demonstrated in Figure 28, below.

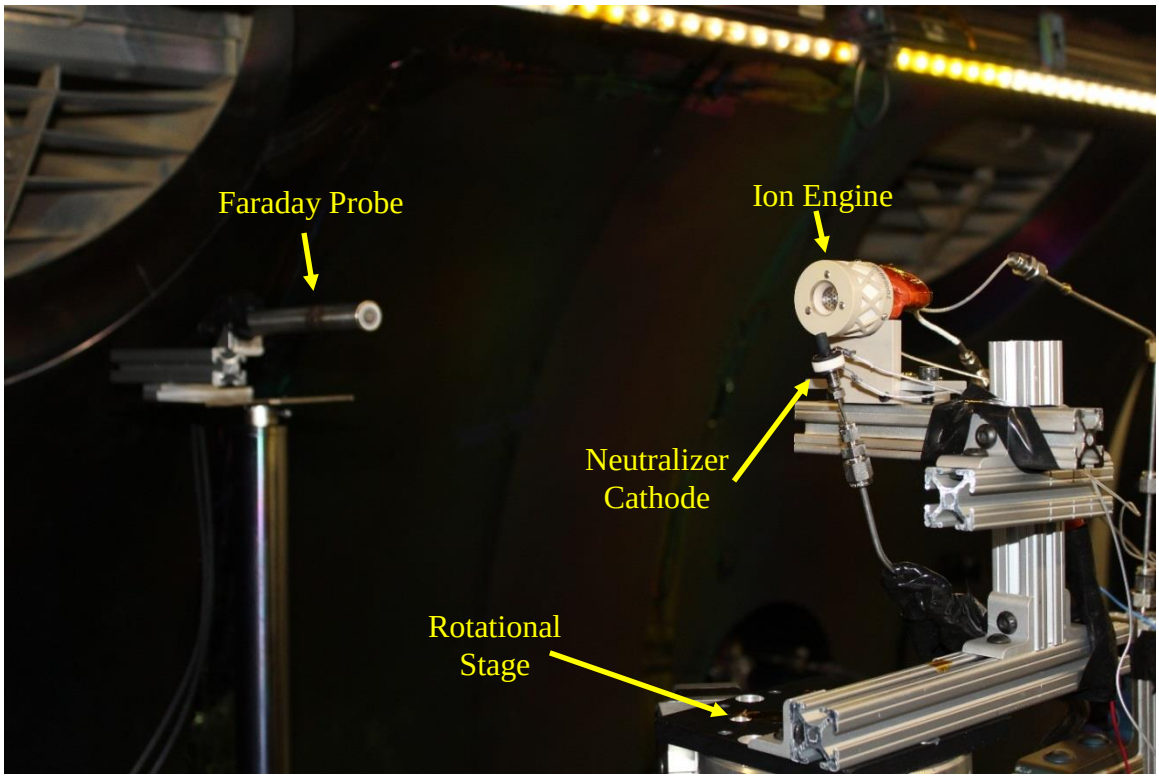

Figure 28. The ion engine and neutralizer cathode mounted to a rotational stage with the ARFL Faraday probe mounted 90 degrees off the face of the thruster.

From there, using the Plasma Controls translational and rotational stage, the AFRL Faraday probe can sweep through to the centerline of the thruster for numerous different radial distances from the face of the thruster. Next, the same process is to be repeated with differing thruster angles, varying by plus or minus 2.5 and 5 degrees. This is accomplished using a B4800 rotary stage, which is capable of multiple axis rotation, but only one was needed for this research. The rotational stage is powered by a PK264-

03A-P1 motor. An image of the final setup, with the rest of the vacuum chamber included, is shown in Figure 29, below.

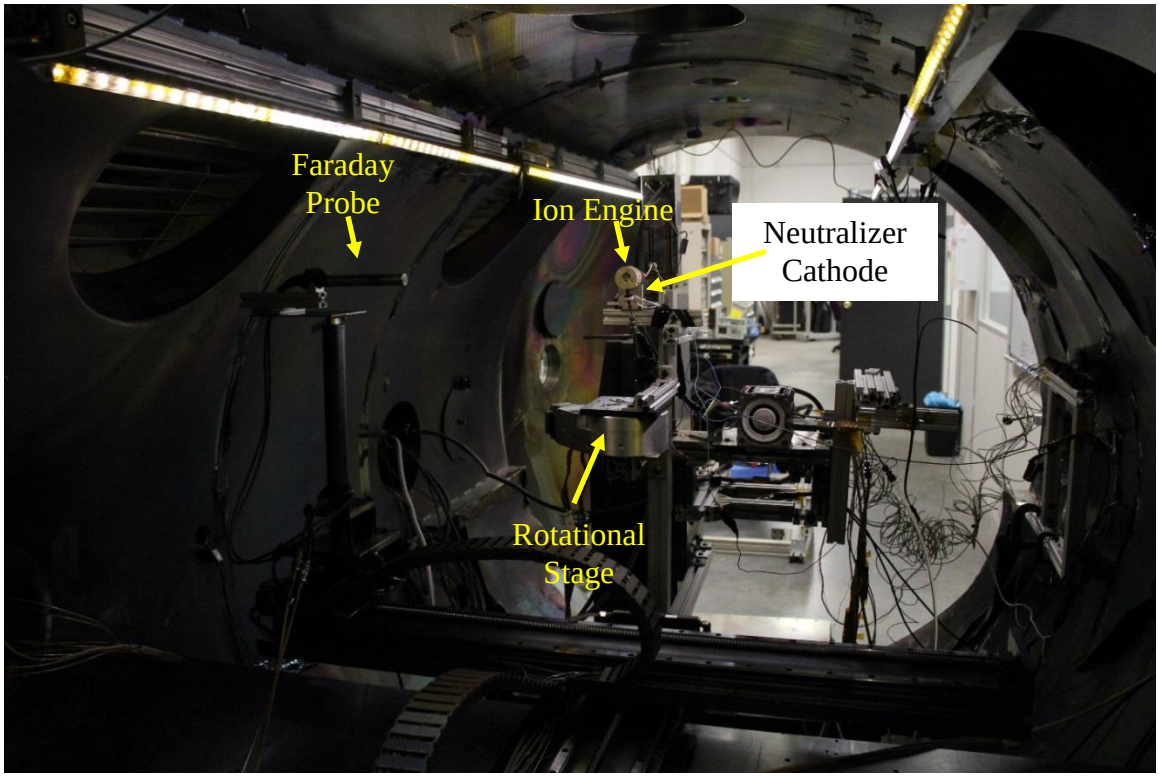

Figure 29. The final setup used in the SPASS chamber with the Faraday probe, ion engine, neutralizer cathode, and rotational stage.

The setup depicted in Figure 29 was, unfortunately, not successful. Initially, during the phase where the vacuum chamber reduces the pressure in the chamber, there were issues with the inability to reach pressures of 10^{-7} torr, which is the normal pressure for the vacuum chamber. After numerous tests and unsuccessful attempts to reduce the pressure by ensuring tight seals, it was discovered that a recently installed 10" cable feedthrough had a faulty component that essentially left a hole with about a millimeter diameter in the chamber, which explains the lack of low pressure. The feedthrough was determined to be the sole source of the problem with the chamber, as regular vacuum pressures were obtained once the feedthrough was replaced.

As the thruster cannot fire in pressures above approximately 10^{-4} torr, there was a halt on testing until the vacuum chamber was fixed. Once it was fully operational, attempts to fire the thruster and collect data with the Faraday probe resumed. Testing plans were drawn out for the Faraday probe stage and an Excel document was created to relate the real-life x, y, and theta values of the probe with the values necessary to input into the computer to achieve them. Though the Faraday probe stage has autonomous capabilities, the use of a separate Faraday probe and computer system than what the stage was designed for dictated that the probe be moved manually. With manual motion, one can correlate the data from the probe to the position the probe rests, which are sets of information located on two separate computers. Therefore, a plan was drawn out to move the Faraday probe to hundreds of different locations to collect current density information, and the corresponding theta values needed to point the probe at the thruster were calculated. All the tests were ready for when the thruster had a sustained firing.

With the chamber at the proper pressure and everything else set up, the startup procedures were the next step. With some coaxing and a little bit of time, the electride neutralizer cathode began emitting electrons and ran smoothly, without sputtering. From there, the thruster is supposed to turn on using the seed electrons from the neutralizer cathode. To do this, the polarity of the accelerator grid is momentarily flipped from negative 200 volts to positive 200 using a toggle switch. Normally, with the RF plasma generation system already in place, the toggle switch is the only action necessary to start the thruster. Despite hundreds of attempts, the thruster never ignited.

One cause of the lack of ignition was likely the use of two flow controllers in series. In the SPASS Laboratory, there are four flow controllers already installed in the

chamber, which were previously discussed. However, those do not have the precision necessary to reach the .05 SCCM necessary for the ion engine to work properly. Therefore, a second, more precise flow controller was installed in series with another flow controller to further regulate the flow into the chamber. This change required significant Swagelok alterations, but allowed the plumbing already installed into the chamber to stand. During the attempted startup of the thruster, the first flow controller went to its defined value, normally 10% of the 10 SCCM flow, without issue. However, as time wore on, the flow controller would eventually drop down to minimal flow.

At first, it was not understood why such a change was happening, so numerous workarounds were attempted, such as letting the flow controllers cool and regulating their temperature with a fan, and using different wires to control the same flow controller with a different regulator. However, none of these attempts were successful at preventing the first mass flow controller in the series from eventually dropping off flow. It was determined afterwards that the likely cause of the flow controller's strange behavior is that the second flow controller only allowed approximately 8% of the 1 SCCM flow coming from the first controller into the chamber. Therefore, the majority of the flow remained stuck in the line between the two flow controllers. As the first flow controller continued to send more xenon into the line, eventually the line completely filled up and the first flow controller was no longer able to send its specified mass flow through to the second flow controller. Because of the regulator of the first mass flow controller outputting seemingly incorrect numbers and the fact that the thruster would not start, it was assumed that the mass flow, or lack thereof, was the root of the cause of the problems.

Once the likely root of the problem was determined, Mr. Hine had used nearly all his time available to stay at AFIT, and decided that it was best to pack up his things. While venting the vacuum chamber, all of the gear outside the chamber was removed. Once the chamber was at atmospheric pressure, disassembly of the components inside the chamber began. Most went smoothly until the removal of the ion engine itself. During its disassembly, the SMA connecter that attaches to the wires leading to the coils on the thruster used for RF plasma generator fell off. It was not yanked, meaning that the connector must have been loose from a previous time. Due to the fact that the thruster did not fire originally because of RF issues, namely much too high of a reflected power, the SMA connector is likely the cause, or at least a contributor to the issues with the thruster. With these issues in mind, the last tests at AFIT concluded, and the final attempt at testing could begin.

3.12 Final Setup

The final experimental setup for this research occurred at the site of the manufacturer of the thruster, Busek Co. Inc., in Natick, Massachusetts. Though there are numerous vacuum chambers located in their lab, the one used had a two foot diameter and a three foot length, for a total volume of around 0.27 m^3. It was capable of reducing pressure from atmospheric to 10^{-6} torr in about thirty minutes and venting in about the same amount of time, which turned out to be a very useful attribute for the amount of troubleshooting and testing that could be accomplished in a short amount of time. In the SPASS Laboratory, two cycles of pumping down to vacuum and then venting to atmospheric to fix a problem would take around eight hours. In the first day of

installation and troubleshooting at Busek, the chamber was cycled six times to fix problems. The ability to decrease and increase pressure so quickly corresponded to finishing about a week's worth of troubleshooting at AFIT to a single day at Busek.

The setup at Busek used the same Omega FMA-2601 flow controller used in the setup at AFIT for the thruster, but it did not have to be attached in series with another flow controller. For the neutralizer cathode, the flow controller was regulated by an MKS type 247, also identical to the one in the SPASS Laboratory. The flow controller for the cathode was a MKS 1179A11CR1BV, capable of 10 SCCM, which is the maximum flow rate required to start the neutralizer cathode. For the RF plasma generation process, the RF board was once again bypassed, in favor of a signal generator in conjunction with a power meter. A Rohde & Schwarz SM300 signal generator was used, as the name implies, to generate a signal for the thruster at a given frequency with the lowest reflected power, and sent through an Ein RF power amplifier. To determine that frequency, an Anzac CH-130-4 bi-directional coupler was used with two Hewlett Packard 8482H power sensors to determine the forward and reflected power, which was displayed on a Hewlett Packard E4419B series power meter. By manually changing the input frequency to the thruster, the percent reflected power can be monitored and minimized, causing the most favorable condition for the start of the thruster.

Inside the vacuum chamber, the thruster and the neutralizer cathode were mounted normally, with the Plasma Controls Faraday probe opposing them. It was mounted level with the center of the thruster and initially zero degrees off its center point, as is seen in Figure 30, below.

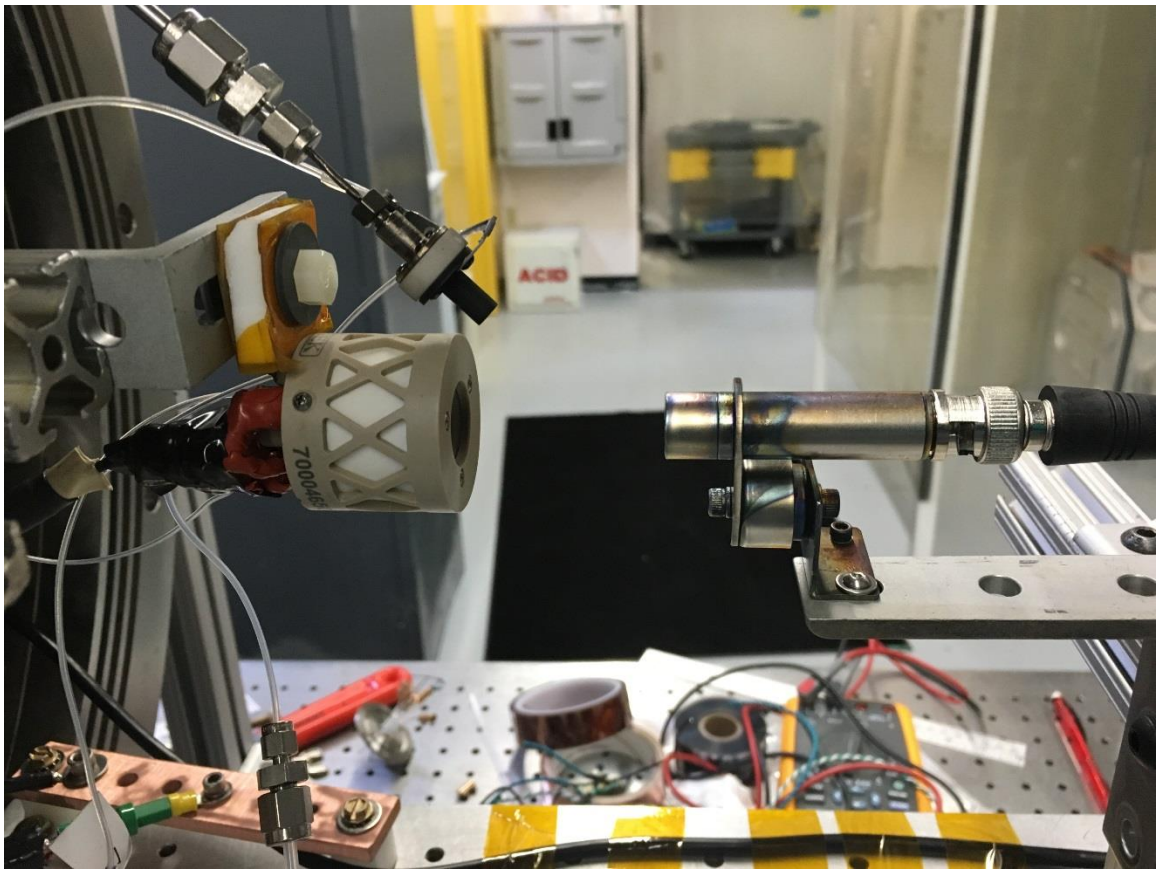

Figure 30. Setup of the ion engine, neutralizer cathode, and Faraday probe in the Busek vacuum chamber.

The probe attaches to a BNC cable, the outer portion of which is biased to -30 volts, and the inner conductor to 30 volts. This is accomplished using a LXI DP832 programmable dual-output power supply. Additionally, to calculate the current density of the plume based on the information from the probe, the voltage drop across a known resistance on the positive 30 volt side must be measured. To do this, a resistor of 3,900,000 ohms was installed in series with the positive supply, and a Fluke 287 multimeter was attached to measure the voltage drop, which was equated to a current density using an equation provided by the probe manufacturer.

To power the cathode, a Glassman High Voltage, Inc. series EQ power supply was used. It is capable of producing the initial kilovolt needed to start the neutralizer. To run the screen of the ion engine, a Glassman High Voltage, Inc. series KL power supply was installed. It can supply the 1800 volts, corresponding to the maximum the screen grid can handle. In order to get an exact measurement of the current going through the screen grid, which is approximately equal to the beam current, a Cal-Tech Co. Inc. digital multimeter was used. Finally, to power the accelerator grid, a Sorensen DCR 600-16T power supply was utilized. To accomplish the polarity switch of the accelerator grid voltage, a Busek in-house created toggle switch was installed in series with the power supply in a large, insulated box.

In order to take measurements with the Faraday probe from known distances from the thruster face in a chamber without an automated stage, the probe had to be moved manually. To do so, the chamber had to be vented between each test. The probe was mounted on a set of 80/20 supports that allowed the probe three axis freedom of movement, along with the ability to rotate, if need be. However, due to the close proximity of 4.45 centimeters between the thruster face and the Faraday probe, and the spacing of two inches between mounting holes in the Busek vacuum chamber, it was very difficult to design a system that maintained distance from the thruster in an arc motion. To sidestep this issue, the probe was moved only perpendicular to the thruster in five millimeter increments. This setup is seen in Figure 31, below.

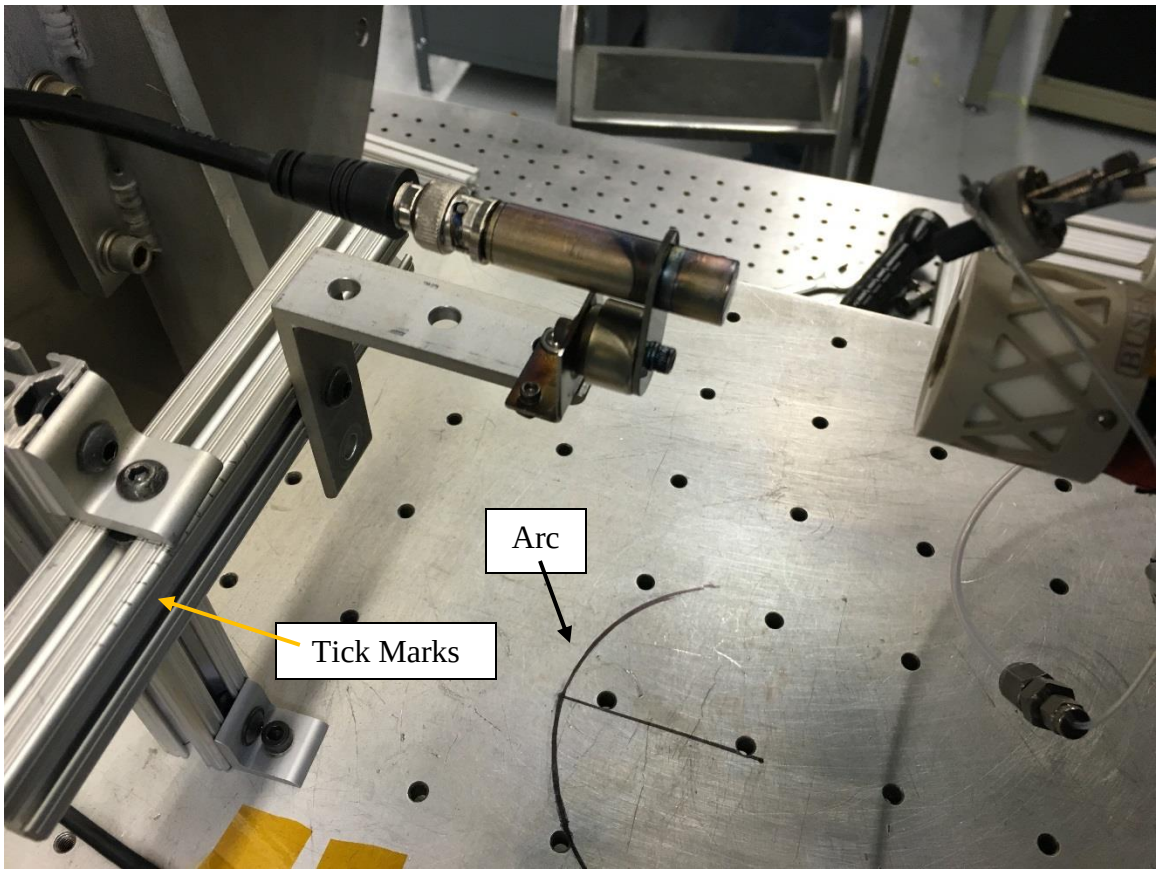

Figure 31. An image of the ion engine, neutralizer cathode, and Faraday probe, along with the two planned movement systems for the Faraday probe. On the mounting table is the arc that the probe was initially going to travel. Instead, the tick marks on the 80/20 that the probe is mounted on indicate specified five millimeter gaps, so the probe could move to known locations while only allowing one axis to move.

At each location, the screen voltage, screen current, RF forward power, RF reflected percentage power, thruster mass flow rate, probe location, and probe voltage drop across the resistor were all recorded. From there, the screen voltage was varied to determine how that impacted the thruster performance. After a full set of data was taken, the chamber was vented, the Faraday probe moved another five millimeters, the chamber pumped down, and the process repeated. Due to time constraints, and the fact that the chamber had to be cycled between each test, a full classification of the plume was not

possible because of the limited number of data points. Additionally, to save time, and therefore obtain more data points, the Faraday probe always remained parallel to the centerline of the thruster, rather than angling to point directly at the thruster, which would have required extensive probe work with each chamber cycle. This strategy allowed for more data points to be taken at the cost of some of the beam current density, which is corrected for in the results and analysis portion of this paper. An image of the final setup and probe movement strategy, with the tick marks, is seen in Figure 32, below.

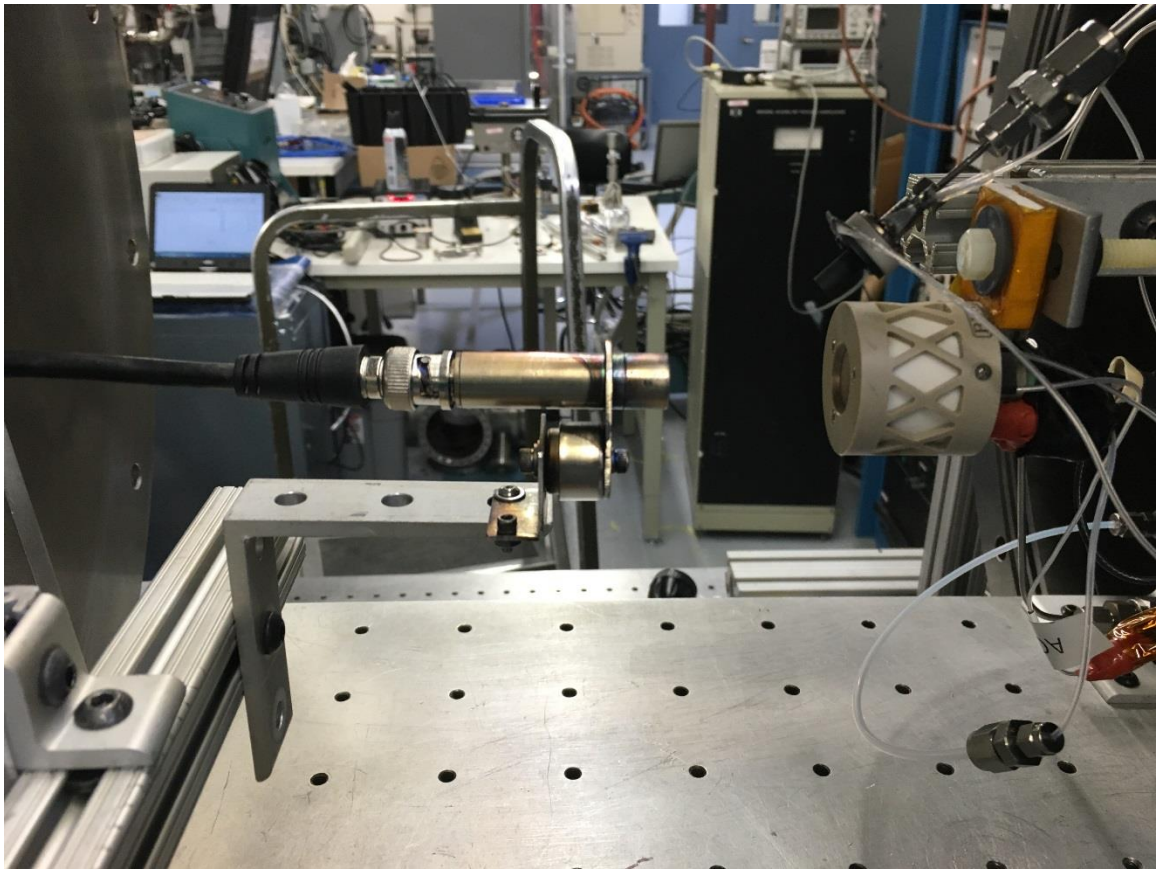

Figure 32. The final setup of the ion engine, neutralizer cathode, and Faraday probe, with the tick marks visible on the bottom left corner of the image on the 80/20 supports.

IV. Analysis and Results

4.1 Chapter Overview

The purpose of this chapter is to discuss the results of the experimentation and expand on the analysis of the results. Due to testing complications at the Air Force Institute of Technology, all of the data and results presented in this section were recorded at Busek, Co. Inc. With the assistance of Dr. Mike Tsay and Mr. John Frongillo, and the use of Busek's vacuum chamber with a high cycle rate, the Busek 1 cm ion engine was installed and tested successfully, which is seen in Figure 33, below.

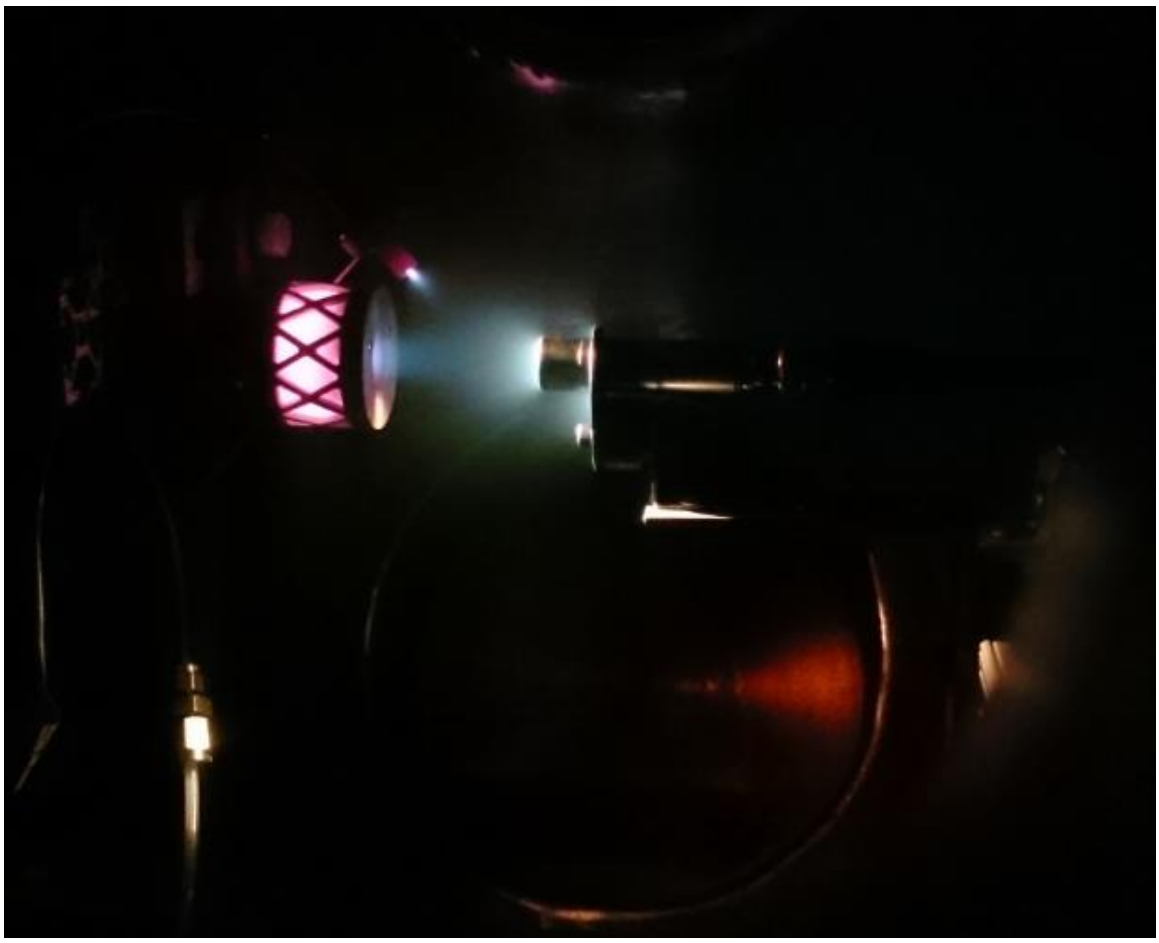

Figure 33. Long exposure image of the 1 cm ion engine and neutralizer cathode (left) emitting a beam and striking the Faraday probe (right).

4.2 Data Collection

During the testing, numerous thruster values were recorded for each data point. These included the RF forward power, percentage of reflected power, screen voltage, screen current, thruster mass flow rate, the Faraday probe voltage drop measured across a known resistance, the distance of the probe from the thruster face axially, and the distance of the probe from the thruster face radially. With this information, it was possible to calculate the RF load power, using Equation 41, where all units are watts.

$$RF\ Load = (RF\ Fwrd\ Pwr)(1 - \%\ Reflected\ Pwr) \quad (41)$$

The RF load is the power the thruster actually sees, in watts, the RF Fwrd Pwr is the power, in watts, supplied to the system, and the reflected power is a loss in the system. Therefore, when accomplishing total power calculations for the thruster and plotting, the RF load value is used, as opposed to the input power, the RF forward power. For efficiency calculations, the total power is needed. Next, it was possible to estimate thrust within about five percent accuracy using known relations with ion engines with a xenon propellant, shown below.

$$T = I_{beam}\sqrt{\frac{2V_{screen}m_i}{e}} \quad (42)$$

T is in Newtons, I_{beam} is in amperes, V_{screen} is in volts, m_i is in kilograms, and e is in Joules. The beam current is equal to the screen current minus the accelerator current. It is approximately equal to the screen current due to the fact that the accelerator current is fractions of a milliamp. The screen voltage was measured, so that value is known. The mass term is calculated using the molecular weight of xenon, 131.3 grams per mole,

converting to kilograms, and dividing by Avogadro's Number, $6.022 \cdot 10^{23}$. The e term is the elementary charge, $1.6 \cdot 10^{-19}$ coulombs.

Because an estimate of the thrust for each test point is now known, one can calculate the specific impulse. However, mass flow rate for the thruster was recorded in SCCM, and it was necessary to convert that number to kilograms per second, using the fact one SCCM of xenon is $9.747 \cdot 10^{-8}$ kg/s. Once all terms are in the correct SI units, Equation 43 is used to calculate specific impulse with units of seconds.

$$I_{sp} = \frac{T}{\dot{m} g_0} \tag{43}$$

From there, the information from the Faraday probe is used to calculate the current density. The Faraday probe has an exterior shell biased to -30 volts, and an inner conductor biased to 30 volts. This setup ensures electrons cannot hit the collector plate, due to the negative exterior bias, and low energy positive ions, such as the products of charge exchange, cannot hit the collector plate due to the positive interior bias. Therefore, only the high energy, positive ions hit the collector plate. To measure the voltage output from the Faraday probe, a 3.9 mega-ohm resistor was placed in series with the positive potential. Then, knowing the aperture radius on the probe is 0.0381 cm, corresponding to an area of 0.00124 cm^2, the current density sensed by the probe is calculated using Equation 44 [16].

$$j_{beam} = \frac{V \cdot 1000}{R \cdot A_{aperture}} \tag{44}$$

Where j_{beam} is in mA/cm^2, V is the measured voltage drop across the resistor in volts, R is the resistance in ohms, and $A_{aperture}$ is the probe aperture area in square centimeters.

Additionally, the probe's angle from the thruster centerline and total distance from the thruster is calculated using geometry.

For the initial testing, the Faraday probe was located on the centerline of the thruster, 4.45 centimeters away from the face. At the initial center point, 10 test cases were conducted, varying the mass flow rate to the thruster, screen voltage, and RF forward power. Afterwards, the tests were simplified to vary only the screen voltage at different locations. The change was made for a few reasons. First, it was discovered varying the mass flow did not yield predictable results. This occurred because of the accuracy capabilities of the thruster's flow controller. It is rated to have a 1% error for 0.5 SCCM. When operating in the thruster's required regime near 0.05 SCCM, that 1% turns into 10%. During testing, flow was varied from 0.04 to 0.06 SCCM. With the 10% error, it was quite possible the flow rate when set to 0.05 SCCM was actually greater than the one at 0.06 SCCM. Therefore, all the mass flow rates were kept constant after the initial point in an attempt to preserve recognizable trends in the data. Additionally, altering the RF power at the initial point yielded all the data necessary for the impacts of power changes to the thruster. As the screen voltage is varied, the power is also varied due to the relatively constant screen current. Therefore, adjusting both the RF power and the screen voltage is essentially adjusting the same parameter two times. For these reasons, testing was limited to a screen voltage of 1600, 1700, and 1800 volts at each Faraday probe location beyond the center point.

Excluding the data retrieved from the mass flow alterations, which were not verified as accurate, all the data was used to create charts of thrust versus total power and specific impulse versus total power. Total power, in this case, is the RF load power plus

the beam current times the screen voltage. The 1 cm ion engine is classified as a 10 watt thruster, and it is noticeable the majority of the data points occur around this region in Figure 34 and Figure 35.

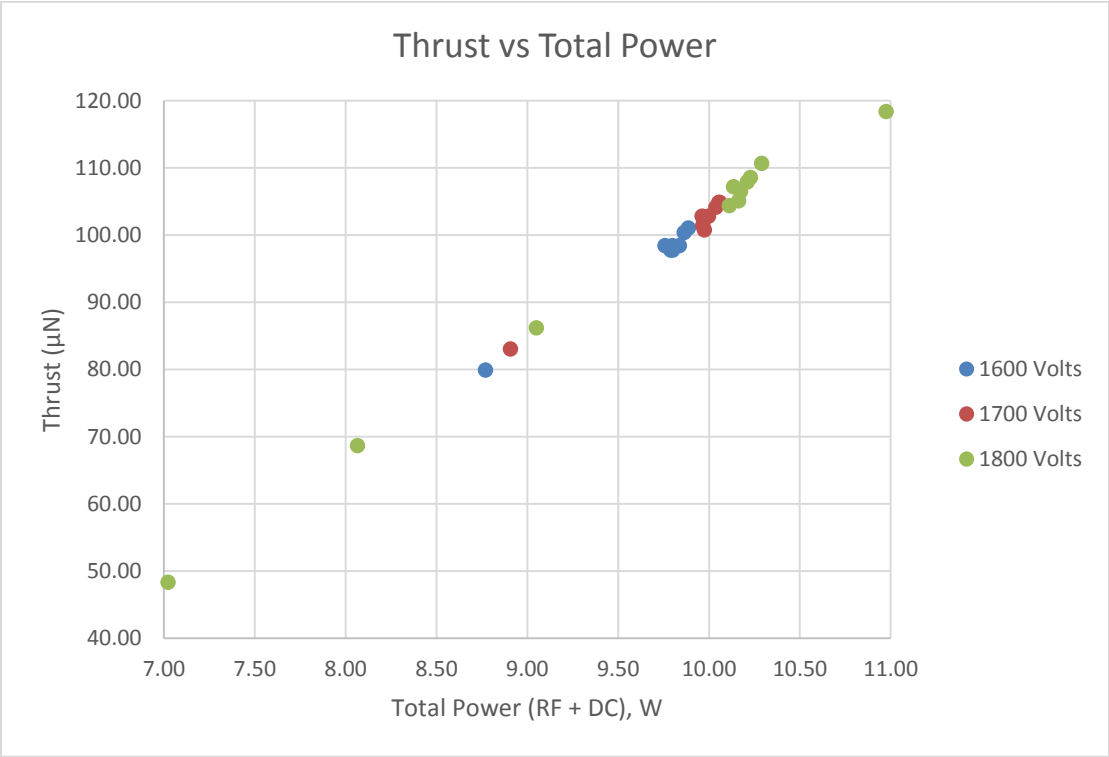

Figure 34. Thrust versus total power for screen voltages of 1600, 1700, and 1800 volts.

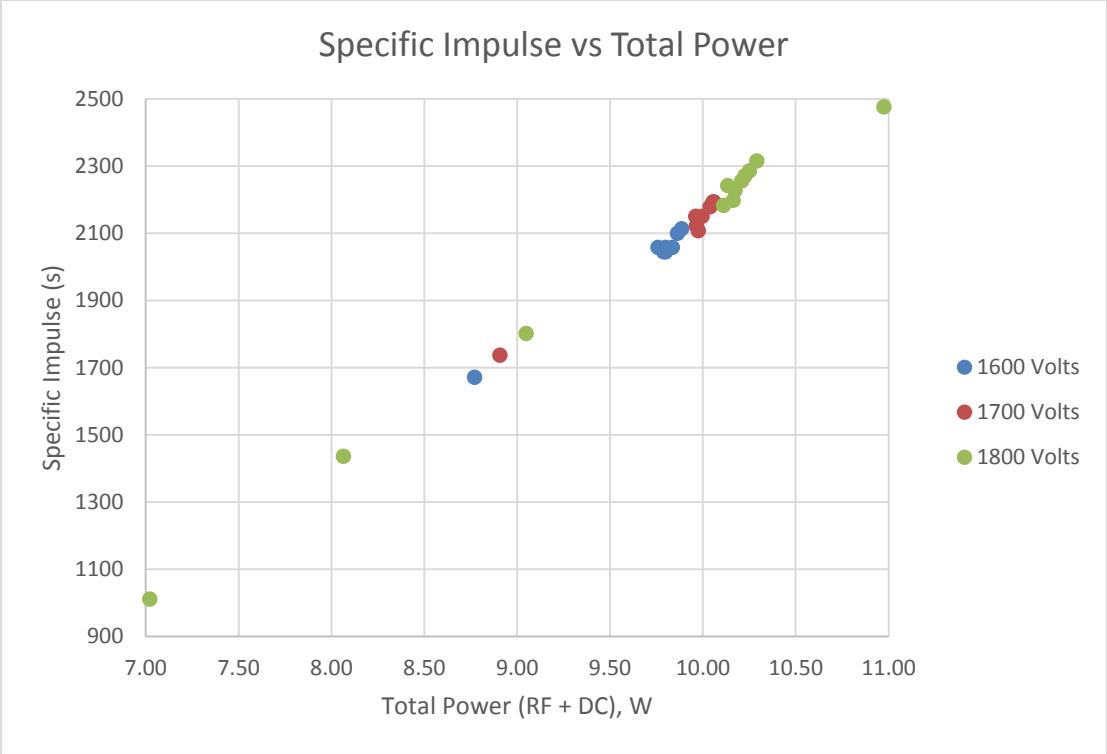

Figure 35. Specific Impulse versus total power for screen voltages of 1600, 1700, and 1800 volts.

The linear trend in both of these graphs is clearly visible, independent of the varying screen voltages. This is because, as previously mentioned, the alteration of the screen voltage impacts the total power. Ion engines' performance is directly linked to the power supplied. As the power increases, so do the thrust and specific impulse capabilities of the thruster. As these charts indicate, this trend remains true for micro ion engines as well. In the interest of preserving the thruster's ability to operate, it was not run at the advertised maximum power. The highest test case was about 0.6 watts short of the maximum. The highest recorded thrust was 118 micro-Newtons, with the corresponding highest specific impulse of 2475 seconds. Using the linear trend of approximately 18 micro-Newtons per watt increase, the maximum thrust output of the thruster is 132

micro-Newtons. Similarly, a one watt increase in power yields 381 more seconds of specific impulse. Therefore, the maximum specific impulse of the thruster is around 2775 seconds. It is important to keep in mind, however, these are just the advertised values, and it is possible that actual performance of this prototype thruster is superior or inferior, depending on how much power it can handle, as the efficiency may vary with the power input. Additionally, the minimum power values tested still remained true to the linear trend, but there is a cutoff point where the thruster's performance will diminish faster at lower power levels. Eventually, after the thrust and specific impulse diminish significantly, the thruster is not able to sustain in the low power regime and will cease operation.

Using data from the Faraday probe, it was possible to plot the current density versus the number of degrees from the centerline of the thruster for the three test cases of 1600, 1700, and 1800 volts for the screen grid. Due to a limited number of test points, it was necessary to assume symmetry in the plume and only test one side. The current density variation with angle detected by the Faraday probe is shown in Figure 36.

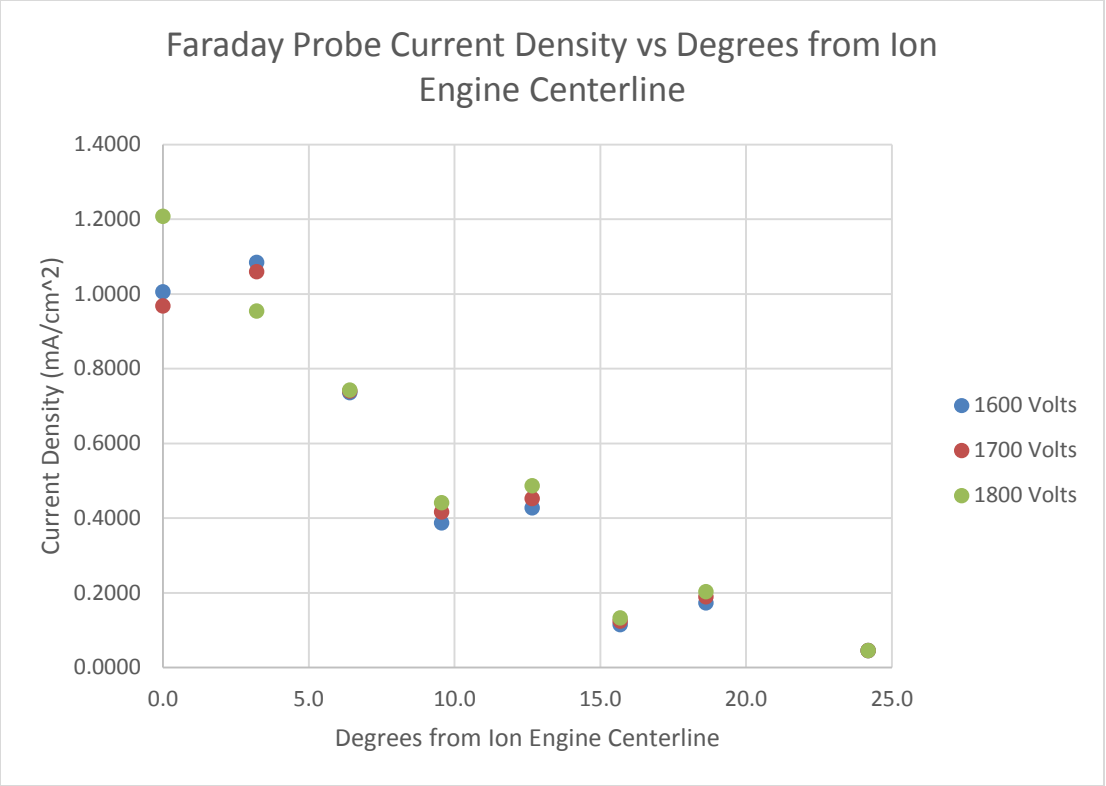

Figure 36. Faraday probe current density variation with angle from the ion engine centerline for screen voltages of 1600, 1700, and 1800 volts.

This is the raw data, all of which is found in the appendix, plotted directly from the Faraday probe measurements and its position in the vacuum chamber. The above plot does not account for any error incurred by the fact the Faraday probe faced parallel to the centerline of the thruster, rather than always pointing at the center of the thruster face. Additionally, it is noticeable the current density for the 1600 and 1700 volt cases are much lower than the 1800 case at the zero degree mark. This is because the 1800 volt case had the nominal 8.7 watts of forward RF power, whereas the 1600 and 1700 volt cases had an RF forward power of 7.89 and 7.88 watts, respectively. Unfortunately, the centerline point recorded numerous RF power values, but the 8.7 watt RF forward power chosen for the rest of the test cases was not one of them. The two data points on the chart

are lower than their correct position, and therefore, the divergence angle information from the 1800 volt case is the most trusted. After testing was completed, an attempt was made to retake the original data point to correct for the lack of information, but the neutralizer cathode was no longer operational due to the extended test firings, and data could not be obtained.

The Fluke 287 multimeter used to measure the voltage drop and calculate the current density has an error of 0.025%. Therefore, based on Equation 44, the uncertainty of the current density information is the error of the multimeter times 1000 and divided by the quantity of the resistance times the aperture area. This calculation simplifies to 0.20678 x 0.025%. With these values, the error in the current density data taken from the Faraday probe is 0.0052%, indicating the values are very accurate.

Testing with the Faraday probe occurred initially with it centered on the thruster, then moving out in five millimeter increments perpendicular to the thruster. This yielded the first five test cases, which were located at 0, 6.4, 12.7, 18.6, and 24.2 degrees. After analyzing the current density trend with the data, it was determined the divergence angle of the thruster was likely already captured. For the next tests, more precise data points were desired, so the probe was moved halfway between the earlier test points, yielding angles of 3.2, 9.6, and 15.7 degrees. A ninth test was scheduled, but the neutralizer cathode had reached the end of its lifetime, and quickly overheated whenever it was run. Therefore, the desired final data point was not accomplished.

Prior to the end of the cathode, it was exhibiting end of life characteristics, namely overheating quickly and emitting a larger beam of electrons than normal, accompanied by some sputtering. As the cathode performance deteriorated, which was

first noticed on test case 23 of the 31 total tests, Faraday probe current density information began to change. It is suspected the odd offsets, or the humps in the divergence data, occurring in the later points is due to worsening cathode performance. Without the usual steady flow of electrons, it is possible the beam from the thruster altered its geometry slightly to reach the nearest common ground, the vacuum chamber. Ideally, testing re-accomplished with a neutralizer cathode capable of longer lifetimes will provide better results, since the data is recorded across consistent conditions. Despite the two inconsistent points, the data was fit to three third order polynomial trendlines, one for voltage case. The data is shown in Figure 37.

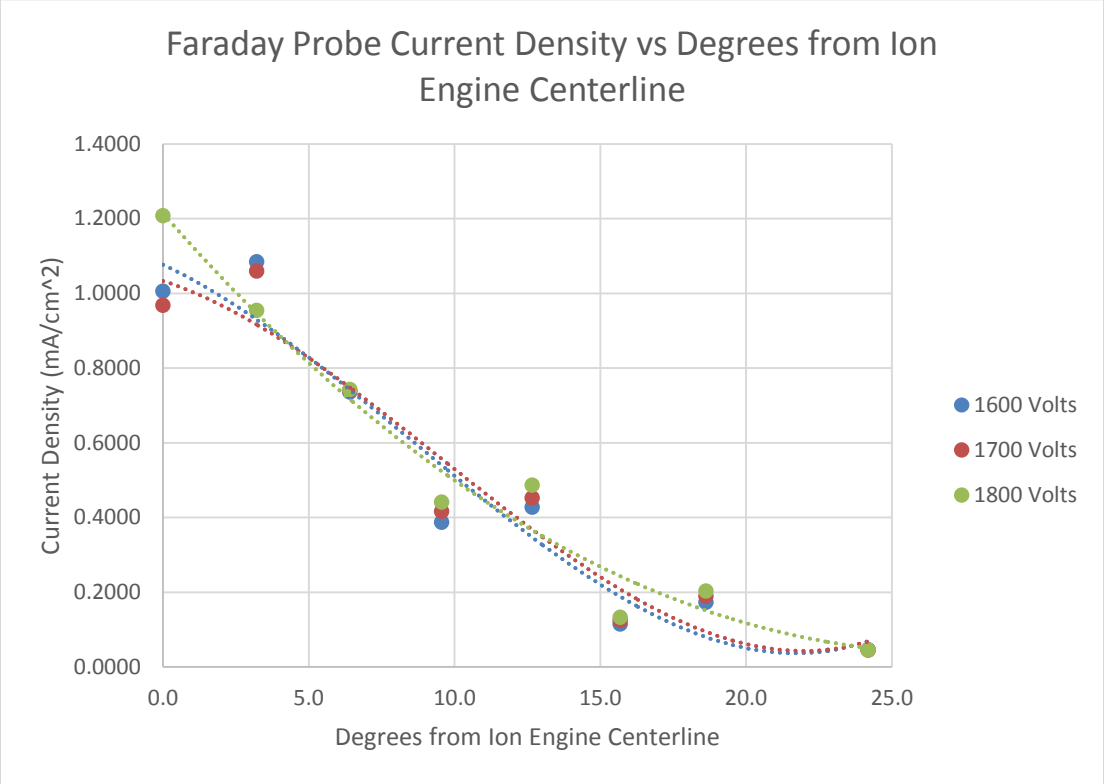

Figure 37. Faraday probe current density versus degrees from ion engine centerline with third order polynomial trendlines shown.

The equation for the 1600 volt trendline is $y = 0.0001x^3 - 0.0033x^2 - 0.0366x + 1.0766$. For the 1700 volt data, the equation of the trendline is $y = 0.0001x^3 - 0.0038x^2 - 0.0254x + 1.0328$. Finally, for the 1800 volt data, the equation is $y = -4 \cdot 10^{-6}x^3 + 0.0018x^2 - 0.0887x + 1.2133$. Using the equations for the trendlines, the current density was integrated from zero degrees to the farthest test point, 24.2 degrees. From there, the data was integrated from zero degrees towards 24.2 degrees until it had obtained 95% of the original current. The 95% divergence half angle occurs at that point, and is a commonly used definition for the divergence of an ion engine. The integration found the point where 95% of the maximum current was located for all three cases, and determined the divergence angle for a screen voltage of 1600 watts was 9.6 degrees. For 1700 watts, it was 9.5 degrees. Finally, for 1800 watts, the divergence angle of the beam was 18.6 degrees. The 18.6 degree divergence angle is the most trusted of the three due to the fact that consistent RF forward power was used throughout the testing. Due to the faulty points for the 1600 and 1700 volt cases, the trendlines for those two cases had an upward turn near its end, which interfered with the proper integration. Therefore, the calculated divergence angle of the 1 cm ion engine is 18.6 degrees with consistent data.

The divergence angle information, though useful, needs slightly more accuracy. Data presented above was taken from the probe's raw data, which does not compensate for the fact it essentially has cosine losses in detection from facing the wrong way. To correct for this, the current density information was divided by the cosine of the angle off the thruster centerline the probe sat for each individual data point. The overall impact of such a calculation boosts the current density as the probe moves farther away from the

thruster; this adjustment is necessary to account for the lack of rotation in the probe. The cosine corrected current density information is shown in Figure 38.

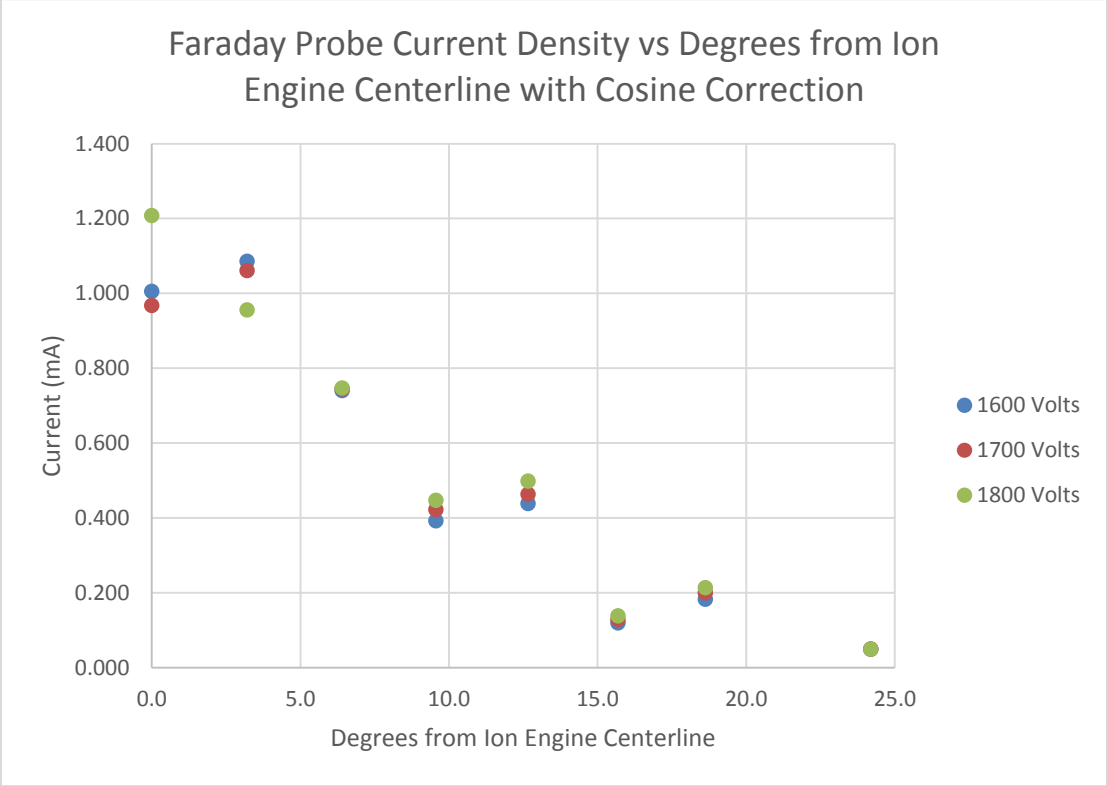

Figure 38. Faraday probe current density versus degrees from ion centerline with cosine correction for screen voltages of 1600, 1700, and 1800 volts.

Using the same method as previously described, the data was fit with three third order polynomials, the results of which are seen in Figure 39.

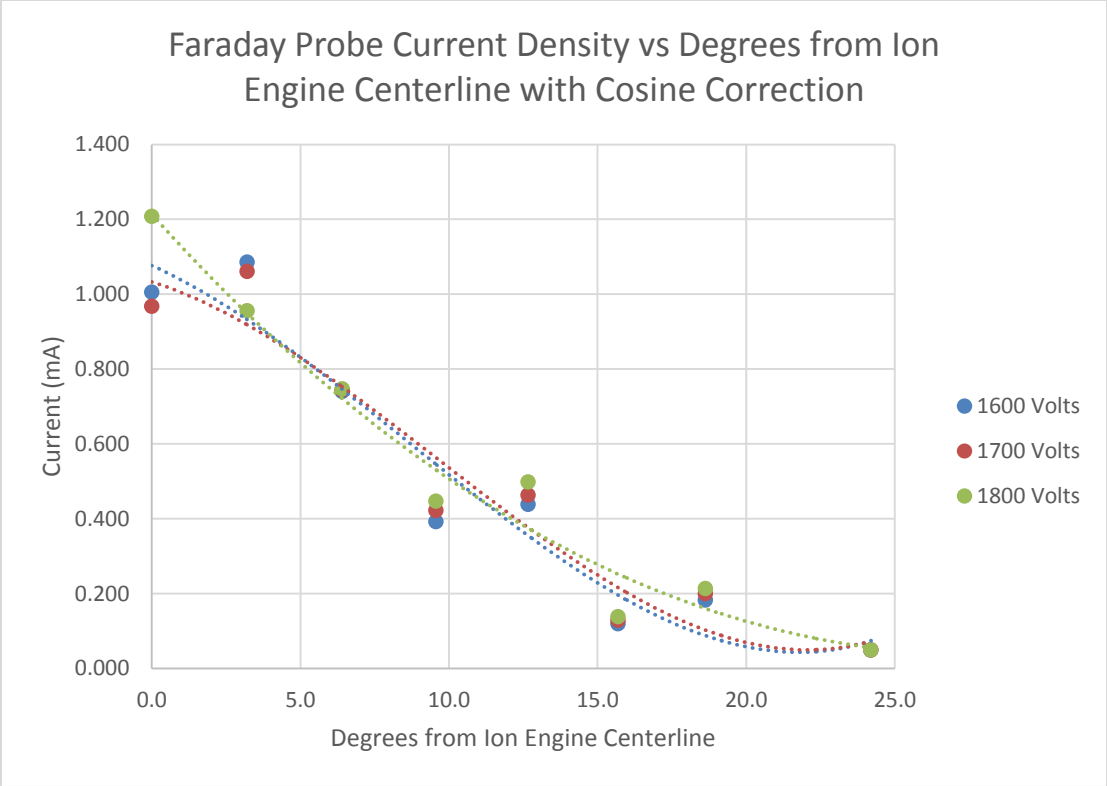

Figure 39. Faraday probe current density versus degrees from ion engine centerline with cosine correction with screen voltages of 1600, 1700, and 1800 volts.

The equation for the 1600 volt trendline is $y = 0.0001x^3 - 0.0032x^2 - 0.0359 + 1.0764$. For the 1700 volt data, the equation of the trendline is $y = 0.0001x^3 - 0.0038x^2 - 0.0257x + 1.0327$. Finally, for the 1800 volt data, the equation is $y = -6 \cdot 10^{-6}x^3 + 0.0018x^2 - 0.0881x + 1.2131$. The corrected values had very small impacts on the original trendlines, but the new equations were used for integration. Cosine correction did slightly impact the divergence angle results from the three cases. For 1600 volts, the corrected divergence angle was 10.8 degrees. For 1700 volts, it was 9.8 degrees. And for 1800 volts, the divergence angle was 18.4 degrees, a 0.2 degree decrease from the original value.

Following the same logic, the process was repeated with a distance correction. Because the Faraday probe did not sweep in an arc, but instead in a straight line, the farther the probe moved from the centerline, the greater the overall distance from the thruster. To adjust the current density values, the all current densities were multiplied by the ratio of the total distance between the probe and ion engine to the minimum distance at zero degrees squared. With the new trendline equations, MATLAB was used to integrate. The final divergence for the 1600 volt case is 11.5 degrees. The 1700 volt case had a divergence of 10.4 degrees. For 1800 volts, the divergence increased to a final value of 19.3 degrees. Therefore, since the 1800 volt case is the most trusted, the most accurate divergence angle of the 1 cm ion engine, with the data collected in this testing, is 19.3 degrees.

V. Conclusions and Recommendations

5.1 Conclusions of Research

Due to numerous testing complications and the necessary work-arounds to actually obtain data for the ion engine, the research objectives were not fully met. Ideally, this research was attempting to use a thrust stand to accurately measure the thrust the ion engine was capable of producing, and find the specific impulse from there. Additionally, this research planned to gather divergence angle information from the thruster using an automated translational and rotational stage. In the SPASS Laboratory at AFIT, the vacuum chamber was more than large enough to house a torsional thrust stand, capable of precise and accurate measurements of micro-Netwon levels of thrust. Additionally, it houses a Plasma Controls 3-axis stage designed to traverse the chamber in an arc around the thruster face, a setup perfect for a Faraday probe to measure current density. However, the thruster never successfully operated at AFIT.

All of the testing of the thruster occurred at Busek, Co. Inc. The company was able to dedicate one of its vacuum chambers and two employees to assist in the setup and testing of the ion engine. The vacuum chamber did not have an automated stage already installed, and did not have the feedthroughs necessary to install a rotational stage. Additionally, the chamber was too small to fit the torsional thrust stand to measure thrust.

To find the thrust of the ion engine, a known relationship between beam current, screen voltage, and the propellant type was used in lieu of a thrust stand. Thrust data obtained in this manner for ion engines is accurate to within 5% of actual thrust stand values [6], and it was the best option available without having a thrust stand. The specific

impulse calculation is based on the thrust, so assuming all other values are accurate, it is also accurate to within 5% of the correct value. Taking into account the 10% error of mass flow rate, the specific impulse has an error of 17% off the correct value. Divergence information was gathered by manually moving the Faraday probe between tests, which is in no way as precise or reliable as data acquired by a translational stage. Compared to a translational stage, far fewer data points were obtained, and they had less accuracy due to the inability to rotate. The accuracy was addressed using a cosine correction.

5.2 Significance of Research

Though this research did not complete all of the original objectives, it was able to gather useful information with regards to the 1 cm ion engine. One must keep in mind the mission type of thrusters of this stature: precise actuation with very small thrust inputs, while retaining high enough specific impulse for feasibility to have a long mission life. It is important to notice the potential for throttleability in this thruster, due to its very linear responses in the operational regime. The thrust was reduced down to as low as 48 micro-Newtons by a mere power adjustment, and was increased to 118 micro-Newtons, with the potential to get higher. With a linear relationship, it is simple to find the power corresponding to a desired thrust for a given mass flow and achieve the necessary force on the spacecraft. The specific impulse remained greater than 1000 seconds for all points tested, and ranged up to 2475 seconds, with potentially higher values at greater input powers. Trendlines for both the thrust and specific impulse data had an R^2 value of 99.6%, indicating a high ability for accurate results from specified inputs. This impressively high statistic was obtained from relatively few data points, meaning more

data would only solidify the conclusion of the thruster's precision and throttleablility, indicating its potential in future Air Force missions.

5.3 Recommendations for Future Research

Though this research found important information about the Busek 1 cm micro RF ion engine, more testing would provide greater confidence in the conclusions reached in this paper. Numerous issues arose in the course of this research, many of which can be corrected with future experimentation. One of the biggest issues in need of change with future research is the neutralizer cathode.

The 1/16" electride cathode Busek provided with the ion engine was very convenient due to its immediate start, and worked throughout the majority of the testing efforts, even when the thruster did not. However, the lifetime on the neutralizer is far too short for any significant testing. This is because the calcium aluminate insert wears away with cathode usage. As the insert gets smaller, more power is required to emit the same number of electrons. Because the cathode is current limited, the current remains constant as the cathode fires. The only way to achieve higher power is to increase the voltage. As the voltage increases, so too does the temperature of the cathode. Near the end of its life, the cathode was red-hot, with voltages much higher than nominal. Unfortunately, without thermistors, the temperature of the cathode was not quantifiable, but it was too high for sustained operation. An image of this phenomenon is shown in Figure 40 and Figure 41, below.

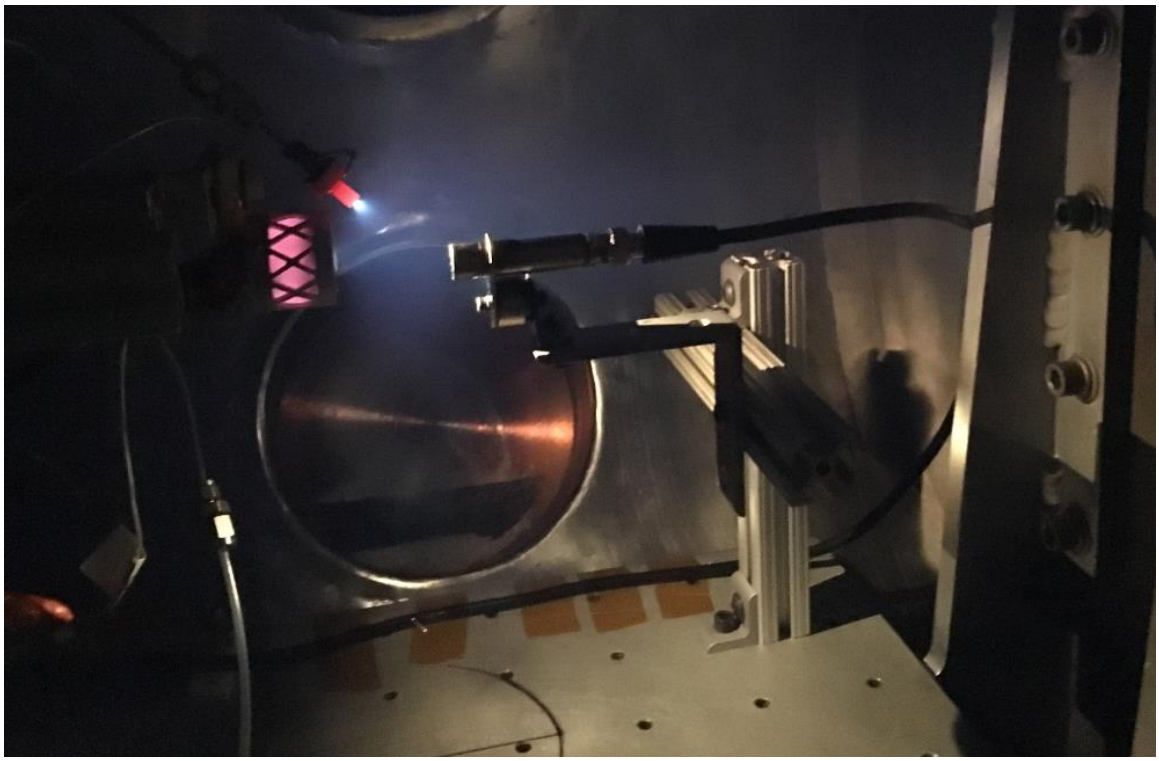

Figure 40. Ion Engine and neutralizer cathode firing at the end of life of the cathode. The cathode is red hot and producing significantly more light than normal, lighting the whole interior of the vacuum chamber.

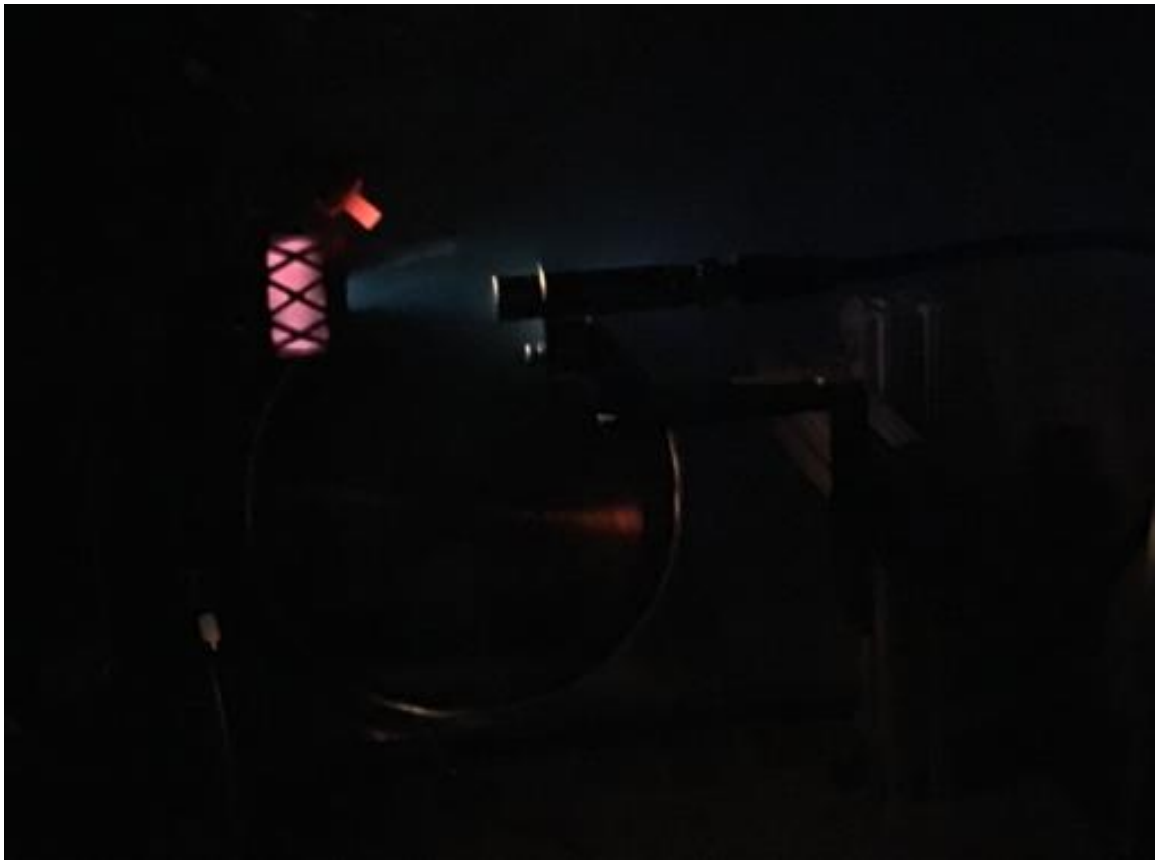

Figure 41. Ion engine firing with the neutralizer cathode off. In this image, one can see than the chamber is dark without the excessive light produced from the dying cathode. The cathode remains red-hot.

The tip of the cathode usually has a very tiny ball of visible light, but the failing cathode emitted a huge beam of light as shown in Figure 40, vastly different from normal operation. Even with the long exposure image, shown in Figure 33, the light produced by the cathode was much dimmer. Additionally, in the final tests, the cathode was sputtering, and it was possible to see sparks from impacts on the walls of the vacuum chamber. Unsteady performance from the neutralizer cathode definitely has the potential to impact results, so steady state capabilities are vital for future research.

When testing with a Faraday probe, the probe needs to be far enough away so when ions bombard it, they do not sputter the thruster or cathode. Alternatively, the probe

needs to be made of a material that is resistant to sputtering from ion impact. For a thruster of this size, the power of the beam dissipates too quickly to have the probe very far away. Therefore, the probe was placed close to the ion engine. The Faraday probe used in this research caused a lot of molecules to strike the thruster after impacting the probe. This is clearly visible in Figure 42. The face of the thruster was formerly the same color as the body. Additionally, discoloration is visible near the apertures on the thruster. As metal particles detach from the Faraday probe and sputter the ion engine, it is possible to negatively impact thruster performance, so changes to the probe setup are necessary in future research to avoid sputtering.

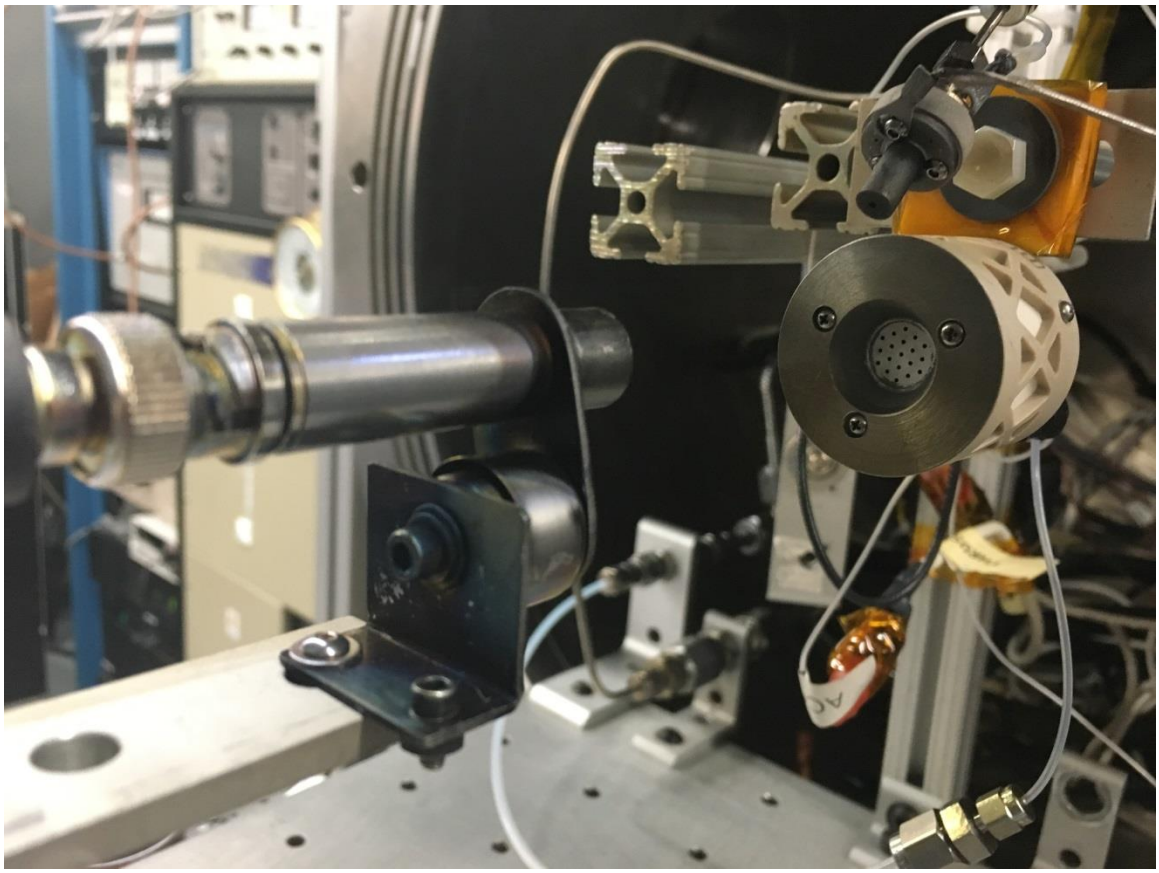

Figure 42. Ion engine after all testing was complete. The face of the thruster is visibly discolored due to particles from the Faraday probe striking it after being removed by high energy ions.

When performing the plasma generation process, future research should use the power detector, bi-directional coupler with two power sensors, and function generator linked with an amplifier method as opposed to an RF board. The former method was much more successful throughout the testing. Additionally, it grants more control when troubleshooting arises. The latter method was very difficult to fix, as all operations occurred behind the scenes, within what was, essentially, a black box. Vastly superior, the former method is easy to operate, despite the higher number of components required. One can see the readouts on all the devices to find and correct problems, so more devices

reign supreme for testing purposes. Operationally, the only choice is the RF board on the PPU, but multiple devices allows for easier testing.

Additionally, more data is required. With a more robust neutralizer cathode and an automated probe stage, all of the information obtained in this research is improvable. To fully quantify the divergence of the plume, much more than eight data points are required, and ideally, testing would occur on both sides of the plume to ensure symmetry and the capture of the centerline of the thruster. Additionally, a thrust stand is necessary to actually determine the exact thrust, rather than a close estimate. With that information, calculating a precise specific impulse is possible.

Finally, a more precise flow controller is necessary for 1 cm ion engines. The required 0.05 SCCM flow rate was not possible with enough accuracy with the Omega FMA-2601A. It was capable of providing the small amounts of xenon to fire the thruster, but with errors nearing 10%. Calculations relying on mass flow rates are not feasible for accurate numbers. Therefore, the specific impulse calculation could potentially change due to its dependence on mass flow rate. Also, the impact of mass flow rate on thrust and divergence is determinable with a precise flow controller, as the mass flow data obtained in this testing was inconclusive.

To fully assess the abilities of micro RF ion engines in the future, analysis on the best performing thruster is necessary. The BIT-1 thruster analyzed in this research was a prototype, as it was the first ion engine of that size. Busek, for example, has made improvements on their micro ion engines since the development of the BIT-1 after witnessing its performance, so superior models exist. In order to accurately and fairly test

these ion engines, the best versions, Busek thrusters or not, are necessary to determine their applicability in future Air Force missions.

5.4 Summary

The Busek 1 cm micro radio-frequency ion engine tested in this research demonstrated its accurate throttleablility through the variation of the total power input to the thruster. Its micro-Newton levels of thrust and potential to achieve several thousand seconds of specific impulse make it an intriguing option for long-duration, low thrust satellite maneuvers. To fully understand the capabilities of this ion engine, a new neutralizer cathode is required, along with additional testing across its full operational envelope. However, with the conclusions drawn from this research, it appears micro RF ion engines could have a future with precision CubeSat maneuverability.

Appendix

Table 2. Performance Characterization Data.

Test	RF Forward (W)	% Reflected	RF Load (W)	Screen Voltage (V)	Screen Current (mA)	Thrust (uN)	Mass Flow Rate (sccm)	Isp (s)
1	7.87	13.07%	6.841	1600	1.31	86.51	0.05	1809.42
2	7.95	11.45%	7.040	1600	1.19	78.58	0.04	2054.58
3	7.85	14.78%	6.690	1600	1.26	83.20	0.06	1450.29
4	7.89	13.37%	6.835	1600	1.21	79.90	0.05	1671.29
5	7.88	13.27%	6.834	1700	1.22	83.04	0.05	1736.97
6	7.88	13.25%	6.836	1800	1.23	86.15	0.05	1801.97
7	8.7	14.59%	7.431	1800	1.49	104.36	0.05	2182.88
8	9.42	15.78%	7.934	1800	1.69	118.37	0.05	2475.88
9	7.1	11.25%	6.301	1800	0.98	68.64	0.05	1435.72
10	6.36	9.10%	5.781	1800	0.69	48.33	0.05	1010.86
11	8.7	14.76%	7.416	1600	1.49	98.39	0.05	2058.04
12	8.7	14.59%	7.431	1700	1.51	102.78	0.05	2149.85
13	8.7	14.50%	7.439	1800	1.55	108.56	0.05	2270.78
14	8.7	14.57%	7.432	1600	1.48	97.73	0.05	2044.23
15	8.7	14.52%	7.437	1700	1.54	104.82	0.05	2192.56
16	8.7	14.50%	7.439	1800	1.54	107.86	0.05	2256.13
17	8.7	15.23%	7.375	1600	1.49	98.39	0.05	2058.04
18	8.7	14.99%	7.396	1700	1.51	102.78	0.05	2149.85
19	8.7	15.16%	7.381	1800	1.53	107.16	0.05	2241.48
20	8.7	14.50%	7.439	1600	1.53	101.03	0.05	2113.29
21	8.7	14.46%	7.442	1700	1.54	104.82	0.05	2192.56
22	8.7	14.40%	7.447	1800	1.58	110.67	0.05	2314.73
23	8.7	14.33%	7.453	1600	1.49	98.39	0.05	2058.04
24	8.7	14.26%	7.459	1700	1.48	100.74	0.05	2107.14
25	8.7	14.21%	7.464	1800	1.50	105.06	0.05	2197.53
26	8.7	14.68%	7.423	1600	1.48	97.73	0.05	2044.23
27	8.7	14.56%	7.433	1700	1.49	101.42	0.05	2121.38
28	8.7	14.50%	7.439	1800	1.52	106.46	0.05	2226.83
29	8.7	14.58%	7.432	1600	1.52	100.37	0.05	2099.47
30	8.7	14.50%	7.439	1700	1.53	104.14	0.05	2178.33
31	8.7	14.44%	7.444	1800	1.56	109.26	0.05	2285.43

Table 3. Performance Characterization Data Continued.

Test	Probe Voltage	Current Density (mA/cm^2)	Probe Perp (cm)	Probe Parallel (cm)	Total Distance (cm)	Angle (deg)	Total Power (W)	Corrected Current Density (mA)
1	4.5	1.0121	0	4.45	4.450	0.0	8.94	1.012
2	4.19	0.9423	0	4.45	4.450	0.0	8.94	0.942
3	4.63	1.0413	0	4.45	4.450	0.0	8.71	1.041
4	4.47	1.0053	0	4.45	4.450	0.0	8.77	1.005
5	4.3	0.9671	0	4.45	4.450	0.0	8.91	0.967
6	4.23	0.9513	0	4.45	4.450	0.0	9.05	0.951
7	5.37	1.2077	0	4.45	4.450	0.0	10.11	1.208
8	6.3	1.4169	0	4.45	4.450	0.0	10.98	1.417
9	3.43	0.7714	0	4.45	4.450	0.0	8.07	0.771
10	2.63	0.5915	0	4.45	4.450	0.0	7.02	0.591
11	3.27	0.7354	0.5	4.45	4.478	6.4	9.80	0.740
12	3.29	0.7399	0.5	4.45	4.478	6.4	10.00	0.745
13	3.3	0.7422	0.5	4.45	4.478	6.4	10.23	0.747
14	1.9	0.4273	1	4.45	4.561	12.7	9.80	0.438
15	2.01	0.4521	1	4.45	4.561	12.7	10.05	0.463
16	2.16	0.4858	1	4.45	4.561	12.7	10.21	0.498
17	0.77	0.1732	1.5	4.45	4.696	18.6	9.76	0.183
18	0.84	0.1889	1.5	4.45	4.696	18.6	9.96	0.199
19	0.9	0.2024	1.5	4.45	4.696	18.6	10.14	0.214
20	0.2	0.0450	2	4.45	4.879	24.2	9.89	0.049
21	0.2	0.0450	2	4.45	4.879	24.2	10.06	0.049
22	0.2	0.0450	2	4.45	4.879	24.2	10.29	0.049
23	4.82	1.0840	0.25	4.45	4.457	3.2	9.84	1.086
24	4.71	1.0593	0.25	4.45	4.457	3.2	9.98	1.061
25	4.24	0.9536	0.25	4.45	4.457	3.2	10.16	0.955
26	1.72	0.3868	0.75	4.45	4.513	9.6	9.79	0.392
27	1.85	0.4161	0.75	4.45	4.513	9.6	9.97	0.422
28	1.96	0.4408	0.75	4.45	4.513	9.6	10.17	0.447
29	0.51	0.1147	1.25	4.45	4.622	15.7	9.86	0.119
30	0.55	0.1237	1.25	4.45	4.622	15.7	10.04	0.128
31	0.59	0.1327	1.25	4.45	4.622	15.7	10.25	0.138

Bibliography

[1] "Glenn Contributions to Deep Space 1," NASA Glenn Research Center, 21 May 2008. [Online]. Available: http://www.nasa.gov/centers/glenn/about/history/ds1.html. [Accessed 20 August 2015].

[2] "Space Electric Rocket Test 1 (SERT 1)," NASA Glenn Research Center, 20 March 2007. [Online]. Available: http://www.grc.nasa.gov/WWW/ion/past/60s/sert1.htm. [Accessed 20 August 2015].

[3] D. M. Goebel, Fundamentals of Electric Propulsion: Ion and Hall Thrusters, 2008.

[4] J. R. Beattie, "XIPS Keeps Satellites on Track," *The Industrial Physicist,* 1998.

[5] J. R. Brophy, "NASA's Deep Space 1 Ion Engine," *Review Scientific Instruments,* vol. 73, pp. 1071-1078, 2002.

[6] M. Tsay, "Micro Radio-Frequency Ion Propulsion System," in *48th AIAA/ASME/SAE/ASEE Joint Propulsion Conference & Exhibit*, Atlanta, 2012.

[7] R. Jah and E. Choueiri, "Electric Propulsion," *Encyclopedia of Physical Science and Technology,* 2002.

[8] K. Groh and H. Loebt, "State-of-the-Art of Radio-Frequency Ion Thrusters," *J. Propulsion,* 1991.

[9] R. e. a. Walther, "Scaling Laws of Radio-Frequency Ion Thrusters," *AIAA,* 1975.

[10] M. Tsay, "Two-Dimensional Numerical Modeling of Radio-Frequency Ion Engine Discharge," Massachusetts Institute of Technology, 2010.

[11] D. Warner, "Advanced Cathodes for Next Generation Electric Propulsion Technology," Air Force Institute of Technology, Wright-Patterson Air Force Base, 2008.

[12] B. Rubin and J. Williams, "Hollow Cathode Conditioning and Discharge Initiation," *Journal of Applied Physics,* 2008.

[13] L. Rand and J. Williams, "Instant Start Electride Hollow Cathode," *Inernational Electric Propulsion Conference,* 2013.

[14] M. Patterson, "Scaling of Ion Thrusters to Low Power," *International Electric Propulsion Conference,* 1998.

[15] M. Tsay, *Personal Communications,* 2015.

[16] *Faraday Probe Operating Manual,* Colorado State: CSU Electric Propulsion and Plasma Engineering Laboratory.

[17] *Torsional Balance System Operation Manual,* Busek Co. Inc., 2007.

[18] *User Manual for Busek 1cm RF Ion Thruster BIT-1 System,* Busek Co. Inc., 2015.

REPORT DOCUMENTATION PAGE

Form Approved
OMB No. 074-0188

1. REPORT DATE *(DD-MM-YYYY)*	**2. REPORT TYPE**	**3. DATES COVERED** *(From – To)*
24-03-2016	Master's Thesis	March 2015 – March 2016

TITLE AND SUBTITLE

Empirical Determination of Performance Characteristics for Busek 1cm Micro Radio-Frequency Ion Propulsion System

5a. CONTRACT NUMBER

5b. GRANT NUMBER

5c. PROGRAM ELEMENT NUMBER

6. AUTHOR(S)

Muilenburg, Connor L., Second Lieutenant, USAF

5d. PROJECT NUMBER

5e. TASK NUMBER

5f. WORK UNIT NUMBER

7. PERFORMING ORGANIZATION NAMES(S) AND ADDRESS(S)
Air Force Institute of Technology
Graduate School of Engineering and Management (AFIT/ENY)
2950 Hobson Way, Building 640
WPAFB OH 45433-8865

8. PERFORMING ORGANIZATION REPORT NUMBER

AFIT-ENY-16-M-231

9. SPONSORING/MONITORING AGENCY NAME(S) AND ADDRESS(ES)
Air Force Research Labs Space Vehicles Directorate

10. SPONSOR/MONITOR'S ACRONYM(S)

AFRL/RQ

11. SPONSOR/MONITOR'S REPORT NUMBER(S)

12. DISTRIBUTION/AVAILABILITY STATEMENT
DISTRUBTION STATEMENT A. APPROVED FOR PUBLIC RELEASE; DISTRIBUTION UNLIMITED.

13. SUPPLEMENTARY NOTES
This material is declared a work of the U.S. Government and is not subject to copyright protection in the United States.

14. ABSTRACT
Performance characterization for the Busek 1 cm micro radio-frequency ion engine was experimentally accomplished across its full regime of operating conditions. The thrust was determined at the nominal operating condition using a known relationship for ion engines between beam current, screen voltage, and the mass of the propellant used. Specific impulse was found at the nominal operating condition by its relation to the thrust and mass flow rate. The divergence angle of the plume of the ion engine was calculated using readings from a Faraday probe. The probe collected current density data at various angles in front of the ion engine, and with integration, the divergence angle was found. The thrust and specific impulse of the ion engine varied linearly with the total power input, or the radio-frequency power plus the beam current times the screen voltage. This trait is very important for throttleability purposes, a useful capability for a thruster. The divergence angle of the 1 cm ion engine was calculated to be 18.1 degrees, a parameter that is ideally minimized to reduce cosine losses. Preliminary testing of this micro ion engine indicates that thrusters of this size may have potential in future CubeSat missions.

15. SUBJECT TERMS
Micro Ion Engine, Radio-Frequency, Electric Propulsion, Neutralizer Cathode, Faraday Probe

16. SECURITY CLASSIFICATION OF:			**17. LIMITATION OF ABSTRACT**	**18. NUMBER OF PAGES**	**19a. NAME OF RESPONSIBLE PERSON**
a. REPORT	**b. ABSTRACT**	**c. THIS PAGE**			Dr. Carl Hartsfield, AFIT/ENY
U	**U**	**U**	**UU**	115	**19b. TELEPHONE NUMBER** *(Include area code)* (937) 255-3636, ext 4667 (carl.hartsfield@afit.edu)

Standard Form 298 (Rev. 8-98)
Prescribed by ANSI Std. Z39-18